POLITECNICO DI TORINO

MSc in Automotive Engineering
A.A. 2024/2025

EXPERIMENTAL AND NUMERICAL ANALYSIS OF THE MODAL BEHAVIOUR OF A KART VEHICLE

Supervisors
Prof. Alessandro Vigliani
Dott. Ing. Angelo Domenico Vella

Candidate
Fedele Semerano

March 2025

Abstract

This thesis presents the model validation of a go-kart chassis frame, made through numerical and experimental modal analysis of a complete kart vehicle. Conducted in collaboration with Autoeuropeo Motorsport karting team, the Tony kart Racer 401 RR direct drive model year 2024 is taken under investigation with the aim of figure out the vibrational modes with the corresponding frequencies of the chassis and relative fundamental components. Moreover, a model updating is performed by hand with the purpose of reducing the percentage of error between experimental modal analysis (EMA) carried out by means of LMS-SCDAS software and finite element analysis (FEA) made with LUPOS (by MATLAB software), to spot the right material properties of the analysed components as well.

The study has started with the reverse engineering process of the main components, where a CAD model has been developed. Then, follows a numerical model generation of all the parts, for assessing the numerical vibrational modes obtained with the hypothesized material properties. With the Experimental modal analysis, it is possible to appraise the real vibrational behaviour of the numerical checked go-kart pieces and to make a successive model updating of the analysed components. By integrating in a single model all the previous numerical ones updated, the final go-kart vehicle assembly has been numerically simulated and experimentally tested.

All the efforts done in this paper, lead to pave the way for a following work oriented to the evaluation of the dynamic behaviour, integrating the results obtained into a multi-body system. Indeed, the multi-body numerical analysis of a go-kart is focused on the evaluation of the vehicle dynamics performance sensibility with respect to the stiffness of its main structural components. For this reason, the structural behaviour of these elements has been in deep analysed in this work.

Index

List of Figures

List of Tables

Chapter 1

1 Introduction

1.1 Karting: history, evolution and current status

“Kart racing” or simply “karting” is a motorsport discipline introduced around 1950s which started out as a fun-filled pastime, invented by Art Ingles in southern California. Over years, this racing activity quickly evolved into a phenomenon around the world, up to being the stepping stone to the higher ranks of motorsport.

According to CIK-FIA (International Karting Commission - Federation International Automobile), go-kart is a land vehicle with four non-aligned wheels in contact with the ground, two which control the steering while the other transmits the power. The first generation of these go-kart vehicles were made by a very simple body frame of steel pipes welded together on which is mounted the engine, the seat to host the driver, the steering system and, generally, only a rear braking system.

FIGURE 1.1: 1960S GO-KART.

As the years goes by, even if the fundamental structure has remained more or less the same, the design and technology of these vehicles saw significant advancements in the 1980s and 1990s up to witness a surge in go-karting's engineering development in the last 20 years, with improvements in safety features, engine performance and vehicle dynamics.

FIGURE 1.2: 2020S GO-KART.

It is even worth noting that, the technology in the karting field has grown so much so that the more competitive vehicles are equipped with data analysis and telemetry systems. Fixing some sensors for recording GPS longitudinal and lateral acceleration, engine RPM, speed, exhaust gas temperature and so on, it is possible to record what it is happening during a run section on the truck in order to analyse the kart behaviour and to spot the mistakes made by the driver.

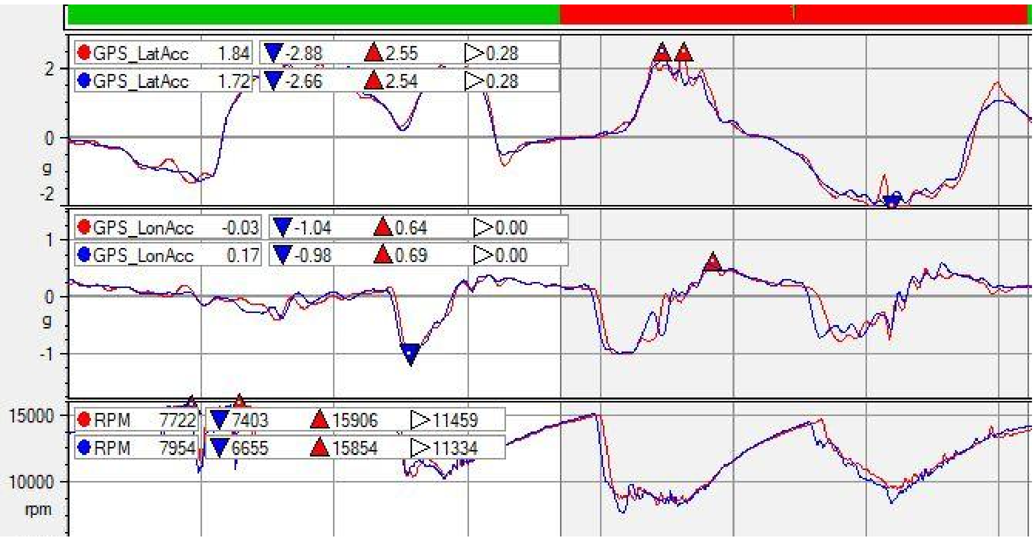

FIGURE 1.3: COMPARISON BETWEEN TWO LAP SECTORS OBSERVING GPS LATERAL ACCELERATION, GPS LONGITUDINAL ACCELERATION AND ENGINE RPM.

The main distinguishing features of these machines whether compared with a Formula open-wheeled racing car, are the absence of the suspensions system and differential. For these reasons, the cornering behaviour and the entire performance of the vehicle are strongly influenced by the structural characteristics of the frame, which it must be:

- Flexible, to make up and adjust itself for suspension function.
- Stiff and durable, to absorb the impact of manoeuvres and to withstand stresses and weight of driver, engine and accessories.

Moreover, the unavailability of the differential on the traction axle makes any cornering manoeuvre problematic. Indeed, while cornering, the inner rear wheel has a smaller forward velocity but the same spin velocity than the outer one, which leads to a yaw torque opposite to the yaw rate. Since the longitudinal force is approximately proportional both to the longitudinal slip and to the tyre load, to reduce such an undesired effect, the vertical load of the inner wheel should be as low as possible and ideally null. This condition may be obtained by designing a proper combination of chassis stiffness and steering system geometry (more information about this crucial aspect will be given in the section **3.1.3**.) but also choosing the right axle, seat and front anti-roll bar.

FIGURE 1.4: REAR-LEFT WHEEL RAISED-UP WHILE BENDING A LEFT CORNER.

In this way, the structural analysis of the tubular frame recovers a fundamental role inside the process of design and valuation of go-kart vehicles.

1.2 Model updating state-of-the-art and MacDisW.m

In this study, for making possible the validation of the numerical go-kart model, the model updating technique is adopted. Model updating is concerned about the correction of finite element models by processing the record of dynamic response from test structures in order to have an accurate model for any simulated analysis. Finite element model updating had emerged years ago as an important subject in structural dynamics. It has been used frequently and has been successfully applied to many fields especially in detecting the dynamic stiffness of a structure. This technique is used for reducing the percentage of error between the modal properties (natural frequency, mode shapes and damping ratio) experimentally obtained by means of modal analysis (EMA) and the modal properties numerically obtained through the finite element analysis (FEA) of each component of the go-kart vehicle. By adjusting the selective parameters, incongruities between those two analyses are generally reduced.

Considering that the geometry of the component taken under investigation cannot be changed for performing the model updating, for making consistence the numerical results, the only two parameters which can be potentially modified are:

- Young's modulus (**E**). The university of Birmingham outlines it as: "…a property of the material that tells us how easily it can stretch and deform. It is defined as the ratio of tensile stress (σ) to tensile strain (ε)", where stress is the amount of force applied per unit area (σ = F/A), strain, is extension per unit length (ε = dl/l). Starting from a certain value, its modification results in more stiff structure (if higher value with respect to the standard one) or less stiff structure (if lower value is chosen). Its variation has allowed to spot the right material Young's modulus value at the end of the optimization process.
- Material density (**ρ**). But, this parameter, must be changed if only if the numerical weight of the component given as output from LUPOS is different whether compared with the real one and once the operator is sure that the numerical component is well modelled in the FEM environment.

For this reason, the Young's modulus can be considered as the only variable to be adjusted. So, it is decided to do not commit this task to an optimization algorithm, performing it through trials and errors by hand.

LUPOS software gives the possibility to have an understanding of which is the correspondence between the numerical and experimental modal parameters after the model updating process: the function MacDistW.m. It evaluates the MAC index of correlation between two sets of eigenvectors with proportional distance of related natural frequencies, providing as output MAC_data, so the values of the MAC matrix. The Modal Assurance Criterion (MAC) is an essential tool in modal analysis. Its use to perform the pairing between two sets of modal vectors is now widespread. The great success of the MAC has fostered the emergence of numerous derivative criteria designed to deal with more specific situations.

The significant reduction in percentage of error before and after model updating procedure was carried out, clearly shows that model updating technique is a reliable method in reducing the discrepancies between EMA and FEA. Therefore, in cases of high discrepancies between analytical and actual test data, model updating can be considered as an option in order to obtain better correlation between those two sets of data.

1.3 Thesis outlook

In this thesis project, the firsts main engineering steps made in the go-kart factory for optimizing and improving the chassis and main components behaviour of a winning kart model are investigated. Indeed, starting from the reverse engineering phase explained in deep into chapter **3**, all the geometries can be available for the following evolution steps. Then, leveraging the model validation phase made through numerical and experimental modal analysis (chapter **4**, **5** and **6**), the modal parameters of the components are obtained for generating the complete go-kart vehicle final assembly (chapter **7**) manufactured with all the spotted right material properties. A very interesting comparison is shown at the end, where it is revealed how the stiffness of the chassis changes when all the vehicle components are introduced into the final model. Finally, the main outcomes of the study are summarised in the conclusion.

Chapter 2

2 Main components: overview and engineering function

In this chapter, is presented an overview and an explanation about the engineering function of the four main structural components of a go-kart vehicle which affect the most the dynamic behaviour:

1. Chassis;
2. Front Anti-roll bar;
3. Seat;
4. Rear axle.

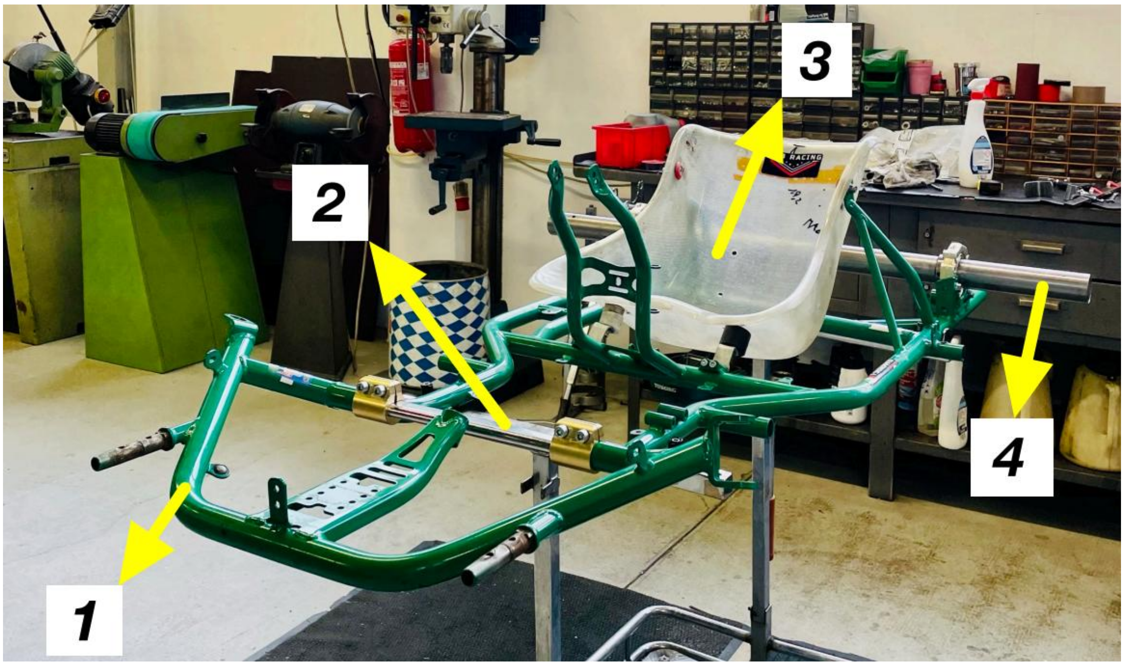

FIGURE 2.1: FOUR MAIN STRUCTURAL PARTS OF A GO-KART. CHASSIS (1), FRONT ARB (2), SEAT (3) AND REAR AXLE (4).

For understanding how and in which way all these 4 components contribute to the performance of the entire vehicle, a brief background about the longitudinal and lateral dynamics is going to be reported:

- STATIC LOAD DISTRIBUTION and LONGITUDINAL LOAD TRANSFER.
  Considering a very simple vehicle, the normal static force F_z applied to front and rear wheel is equal to:

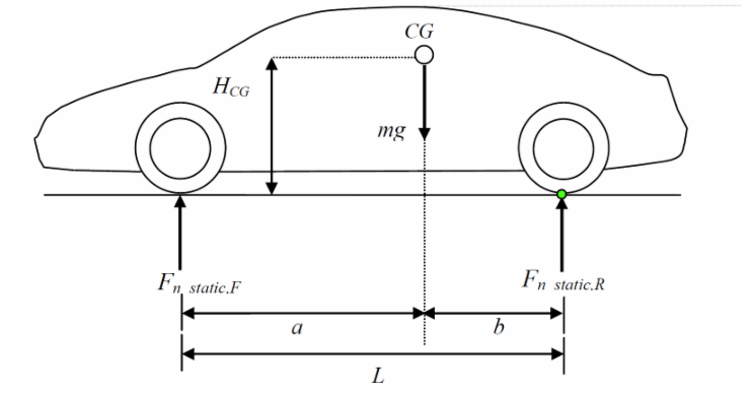

FIGURE 2.2: STATIC LOAD DISTRIBUTION ON VEHICLE.

$$\boldsymbol{F_{n\,static\,Front}} = \boldsymbol{mg\frac{b}{L}}, \text{ FOR THE SINGLE WHEEL } \rightarrow \boldsymbol{F_{Z,FLR,st}} = \boldsymbol{\frac{1}{2}mg\frac{b}{L}} \qquad (2.\,1)$$

$$\boldsymbol{F_{n\,static\,Rear}} = \boldsymbol{mg\frac{a}{L}}, \text{ FOR THE SINGLE WHEEL } \rightarrow \boldsymbol{F_{Z,RLR,st}} = \boldsymbol{\frac{1}{2}mg\frac{a}{L}} \qquad (2.\,2)$$

The centre of gravity (CoG) in a go-kart vehicle is in correspondence of the seat (since it hosts the driver), in a position a bit translated towards the engine due to its weight (as shows images **2.3**).

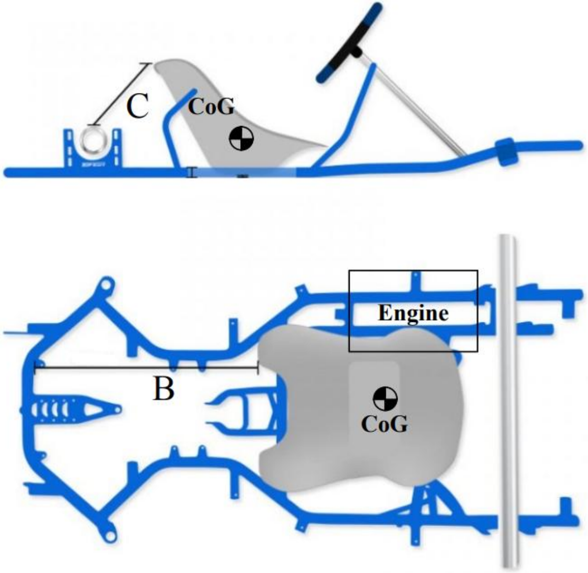

FIGURE 2.3: COG OF A GO-KART.

Modifying the distances B and C during the seat assembly phase, it is possible to change the CoG position as required. It has a direct effect of the static load distribution but even on the front and rear load transfer during the acceleration or braking phase because, changing C, the height of the centre of gravity is modified.

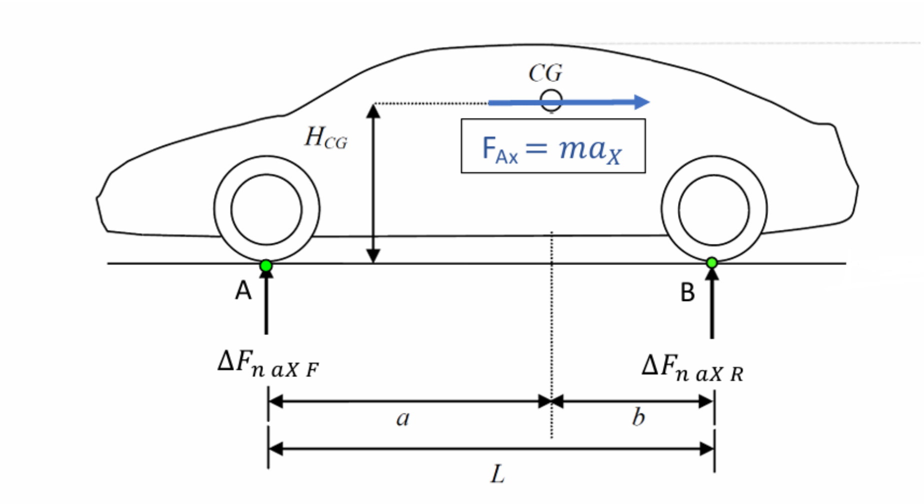

FIGURE 2.4: LONGITUDINAL LOAD TRANSFER ON A VEHICLE DURING THE ACCELERATION OR BRAKING PHASE.

$$\boldsymbol{\Delta F_{n\,aX\,F} = -F_{Ax}\frac{H_{CG}}{L} \rightarrow \Delta F_{n\,aX\,FL} = \Delta F_{n\,aX\,FR} = -\frac{1}{2}ma_x\frac{H_{CG}}{L}} \tag{2. 3}$$

$$\boldsymbol{\Delta F_{n\,aX\,R} = -F_{Ax}\frac{H_{CG}}{L} \rightarrow \Delta F_{n\,aX\,RL} = \Delta F_{n\,aX\,RR} = -\frac{1}{2}ma_x\frac{H_{CG}}{L}} \tag{2. 4}$$

Considering now the typical characteristic of the tyre describing the longitudinal behaviour, reported in figure **2.5**, it is possible to see that the longitudinal force F_x that the tire can develop, depends on the vertical load F_z, where $\sigma = tire\ slip$.

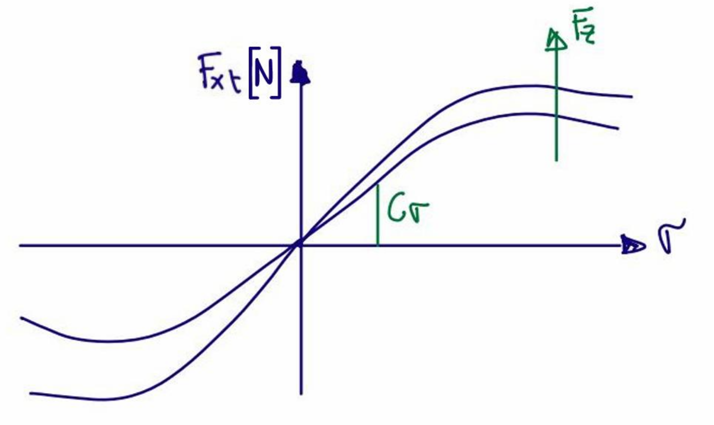

FIGURE 2.5: TYPICAL CHARACTERISTIC OF THE TIRE DESCRIBING THE LONGITUDINAL BEHAVIOUR.

But the increasing of vertical force has benefits only up to a certain limit, owing to the presence of the tire saturation over which the performance of the tire becomes unstable.

- LATERAL LOAD TRANSFER due to lateral acceleration with roll motion.
  When a vehicle starts to bend a curve, a centrifugal force $F_{y,RC}$ is applied in the roll centre in the opposite direction with respect to the centre of the curvature. This generates a lateral load transfer from the inner wheels to the outer ones, with a consequent variation of the normal force F_z applied to each wheel. A front-view of a general vehicle performing a left-curve, can allow to better explain the concept:

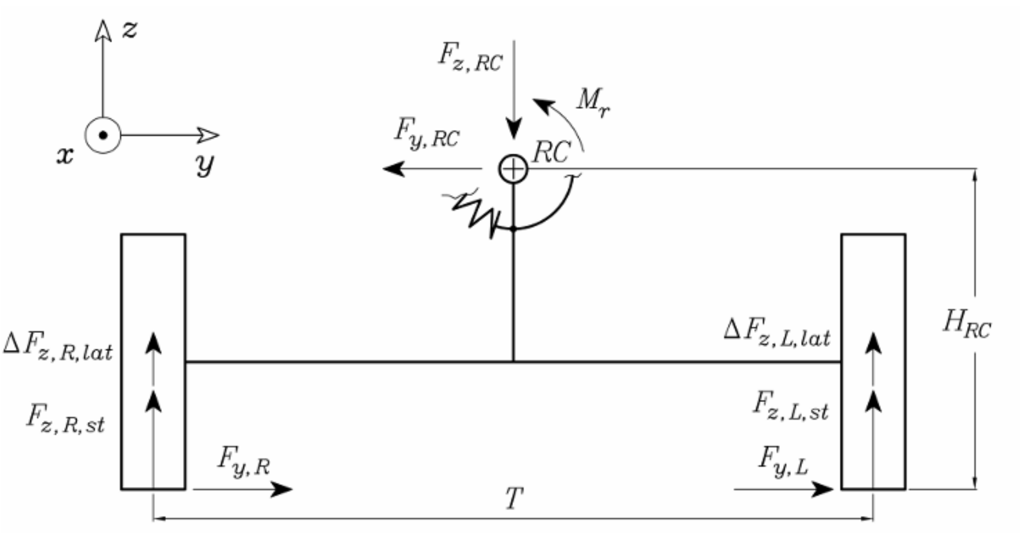

FIGURE 2.6: LATERAL LOAD TRANSFER ON A VEHICLE DURING LEFT-CORNERING OPERATION.

TOT. LOAD TRANFER: $\boldsymbol{\Delta F_{z,lat,F/R} = \frac{1}{T_{F/R}}[\,H_{RC}\left(F_{y,R,F/R} + F_{y,L,F/R}\,\right) + M_{r,F/R}\,]}$ (2. 5)

ROLL MOMENT: $\boldsymbol{M_{r,F/R} = K_{F/R}\varphi + C_{F/R}\dot{\varphi}}$ (2. 6)

- φ = roll angle.
- $K_{F/R} = K_{spring,F/R} + K_{ARB,F/R}$. Total roll stiffness of Front or Rear axle, which in a vehicle equipped with suspensions is equal to the sum of the stiffness of the suspension spring $K_{spring,F/R}$ plus the contribution given by the anti-roll bar $K_{ARB,F/R}$.
  For a go-kart vehicle, the stiffness of the spring is substituted by the stiffness of the chassis (which depends on the geometry of the frame and on the utilized material) that will be called $K_{chassis,F/R}$.
- $C_{F/R}$ = Total roll damping contribution of Front or Rear axle, equal to zero for go-kart case since no suspensions are present.

Writing the complete equations for Front and Rear axle adjusted for the go-kart vehicle, it is possible to write:

$$\text{Front axle: } \boldsymbol{\Delta F_{z,lat,F} = \frac{1}{T_F}[H_{RC,F}(F_{y,FL} + F_{y,FR}) + (K_{chassis,F} + K_{ARB,F})\varphi]} \qquad (2.\ 7)$$

$$\text{Rear axle: } \boldsymbol{\Delta F_{z,lat,R} = \frac{1}{T_R}[H_{RC,R}(F_{y,RL} + F_{y,RR}) + (K_{chassis,R} + K_{ARB,R})\varphi]} \qquad (2.\ 8)$$

From the last two written equations it is clearly shown that, increasing the stiffness of the chassis (by making some modifications that will be well explained in the section **2.1**) or increasing the stiffness of the anti-roll bar (more detailed information in the section **2.2** and **2.4**), more load transfer is experienced on that axle. This means more vertical load acting on the tire but, as explained before in the longitudinal dynamics studying, the benefits of having higher vertical load are verified up to a certain threshold.

A very simple example can make easier the understanding of the tire behaviour:

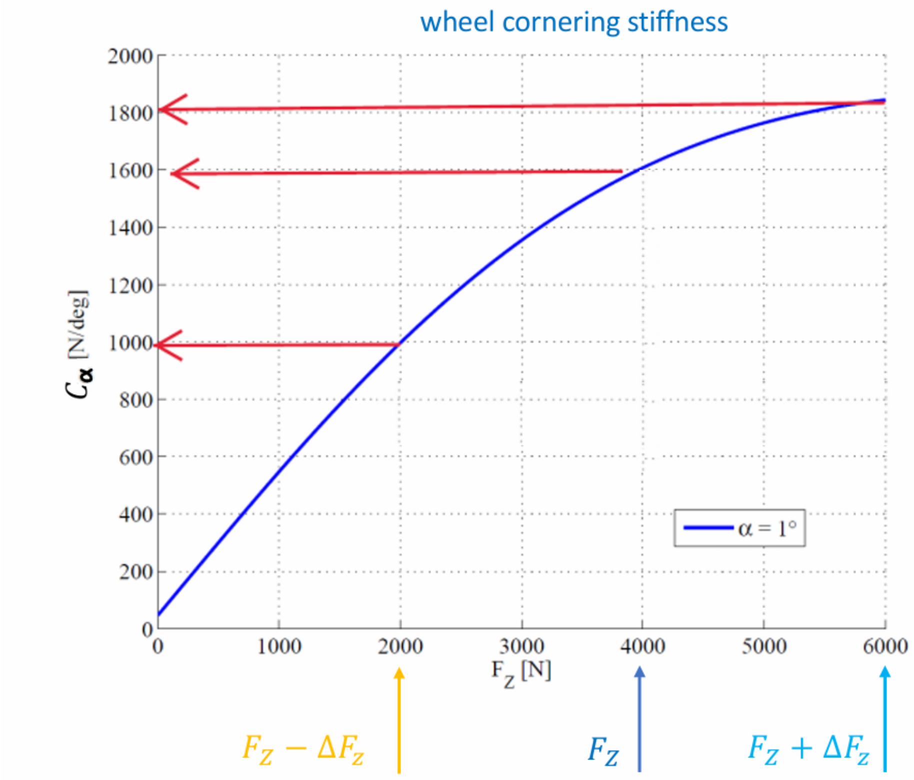

Figure 2.7: Wheel cornering stiffness and lateral load transfer.

- In NO load transfer conditions, the cornering stiffness of each wheel of the axle is equal to $C_\alpha = 1600 \frac{N}{deg}$, so the axle cornering stiffness has a value of $C_\alpha = (1600 + 1600)\frac{N}{deg} = 3200 \frac{N}{deg}$.
- In case of load transfer $\Delta F_z = 2000\,N$, it can be noted that the total cornering stiffness of the axle is equal to $C_\alpha = (1000 + 1800)\frac{N}{deg} = 2800\frac{N}{deg}$, so more than 10% less due to the non-linear behaviour of the cornering stiffness with respect to vertical load.

In the following sections, will be in deep explained how the engineering parameters reported until now can be modified, starting with operation that can be made during development chassis phase (geometry, materials etc...) up to changing that can be done on track by the employment of different types of front anti-roll bar, seats, or axles.

2.1 Chassis

Go-kart chassis is the vehicle's supporting structure made by hollow pipes welded together which acts as a load bearing framework that, structurally, supports the driver and the engine. It is the core of the go-kart, which bears all the stresses in both static and dynamic conditions. For allowing the correct functioning of the complete vehicle during the running section on truck, it embeds various components like braking system, steering mechanism, cooling system, wheels, a very simple transmission mechanism, body works and engine mounting.

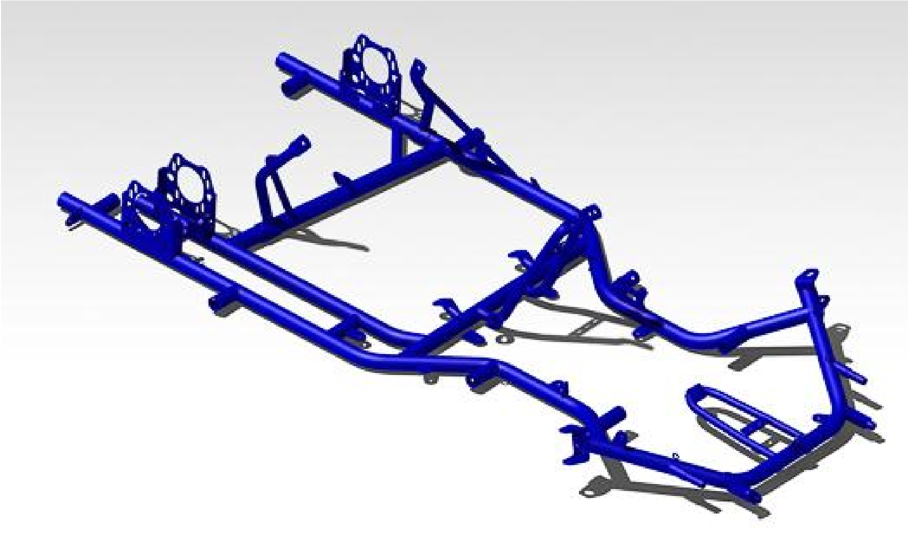

FIGURE 2.8: CHASSIS.

In the past, different types of pipes cross section were used but, nowadays, only the circular cross-section is adopted because of its high resistance of twisting effect and possesses torsional rigidity. It is important to be noted as well that, the round cross-sectional tube, presents greater energy absorption ability than the square cross section tube or any other. This is fundamental since the body frame needs to withstand all the static and dynamic stresses and loads which come from the road, the curb, the weight of the driver, the impact with other vehicles and so on and so forth.

The pipes diameter can vary from 28mm to 32m with a thickness of 2mm. It is not mandatory to select just one pipe diameter measure for producing the structure, in fact there are some chassis which have a combination of pipes with different diameter, in order of having the required stiffness $K_{chassis,F/R}$. Indeed, depending on the type of the truck that can be more or less demanding in terms of chassis flexibility due to grip conditions, tight or not corners, high or low speed corners and so on, a chassis with all pipe's diameter of 30mm, 32mm or a blend of the two measures, can makes the difference. If the tubing size is less, the kart will be more flexible, which means its ability to go over curbs is better and makes the chassis lightweight whereas, if the tubing size is more, the kart will become stiffer and would give better handling and grip on the track. Generally, 32mm chassis is best suited for low grip conditions while, 30mm for high grip situations. But, it is true if the employed material is the same for the three configurations defined before. Obviously, changing the material of the frame, using a less stiff one for example, can lead to use pipes diameter of 32 even in high grip conditions.

For all the reasons reported up to now, the material selection for the body frame is a very heavy task for kart manufacturers as it has many constraints of weight, structural resilience towards various types of forces, torsional rigidity (and so impact on $K_{chassis,F/R}$), factor of safety under application of various loads and market availability with pricing and cost constraints. The most used materials are:

- various grades of steel, where the amount of carbon in steel is important to determine the hardness, and providing desired strength, endurance, safety and reliability of the vehicle.
- aluminium alloys.

2.2 Front Anti-roll bar

The anti-roll bar, according to Milliken (1995), is responsible for vertically connecting the left and right wheels of the same axle, reducing body roll. During a turn, the anti-roll bar generates dynamic reactions, rotations, and deflections that are transmitted from one wheel to the other, creating a physical dependency that increases chassis stiffness. It is worth noting that this bar only affects lateral movements, where the wheels have opposite movements, and it is useless for longitudinal movements such as acceleration and braking, where the wheels either move up or down together relative to the chassis.

The stiffness and roll of the chassis can be adjusted by adding or removing the anti-roll bar. The attachment location, material, and geometry of the bar directly affect chassis stiffness.

FIGURE 2.9: OVAL FRONT BAR OF TONY KART CHASSIS.

Anti-roll systems serve two primary purposes: mitigating body roll and providing adjustable stiffness on one side compared to the other. While roll is not excessively detrimental in vehicles with low centres of gravity like karts, it can induce a force that affects the tire's contact angle with the ground, commonly referred to as “camber”, thereby reducing tire efficiency. Due to minimal roll, the ARB (Anti-Roll Bar) of a kart has limited influence on altering the tire's contact angle with the ground. However, it significantly affects lateral load transfer per axle, consequently impacting the vehicle's behaviour.

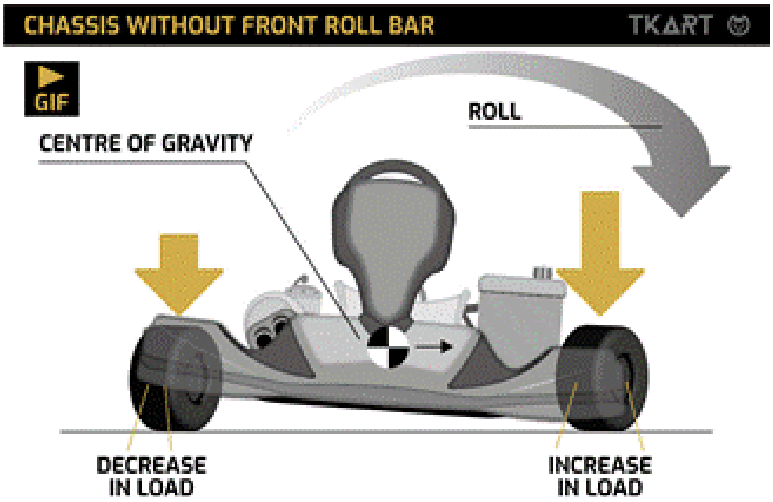

FIGURE 2.10: ROLL EFFECT.

Nowadays, many types of ARB are sold on the market, with particular and complicated shapes (round, oval, hollow or with solid cross section etc…) but even made by distinct types of materials (Structural steel, PVC, Carbon Fiber, Al 6061-T6), which have different values of stiffness $K_{ARB,F}$ in order to satisfy the requirements about the requested dynamics.

FIGURE 2.11: DIFFERENT TYPES OF FRONT ARB.

2.3 Seat

The seat is one of the main components of the complete vehicle since it holds the driver body in the kart. It is fastened in 4 points directly on the chassis and, since the driver weight is the most important factor which influences the centre of gravity position of the entire vehicle, the choice of all the measure to be utilized in the seat assembly phase, will have an impact on the karting dynamics behaviour (as explained in the introductive part of this chapter, where the 2 main measure to be chosen were defined with “B” and “C” in the figure **2.3**).

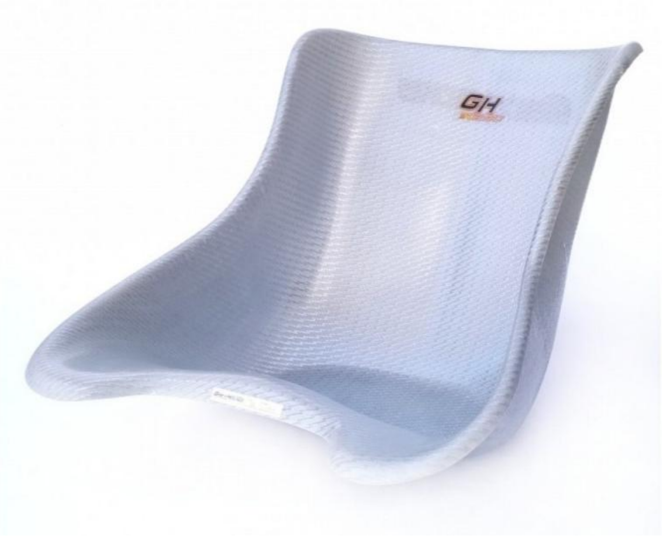

FIGURE 2.12: GREYHOUND SILVER RACING SEAT.

There is a general rule given by the kart manufacturers, which indicates the seat position with respect to driver height, distinguishing direct drive and gear box kart:

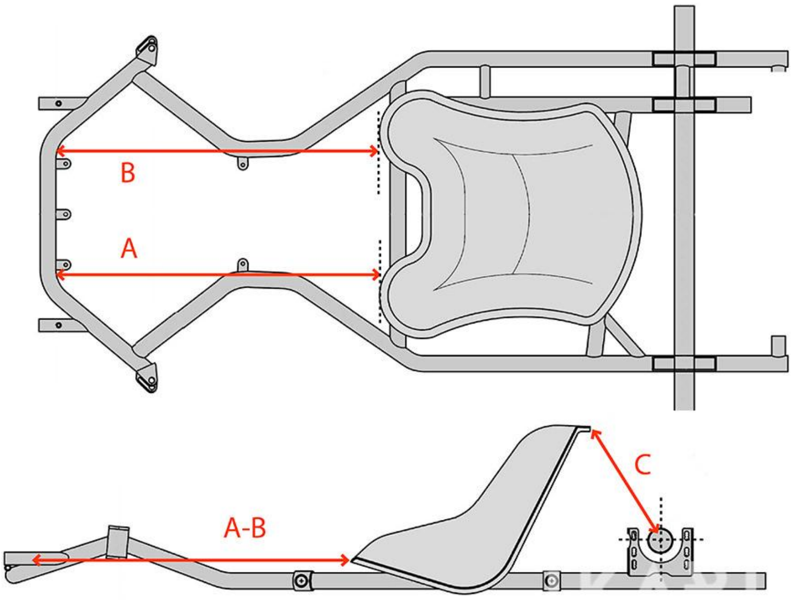

FIGURE 2. 13: SEAT POSITION MAIN MEASURES.

DIRECT DRIVE KART STD SEAT				
Driver height	150/160 cm	160/170 cm	170/180 cm	180/190 cm
A	640mm	650mm	660mm	665mm
B	645mm	655mm	665mm	670mm
C	200mm	195mm	190mm	185mm

TABLE 2.1: DIRECT DRIVE STANDARD SEAT MEASURE.

GEAR BOX KART STD SEAT				
Driver height	150/160 cm	160/170 cm	170/180 cm	180/190 cm
A		660mm	670mm	680mm
B		665mm	675mm	685mm
C		200mm	195mm	195mm

TABLE 2.2: GEAR BOX KART STANDARD SEAT MEASURE.

Comparing the values of the two tables for the same driver height, it is possible to see that the seat in the gear box kart must be assembled rearward with respect to a direct drive kart: it is due to the more power available in the gear shifting category, so positioning the CoG backward allows to have more traction. As a matter of fact, in karting, the seat's contribution is not in the way of comfort. Indeed, the general indications are usually "not followed" if other better solutions enable to be faster on track.

The most used material for seat production is the fiberglass but, depending on the resin and on the layers of glass fibre introduced, different seat stiffnesses can be obtained. Carbon fibre is employed as well. Furthermore, there are different shapes employed for having a different longitudinal and lateral load transfer with respect to the standard shape (image **2.12**):

FIGURE 2.14: GREYHOUND RACING SEAT DIFFERENT DESIGN.

For these reasons, the racing seat is another element to work with to obtain the best setup.

2.4 Rear axle

The rear axle is a very particular component of the go-kart assembly owing to its multiple functions.

FIGURE 2.15: REAR AXLE.

First of all, it allows to transmit the power from the engine to the wheel, thanks to a gear wheel which is assembled directly on the axle itself which is connected to the engine sprocket by means of a transmission chain mechanism (image **2.16**)

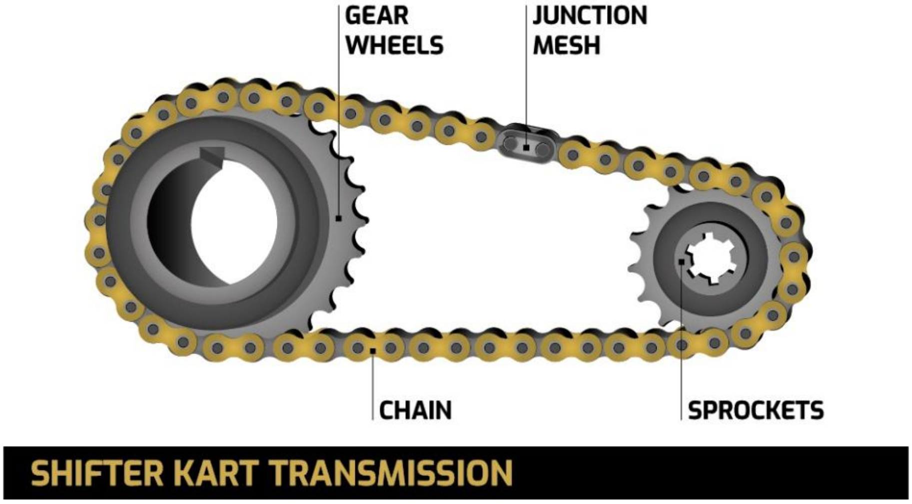

FIGURE 2.16: SHIFTER KART TRANSMISSION.

The axle is fixed on the go-kart body frame by means of forged axle's supports which hosts the axle's bearing (figure **2.17**) to permit the rotation.

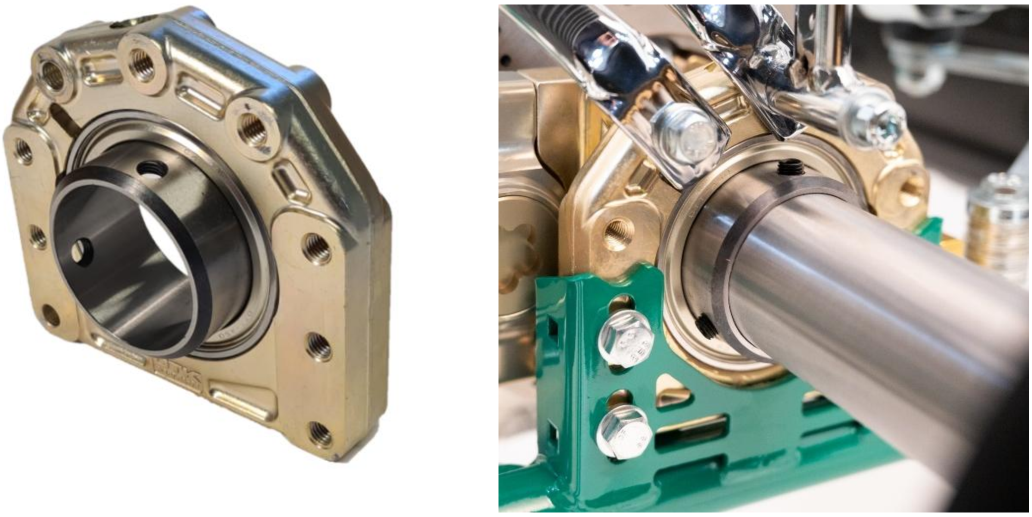

FIGURE 2.17: FOGED AXLE'S SUPPORT PLUS BEARING (LEFT) AND EXAMPLE OF MOUNTED SYSTEM ON THE CHASSIS (RIGHT).

It is very important to be noted that, in the new go-kart models is not used anymore the rear anti-roll bar since the axle reproduce this effect connecting rigidly the left and right side of the rear body frame. Owing to this, kart manufacturers have produced disparate types of axles with different hardness in order to vary the value $K_{ARB,R}$ previously defined for the evaluation of the total rear load transfer (equation **2.8**). The following image **2.18** displays the Hardness chart of the different types of axles produced by the OTK group with length of 50mm and 2mm of thickness: axle of type N is the standard one.

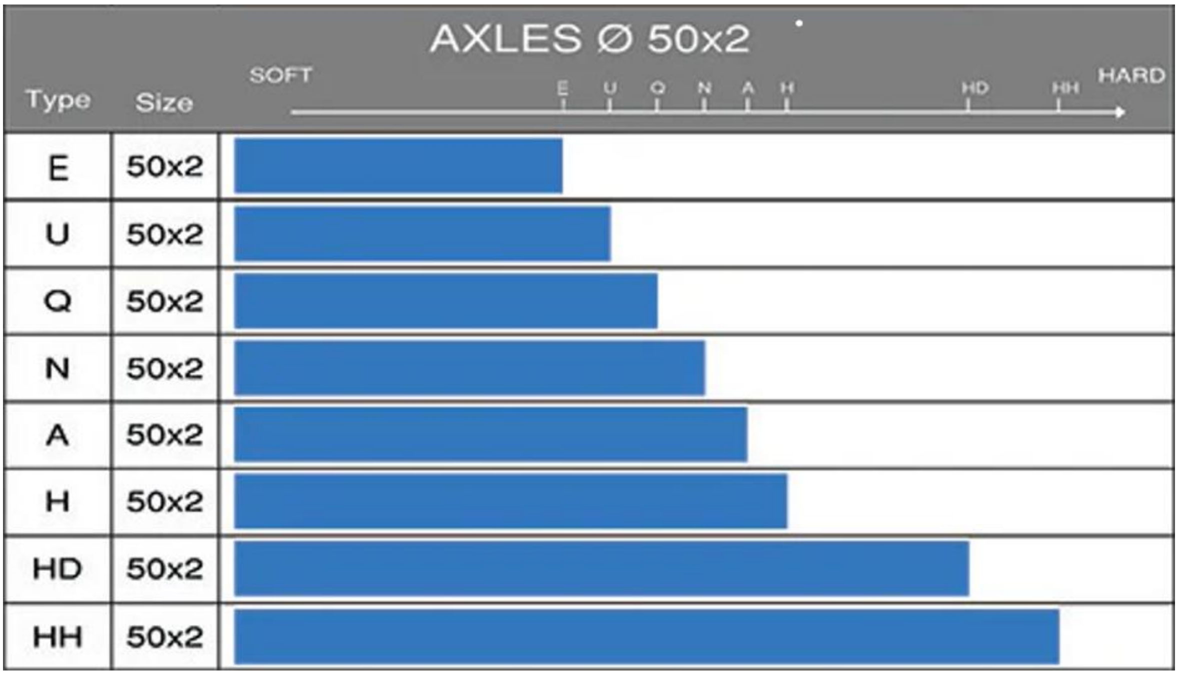

FIGURE 2.18: OTK AXLE HARDNESS CHART.

In addition, the stiffness of the axle has even an enhancing or not effect about the rising-up of the rear inner wheel while the vehicle is performing a curve. For this reason, since the changing of the axle is an action which does not requires too much time, different types of axles can be tried during a testing day for finding the right setup.

Chapter 3

3 Reverse engineering process

The operative working phase of this thesis starts with the geometrical reverse engineering process, which foresees the measurement and the acquisition of the fundamental geometries that characterize the go-kart vehicle main components. This process is essential to reconstruct a precise geometrical model of the foremost vehicle parts that can be easily adopted in the subsequent structural and dynamic virtual analyses.

The Autoeuropeo Motorsport go-kart team has given available to us the system chassis plus front anti-roll bar, seat and rear axle that is shown in figure **2.1.** After the detailed reverse engineering process made by hand-measurements using some reference systems during the acquisition phase for being as much meticulous as possible, the final 3D CAD Model assembly created using SolidWorks software, is revealed in figure **3.1.**

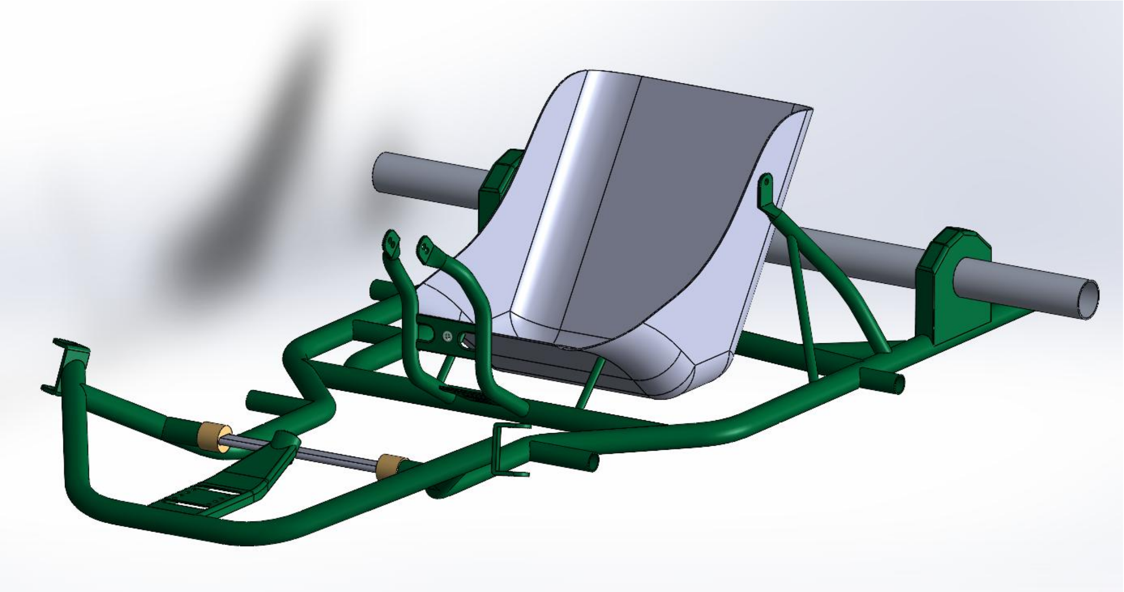

FIGURE 3.1: ASSEMBLY 3D CAD MODEL.

All the intermediate steps done before arriving to the final result shown in the previous picture **3.1**, will be deeply presented in the following sections.

3.1 Chassis: Tony kart Racer 401RR

The chassis that has been chosen for this development work is the Tony kart Racer 401 RR direct drive model year 2024, since it is one of the most winning chassis of the modern era. Indeed, the Exprit Noesis RR chassis which is part of the OTK group (that encompasses Tony kart, Exprit and other brands), has won the 2023 world championship and the 2024 European championship. The only difference between Tony kart Racer 401 RR and Exprit Noesis RR is about the colour and, clearly, the name. Materials, geometry and components are exactly the same.

FIGURE 3.2: EXPRIT NOESIS RR (ON THE LEFT SIDE) AND TONY KART RACER 40RR (ON THE RIGHT SIDE).

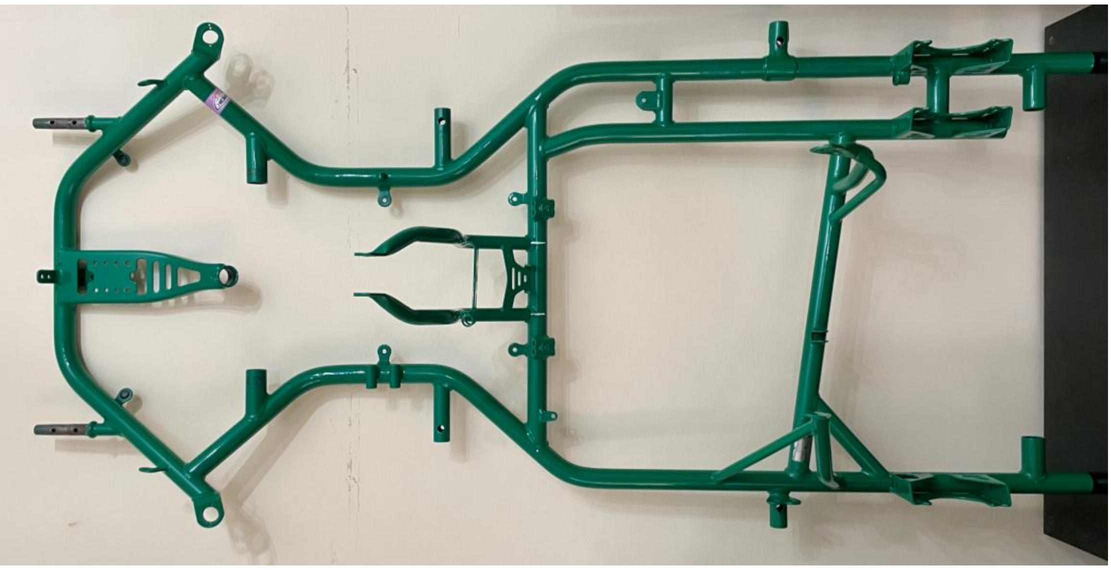

FIGURE 3.3: NAKED CHASSIS OF TONY KART RACER 401RR AT OUR DISPOSAL FOR THE ANALYSIS.

3.1.1 Fiche homologation and main geometries

When a new chassis is conceived, the factory needs to fill in the homologation form provided by the Commission Internationale de Karting (CIK) – FIA which reproduces descriptions, illustrations and dimensions of the chassis frame at the time of the CIK-FIA homologation. Into this paper, it is possible to find a photo of complete chassis identical to one of the models submitted for homologation without bumpers, brakes, bodywork, seat or tyres and, more interesting for us, a technical drawing (scale 1:10) used for the identification of the structure and the geometry of the frame.

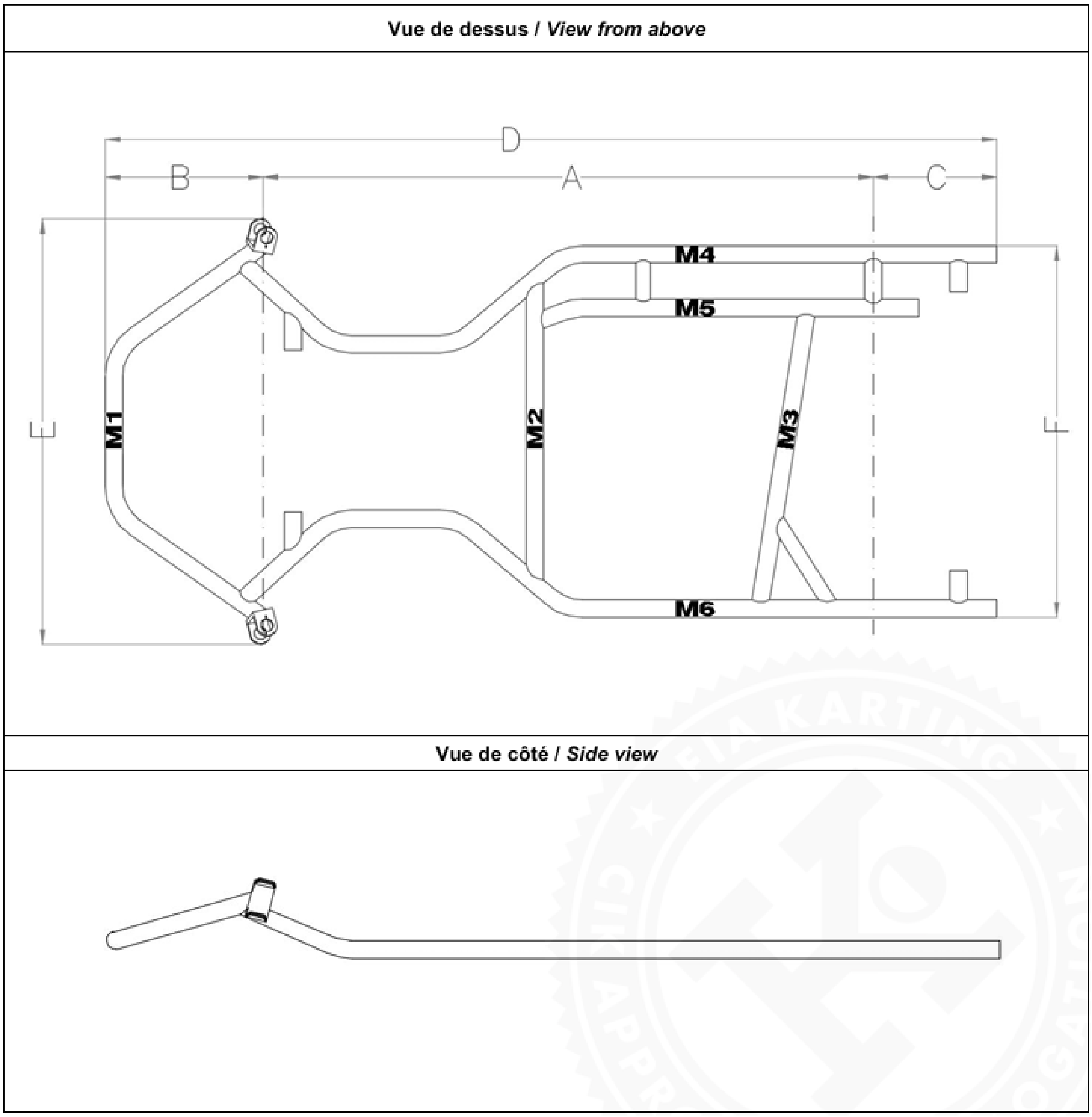

FIGURE 3.4: VIEW FROM ABOVE AND SIDE VIEW OF THE CHASSIS.

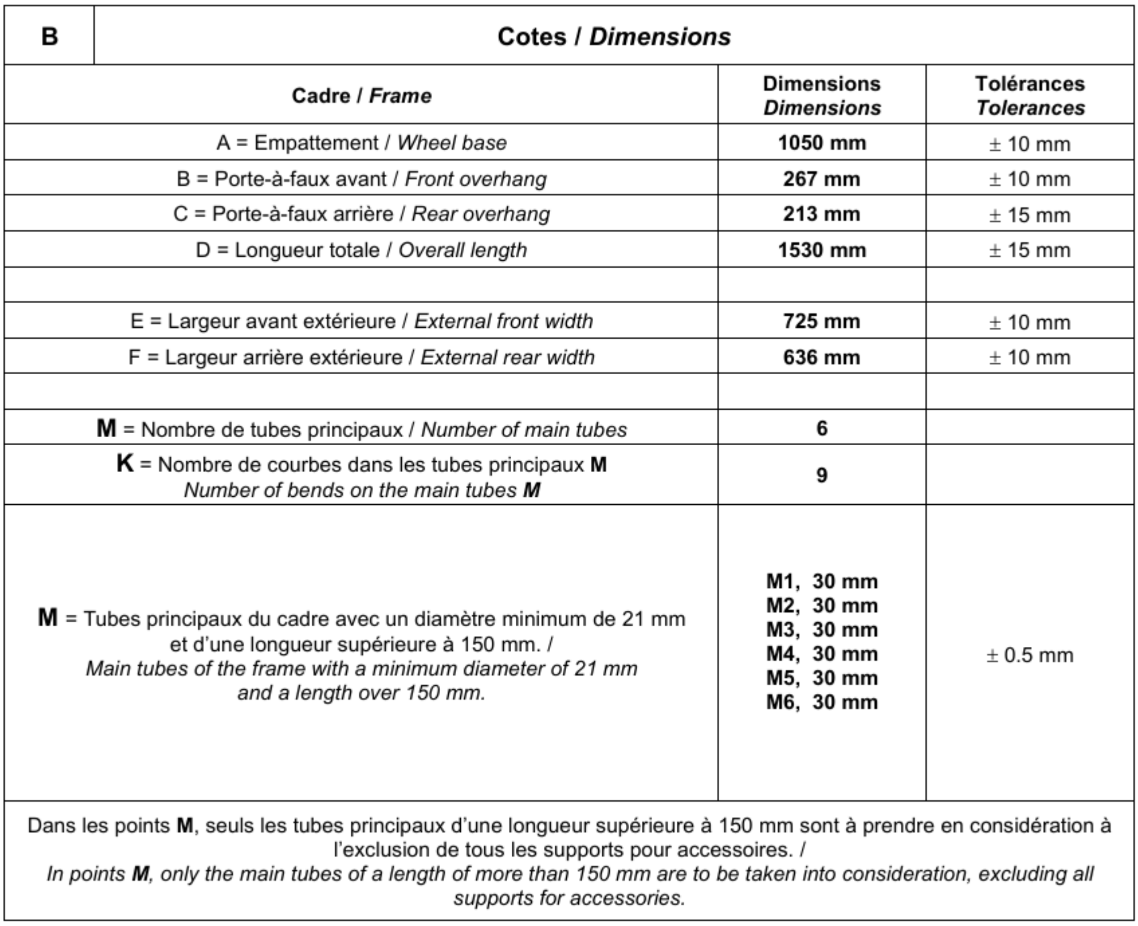

B	**Cotes / *Dimensions***	
Cadre / *Frame*	**Dimensions** ***Dimensions***	**Tolérances** ***Tolerances***
A = Empattement / *Wheel base*	**1050 mm**	± 10 mm
B = Porte-à-faux avant / *Front overhang*	**267 mm**	± 10 mm
C = Porte-à-faux arrière / *Rear overhang*	**213 mm**	± 15 mm
D = Longueur totale / *Overall length*	**1530 mm**	± 15 mm
E = Largeur avant extérieure / *External front width*	**725 mm**	± 10 mm
F = Largeur arrière extérieure / *External rear width*	**636 mm**	± 10 mm
M = Nombre de tubes principaux / *Number of main tubes*	**6**	
K = Nombre de courbes dans les tubes principaux **M** *Number of bends on the main tubes **M***	**9**	
M = Tubes principaux du cadre avec un diamètre minimum de 21 mm et d'une longueur supérieure à 150 mm. / *Main tubes of the frame with a minimum diameter of 21 mm and a length over 150 mm.*	**M1, 30 mm** **M2, 30 mm** **M3, 30 mm** **M4, 30 mm** **M5, 30 mm** **M6, 30 mm**	± 0.5 mm
Dans les points **M**, seuls les tubes principaux d'une longueur supérieure à 150 mm sont à prendre en considération à l'exclusion de tous les supports pour accessoires. / *In points **M**, only the main tubes of a length of more than 150 mm are to be taken into consideration, excluding all supports for accessories.*		

FIGURE 3.5: MAIN DIMENSIONS SPECIFIED BY THE MANUFACTURER.

So, taking the information from the technical drawing and all the measures given into the documentation, the reverse engineering process of the chassis has begun.

3.1.2 CAD model generation process

The 3D geometrical CAD model of the chassis has been created using SolidWorks 2023 software, starting from a new sketch. As already mentioned, this process has been made by hand due to the non-availability of system like CMM (Coordinate measuring machine). For this reason, to gather all the information needed to reconstruct the tubular frame geometry a lot of angle calculations and measurements has been carried out, since the frame is composed by tubular elements (formed by straight and curved elements) and some other components welded to them, whose function is that of supporting the rear axle, the seat, the front wheels, the steering system, etc. Thereby, after each angles/lengths evaluation process, line by line, the complete main structure of the frame took shape. Just for giving an idea about the level of complexity of the chassis sketch, the following image **3.6** reports all the mandatory quotes introduced during the reverse engineering phase for reproducing in the correct way the body frame.

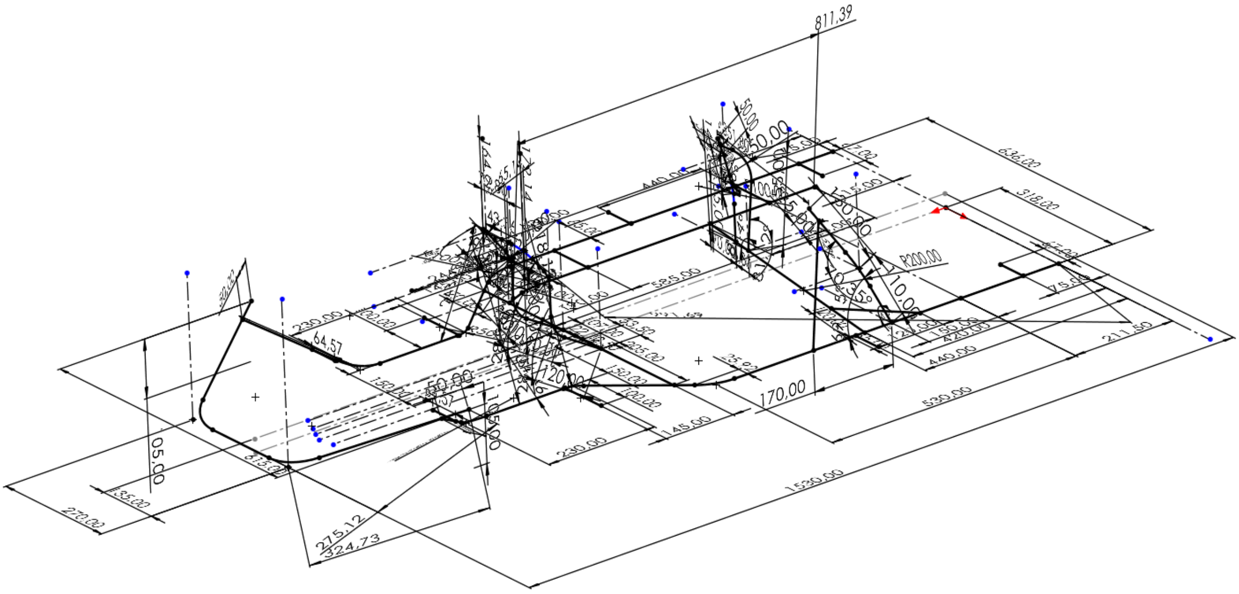

FIGURE 3.6: COMPLETE SKETCH OF THE CHASSIS.

For generating the tubular part, after the introduction of the correspondent line, the SolidWorks command “Sweep-Thin” is used which allows to select the diameter and the thickness of the pipe that needs to be introduced. Once generated the tubular frame, the junctions between:

- seat supports and the bracket for assembling the seat;
- steering supports and the bracket for fixing the steering wheel;

are created through the command “Boundary Boss/Base”.

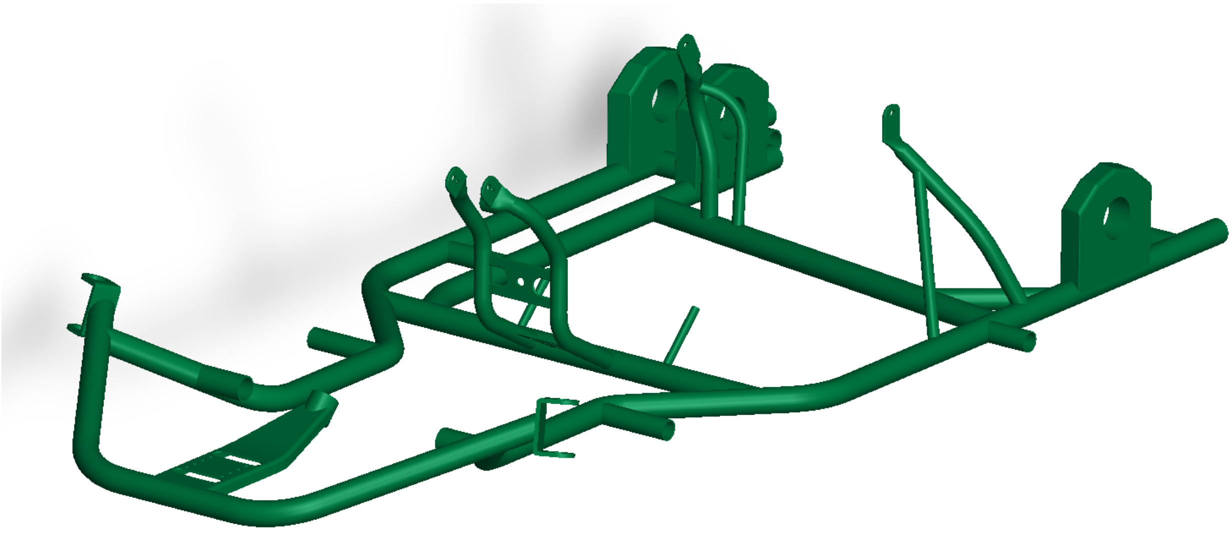

FIGURE 3.7: ISOMETRIC VIEW OF THE BODY FRAME 3D CAD MODEL.

3.1.3 Fixations sustaining the stub axles and caster angle.

It is very worth to be pointed out that the fixation sustaining the stub axle is welded to the frame pipe with an inclination angle of 16,9°: it is done for enhancing the caster angle, which is the axis inclination of the stub axle's screw.

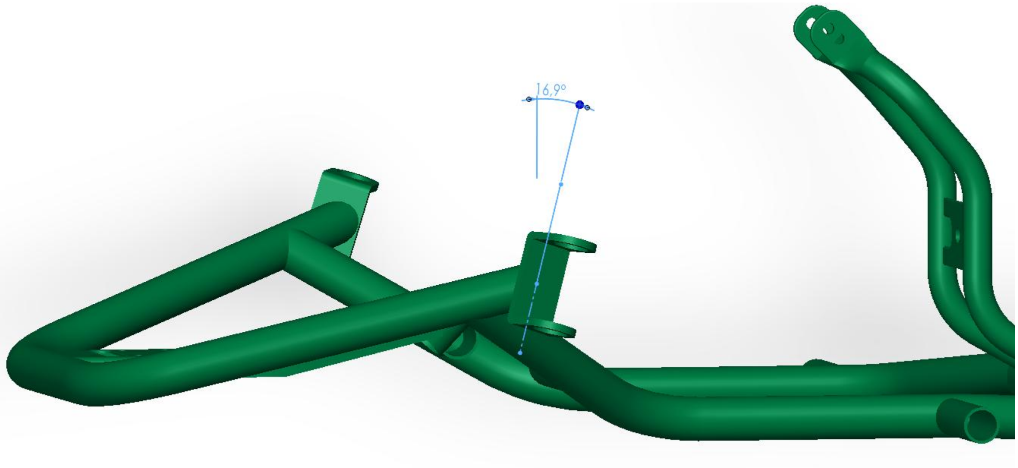

FIGURE 3.8: FIXATION SUSTAINING THE STUB AXLE INCLINATION ANGLE.

This angle has an important impact on the many times mentioned effect regarding the rising-up of the rear inner wheel while bending a curve. Indeed, the main role of the caster angle is to get the inner front wheel pulled down by a quantity proportional to the steering angle, while the outer front tyre is lifted-up by the same amount. Thus, part of the vertical load is transferred to the front inner wheel and the rear inner one gets more, if not completely, unloaded. Such essential feature given by the caster angle, can be even managed and modified on track as a function of the grip conditions thanks to the 20 holes eccentric bush, which is mounted on the upper and lower side of the stub axle support (image **3.9**).

FIGURE 3.9: 20 HOLES ECCENTRIC BUSH.

Rotating the eccentric bush, it can be changed the caster angle but even the camber angle, which is the inclination between the plane of the wheel and the vertical.

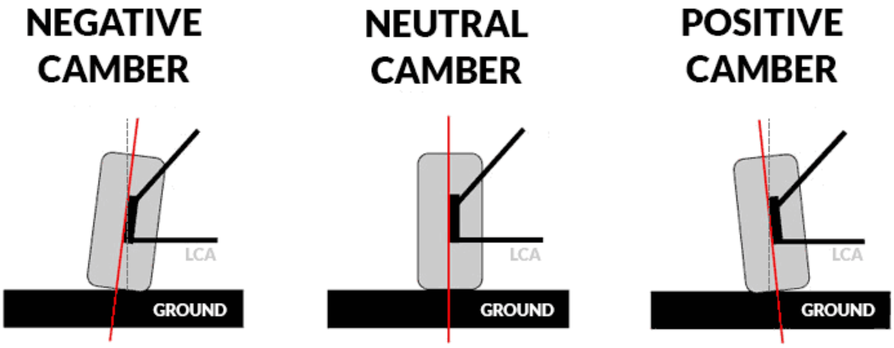

FIGURE 3.10: CAMBER ANGLE EXPLANATION.

Another operation that has been done, is the weighing of the chassis, made in the laboratory by a precision balance. The obtained result is the following.

FIGURE 3.11: CHASSIS WEIGHING OPERATION.

Due to the limited surface of the balance, a piece of wood has helped the measurement phase. So, from the value that can be seen on the balance display of 13.793 kg, must be subtracted the weight of the support in wood equal to 1.151 kg. But, for being as consistent as possible, it is even required to remove from the shown chassis weight, the one of each aluminium lower seat support that were mistaken assembled on the body frame during the weighing process, for obtaining the real naked chassis value:

$$m_{chassis} = (13.793 - 1.151 - 0.074 - 0.074)\,kg = 12.494\,kg.$$

3.2 Front ARB: OTK oval front bar

The front anti-roll bar employed in this work is the standard one provided by OTK group, the oval front bar $L = 275mm$ shown in the figure **2.9**. The 3D CAD model generation phase has been quick, owing to the simplicity of the component. Firstly, the oval geometry with the correct measures has been reported on a new sketch. Then, through the command "Boss-Extrude", the solid part with length of 275mm took shape. The last operation regards the using of "Cut-Extrude" command, for creating the hollow part of the bar.

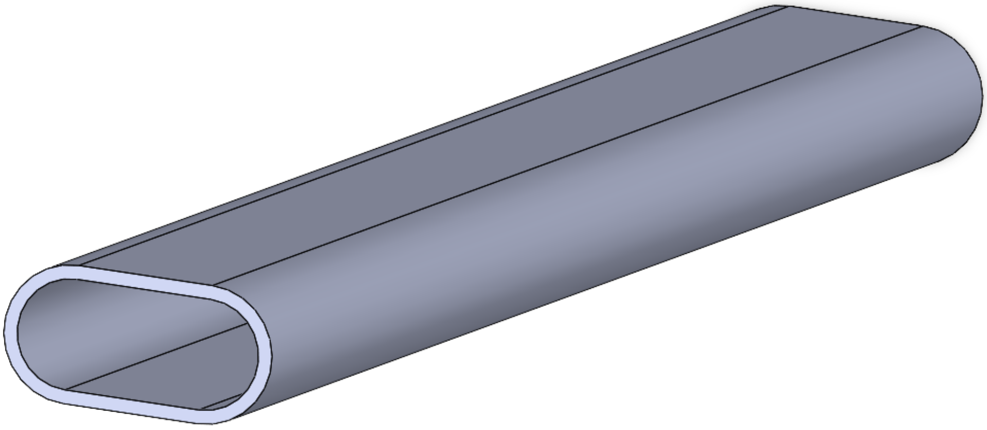

FIGURE 3.12: ISOMETRIC VIEW OF THE OVAL FRONT BAR 3D CAD MODEL.

For the front anti roll bar as well, the weight has been in laboratory detected (figure **3.13**), with a value of $m_{Front.ARB} = 0.2441\ kg$.

FIGURE 3.13: OVAL FRONT BAR WEIGHING OPERATION.

3.3 Seat: OTK standard and Greyhound brand new version

In this thesis work, 2 types of seats with completely different hardness have been taken under investigation:

- Standard OTK seat, well known for its rigidity.
- Greyhound brand new 2025 seat, called “crystal”, much softer and more flexible than the OTK standard one.

Indeed, thanks to the collaboration of “Greyhound racing seats” and its owner Alessandro, it was given to us the possibility of working on a brand new 2025 seat produced by the Greyhound factory, one of the most important company in the karting world for the manufacture of seat and other components in fiberglass (as floor pans, chain covers, air box filter water protection and so on). The particularity of this new seat stands into the innovative production process and material used by the company: the seat mould cavity is heated up to reach a temperature of 20°, then the fibre layers are applied with silicon-based glue and, the way by which this process is done will give the required final hardness to the seat. The core of the mould has a profile which perfectly reproduces the seat shape, so the mould is closed and a depression of 0.9 bar is applied. The next operation is the injection of the new resin called “crystal” and after 4 hours the mould is opened. Finally, the seat is put into an oven for 40 minutes for the drying phase.

The 3D CAD model of the seat is made by reproducing the side shape of the component on a new sketch. After that, the command “Boss-Extrude” is exploited for creating the 3D shape and, as last main operation, with the command “Shell”, the cavity for hosting the driver is designed.

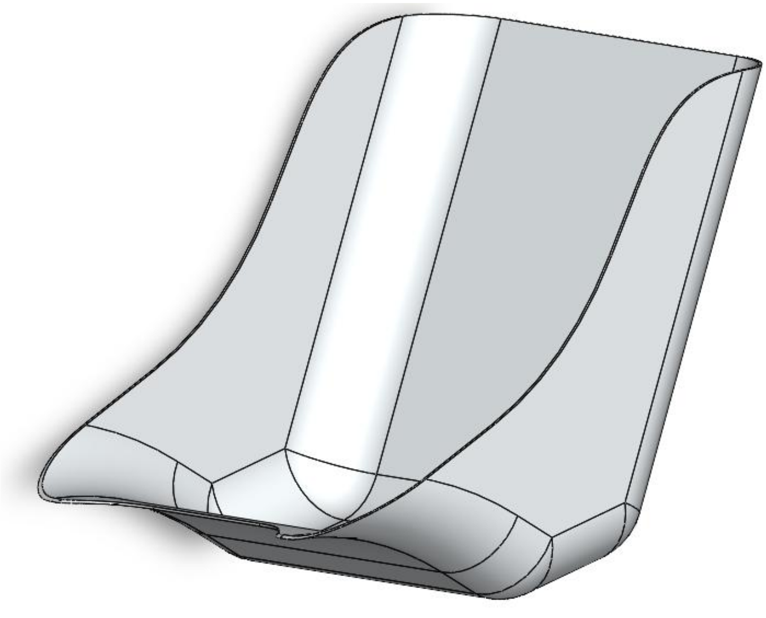

FIGURE 3.14: ISOMETRIC VIEW OF THE SEAT 3D CAD MODEL.

For both seats, the weighing phase has been done, the results are:

- Standard seat, $m_{std,seat} = 1.4076\ kg$.
- Greyhound seat, $m_{greyhound,seat} = 1.2737\ kg$.

FIGURE 3.15: STANDARD SEAT WEIGHING OPERATION.

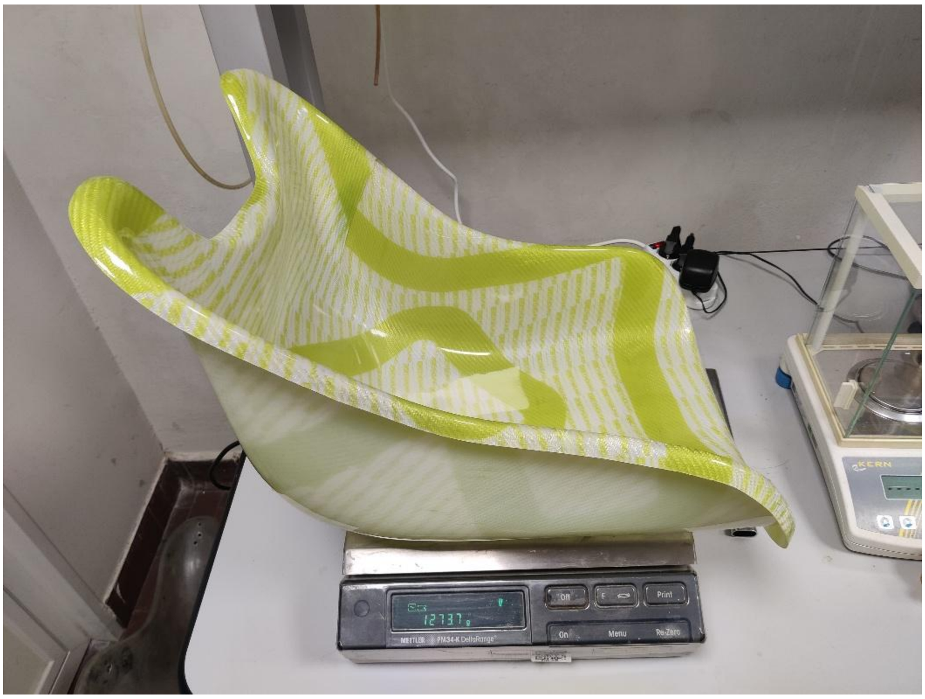

FIGURE 3.16: GREYHOUND SEAT WEIGHING OPERATION.

3.4 Rear axle: OTK standard N type

As well explained in the section **2.4**, there are a lot of different types of rear axle as a function of the hardness. The OTK standard N type is the one examined into this paper. It has hollow-cylindrical shape, with a diameter of $50mm$, thickness of $2mm$ and length of $1030mm$. Hence, for the 3D CAD model production, it has been followed the same path used for the creation of the chassis' pipes: a line with the same length of the axis is reported on a new sketch and then, the command "Sweep-Thin", has allowed the creation of the required hollow component.

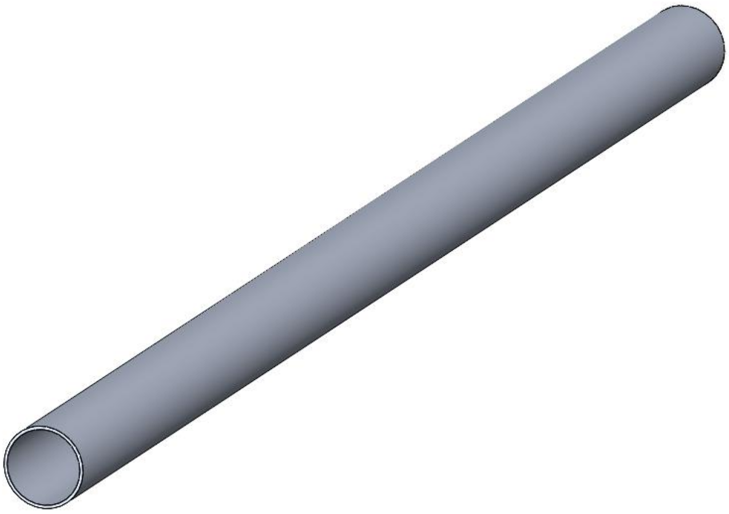

FIGURE 3. 17: ISOMETRIC VIEW OF THE REAR AXLE 3D CAD MODEL.

Following the same steps made for the previous components, the last operation is to weight the rear axle, gaining a value of $m_{Rear\ axle} = 2.4969\ kg$.

FIGURE 3.18: REAR AXLE WEIGHING OPERATION.

Chapter 4

4 FEA: Finite Element Analysis

The Ansys software website, defines Finite element analysis (FEA) as the process of predicting an object's behaviour based on calculations made with the finite element method (FEM). While FEM is a mathematical technique, FEA is the interpretation of the results provided by FEM. In practice, a finite element analysis, usually consists of three principal steps:

1. *Preprocessing:* The user constructs a model of the part to be analysed in which the geometry is divided into a number of discrete subregions, or "elements", connected at discrete points called "nodes".
2. *Analysis:* The dataset prepared by the preprocessor is used as input to the finite element code itself, which constructs and solves a system of linear or nonlinear algebraic equations.
3. *Postprocessing:* The user pores through reams of numbers and animations generated by the code, listing the modal displacements and stresses at discrete positions within the model.

In this chapter, as part of FEA, the numerical modal analysis following the pre-evidenced three steps has been done on the finite element model of all go-kart vehicle parts, with the aim of obtaining the dynamic properties of the component under investigation: natural frequencies and mode shapes.

4.1 LUPOS software: how it works

The software that has been employed to perform the numerical modal analysis is LUPOS, which is a LUmped Parameters Open-Source FEM code written completely in Matlab. It includes a list of useful tools for finite elements numerical analysis, in addition to a solver for several types of analysis. The approach followed in the software is similar to most FEM codes.

For first, it is necessary to generate a Matlab script (for description simplicity it is going to be called "ModelScript.m") where are introduced all the required input that allows to reproduce the shape and the dimensions of the part to be analysed: geometry (nodes and dofs) and elements (1D formulations such as Euler-Bernoulli or Timoshenko beams, rigid joints, etc. and 0D elements such as lumped masses, dampers, springs, etc.) to connect the nodes. These inputs are stored into the so called “Model” structure. A second Matlab script, with usually the same name of the one defined before but with the pre-name “Gui”, has the aim of containing all the simulation setup and of recalling the “ModelScript.m”.

Once launched the software, the typical graphical interface is the following:

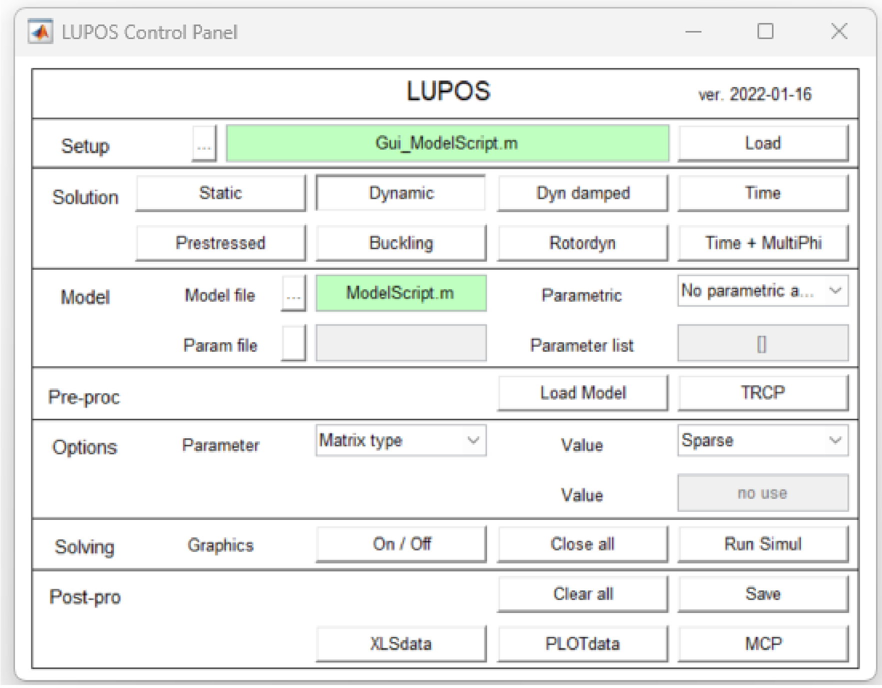
LUPOS Control Panel

LUPOS ver. 2022-01-16

Setup: Gui_ModelScript.m

Model file: ModelScript.m

Parametric: No parametric a...

Param file:

Parameter list: []

Parameter: Matrix type

Value: Sparse

Value: no use

FIGURE 4.1: LUPOS GRAPHICAL INTERFACE.

Thereby, after the loading of the named “Gui” script, the *Preprocessing* phase ends when the Model file “ModelScript” will be loaded through the command “Load Model”.

The intermediate step (*Analysis* process) is the conversion of the input data in matrices that are related also to the simulation choice, boundary conditions and additional parameters. These results are collected into the “Simul” structure of the “ModelScript.m”. This process starts when the command “Run Simul” is pressed.

Finally, the *Postprocessing* phase can be done through the Modal Control Panel (MCP), where it is possible to see the animation of the numerical mode shapes and the list of the natural frequencies.

With the aim of understanding the modal behaviour of all the kart vehicle components, the numerical modal analysis has been done for all the go-kart pieces which can be divided into two macro-categories: Main and Secondary components.

4.2 Main components

They are deeply described into the chapter **2** which, as well known, have structural function and affect the most the vehicle performances.

4.2.1 Chassis

To obtain a numerical model of the chassis, the nodes division of the real model must be carried out as first operation. The nodes selection has followed the idea of taking all the relevant points of the structure, such as curvature of the thin-walled pipes, welding zones and connection points with other elements (side bumper, front lower and upper bumper and so on and so forth). To simplify this acquisition phase, a handmade selection has been made naming the nodes with a precise numeration and different colours.

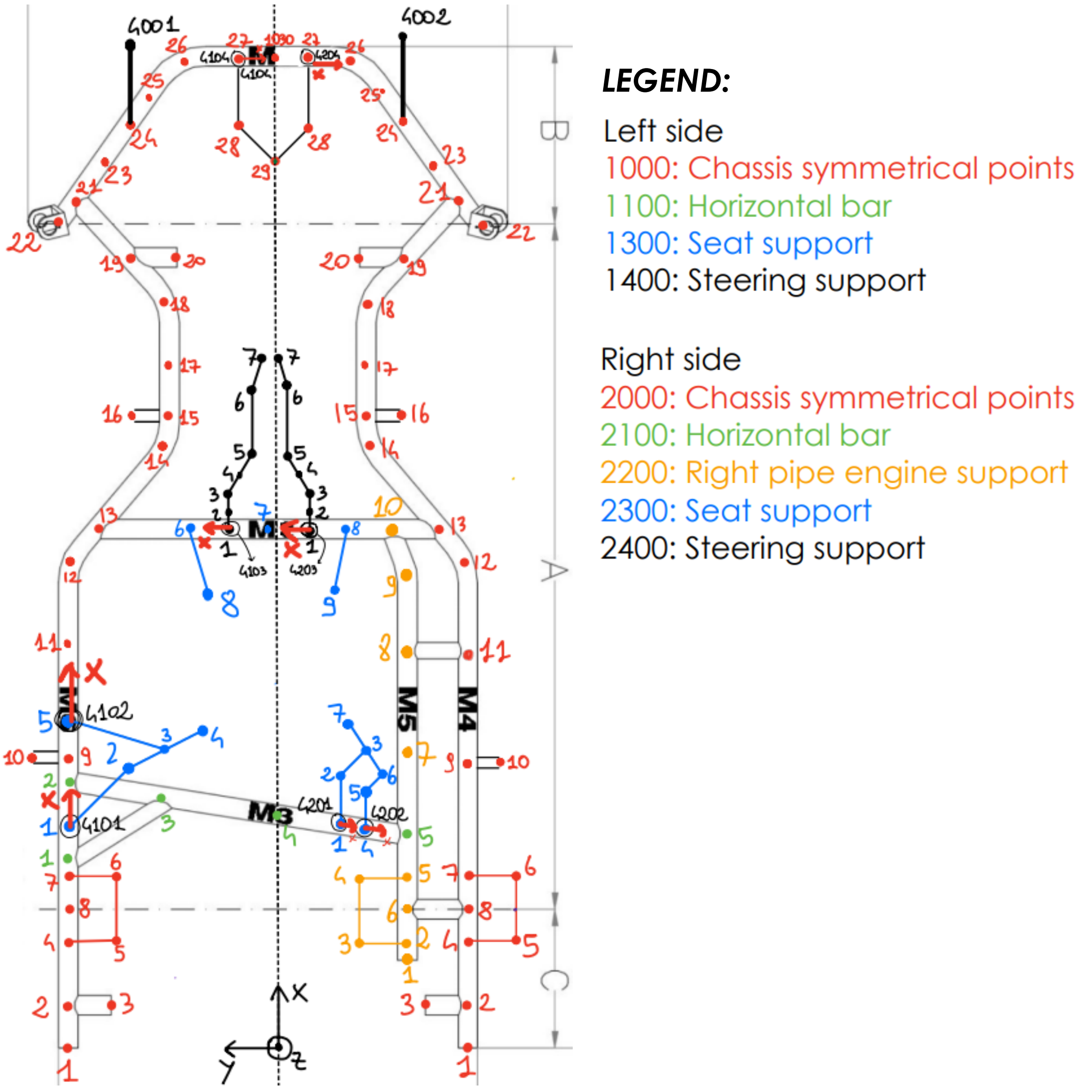

FIGURE 4.2: CHASSIS NODES DIVISION.

For getting the final node label observing the figure **4.2**, has to be added to the numeration present on the chassis, the quantity signed in the legend, which allows to make a distinguish among different parts of the body frame and between left and right-side nodes.

Then, exploiting the chassis 3D CAD model shown in the image **3.7**, the x,y,z coordinates of each pre-selected node could be seen through the command "Measure" (into the section "Evaluate").

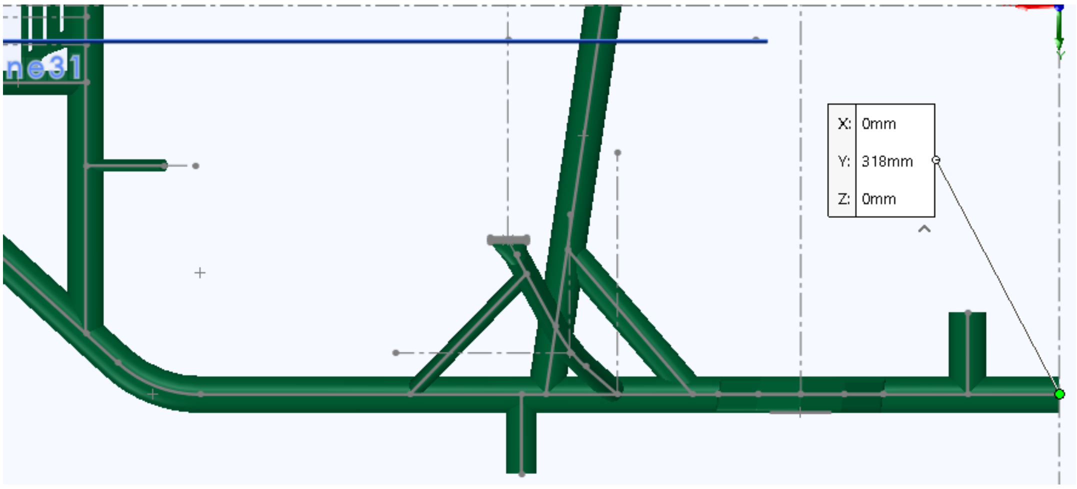

FIGURE 4.3: NODE 1001 X,Y,Z COORDINATES.

These coordinates have been copied and pasted into an excel file which contains in column the node ID and the x,y,z coordinates in millimetres.

NODE	ID	x	y	z
1	1001	0.000000	318.000000	0.000000

TABLE 4. 1: NODE 1001 STORED INTO THE EXCEL FILE.

Once generated the excel file with all the label and nodes coordinates, it can be loaded as input into the "Model" structure of the Matlab script, where it is needed to specify how the nodes are connected (just rods with different diameters but all with circular cross-section in this case) and the material as well. It was already mentioned in chapter **2** that, the variety of the material employed in the go-kart chassis production, is very wide. Since it is not known the material used by OTK group to produce the direct drive chassis, it has been hypothesized the using of AISI 4130, which is also called "chromoly steel" because of its chromium and molybdenum content in it. The chassis material properties reported as input into the model are the following:

- `rho_4130 = 7850; %material density         [kg/m3]`
- `E_4130 = 210e9;  %material Young's modulus [Pa]`
- `v_4130 = 0.30;   %material Poisson ratio`

But then, the real material properties value, will be discovered in the chapter **6**, during the model updating process of each component analysed in this chapter. All the insights previously reported, allows to complete the numerical model of the body frame. For being sure about the shape and geometry of the component for which the inputs are introduced, after the loading of the Model script into LUPOS environment, it is possible to plot the final configuration by clicking on "TRCP" (Test Rig Control Panel, in the pre-processing section of the LUPOS graphical interface, figure **4.1**). The animation that will be presented is displayed in the following image **4.4**.

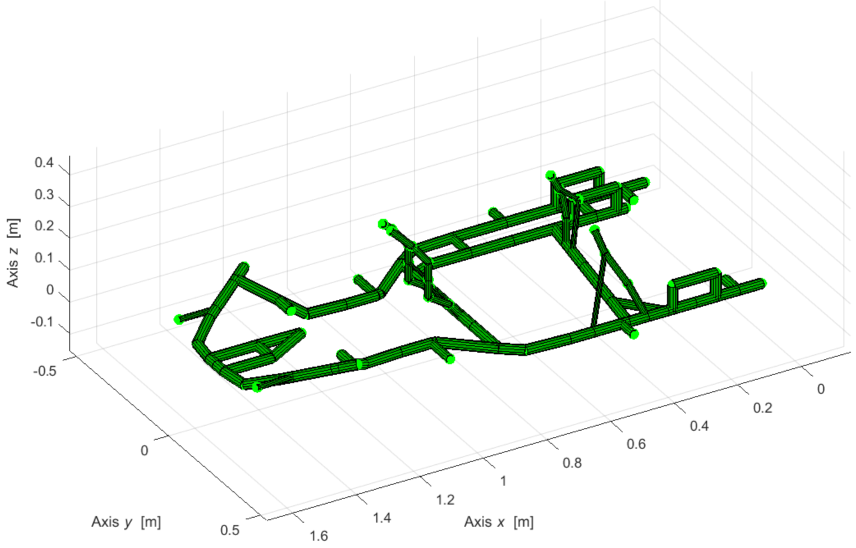

Figure 4.4: TRCP output of chassis numerical model.

Then, the next operation regards the option setup of numerical simulation, where as parameter is chosen "matrix type", as value is selected "sparse" (they can be seen in the Options section of image **4.1**). Finally, the numerical simulation can be run, obtaining as output the first 20 modes shape with the correspondent natural frequencies. The number of the modes printed by the modal control panel is an option variable that can be changed into the simulation setup "Gui" script, modifying: `Simul.num_modes = '20';`

The first 6 modes with natural frequency different from zero, are now reported in the following picture.

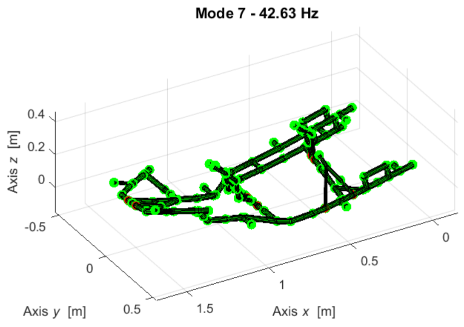

Figure 4.5: mode 7 = 42.63 Hz

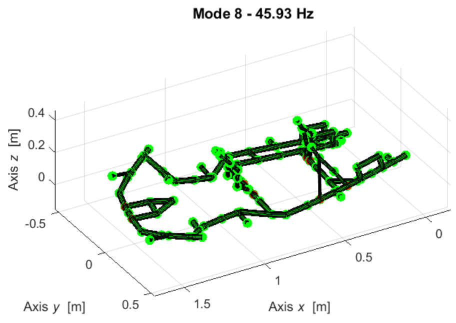

Figure 4.6: Mode 8 = 45.93 Hz

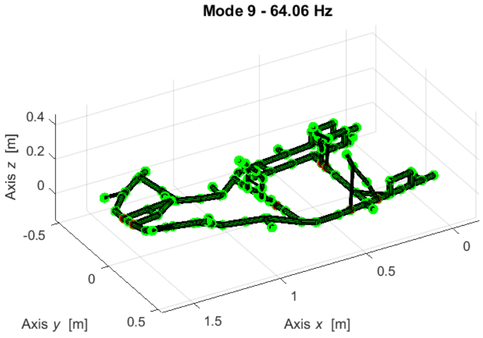

FIGURE 4.7: MODE 9 = 64.06 HZ

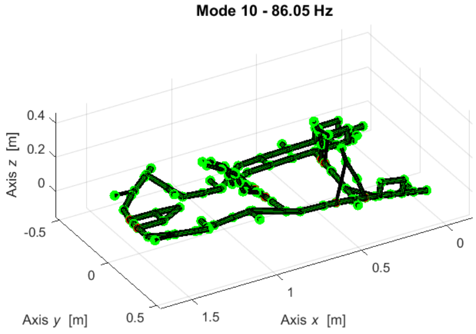

FIGURE 4.8: MODE 10 = 86.05 HZ

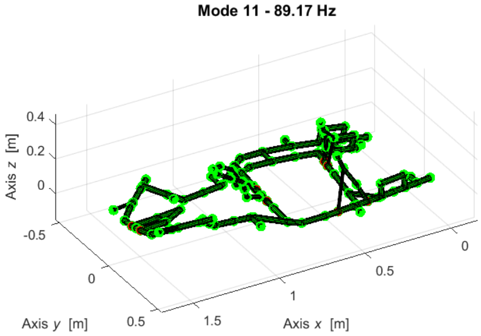

FIGURE 4.9: MODE 11 = 89.17 HZ

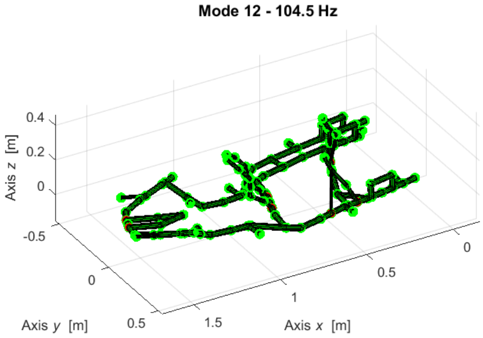

FIGURE 4.10: MODE 12 = 104.5 HZ

Mode - Chassis	Frequency [Hz]	Mode Shape
Mode 1	0	Rigid Body
Mode 2	0	Rigid Body
Mode 3	0	Rigid Body
Mode 4	0	Rigid Body
Mode 5	0	Rigid Body
Mode 6	0	Rigid Body
Mode 7	42.63	1st Bending
Mode 8	45.93	1st Torsion
Mode 9	64.06	2nd Bending
Mode 10	86.05	2nd Torsion
Mode 11	89.17	3rd Torsion
Mode 12	104.5	3rd Bending

TABLE 4. 2: CHASSIS NUMERICAL NATURAL FREQUENCIES.

From mode 1 to mode 6, the natural frequency is equal to zero since they are referred to rigid body modes.

4.2.2 Front ARB

The next component to numerically analyse is the oval front bar by OTK group. The nodes division has been performed just over the length of the bar, equal to 273.5mm. For this reason, a node each 25mm is introduced, considering the z-axis the one through which the beam is oriented.

This kart vehicle part is much simpler than the chassis, as a matter of fact it can be modelled with a rod that has elliptical cross-section, linking one by one each node.

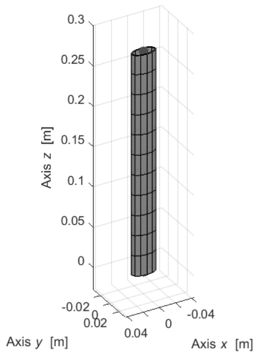

FIGURE 4.11: TRCP OUTPUT OF FRONT ARB NUMERICAL MODEL.

Regarding the material, it is supposed the employment of structural steel. In the following, are listed the material properties and even the geometrical dimensions:

- `rho_ARB = 7850; %material density  [kg/m3]`
- `E_ARB = 200e9;  %Young's modulus   [Pa]`
- `v_ARB = 0.30;   %Poisson’s ratio`
- `t_ARB = 0.0015; %ARB thickness     [m]`
- `Dy_ARB = 0.03;  %Dimension along y [m]`
- `Dz_ARB = 0.015; %Dimension along z [m]`

As numerical simulations results, are taken the first 4 mode shapes with a natural frequency different from zero:

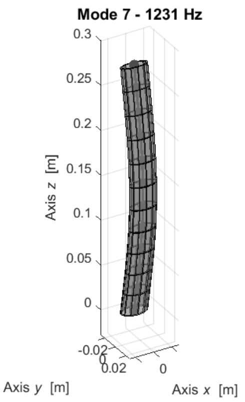

FIGURE 4.12: MODE 7 = 1231 HZ

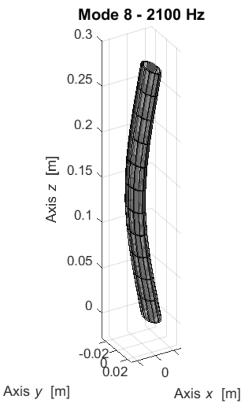

FIGURE 4.13: MODE 8 = 2100 HZ

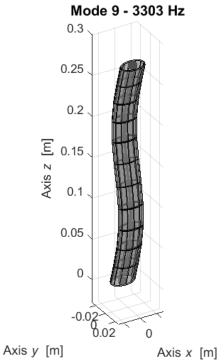

FIGURE 4.14: MODE 9 = 3303 HZ

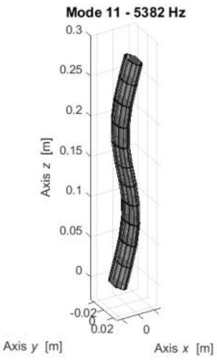

FIGURE 4.15: MODE 11 = 5382 HZ

Modes - Front ARB	Frequency [Hz]	Mode Shape
Mode 1	1231	1st Bending - YZ plane
Mode 2	2100	1st Bending - XZ plane
Mode 3	3303	2nd Bending - YZ plane
Mode 4	5382	2nd Bending - XZ plane

TABLE 4.3: FRONT ARB NUMERICAL NATURAL FREQUENCIES.

4.2.3 Seat

The third main component to study is the seat. As deeply explained into the chapter **3** about the reverse engineering process, a CAD model of this kart vehicle part has been developed. It is a key element because has helped a lot in this numerical analysis part. In fact, for modelling such a complex thin-walled component, a first solution could be found by using the LUPOS 2D shell elements connected through 3 or 4 nodes (called "Sh3" and "Sh4" elements). It would means consider just a mid-surface of the seat where a nodes split is present. Unfortunately, they do not work well at the moment since a developing phase is present on them. Perhaps, the focus has been directly switched to the "Hexa" 3D solid elements. They can be defined as a link between a pair of 4 nodes where, the distance between them, defines the seat thickness.

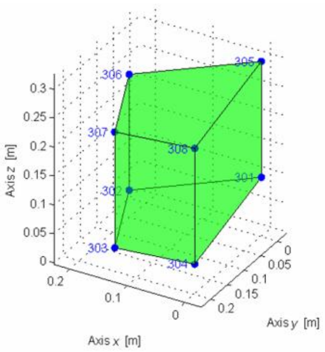

FIGURE 4.16: LUPOS HEXA SOLID ELEMENT.

Thereby, a nodes division is needed on both surfaces of the seat in order to make possible the utilization of those kind of Hexa solid elements. For making quite simple this process, it has been decided to leverage the Hypermesh software: the SolidWorks part of the seat has been imported and meshed using the command 3D-THIN SOLID MESH. The mesh is created by first generating a 2D mesh on a selected set of source faces, and then extruding this mesh to generate solid Hexa.

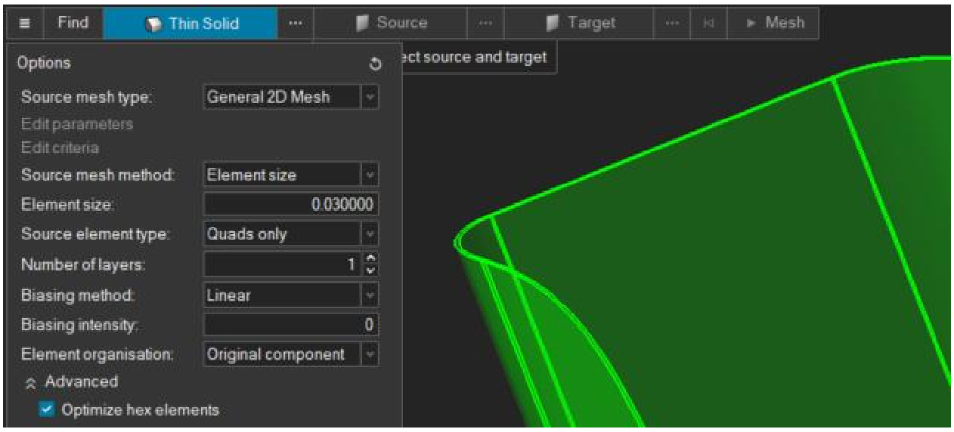

Source mesh type: General 2D Mesh
Source mesh method: Element size
Element size: 0.030000
Source element type: Quads only
Number of layers: 1
Biasing method: Linear
Biasing intensity: 0
Element organisation: Original component
☑ Optimize hex elements

FIGURE 4.17: MESH OPTIONS.

As it is shown in figure **4.17**, the mesh options are defined starting from element size of 30mm for the first trial, then other two tests have been done reducing respectively the mesh size. The type of elements used to create the source mesh must strictly be of the “Quads only” type, since it is the only way to try to get CHEXA8 elements.

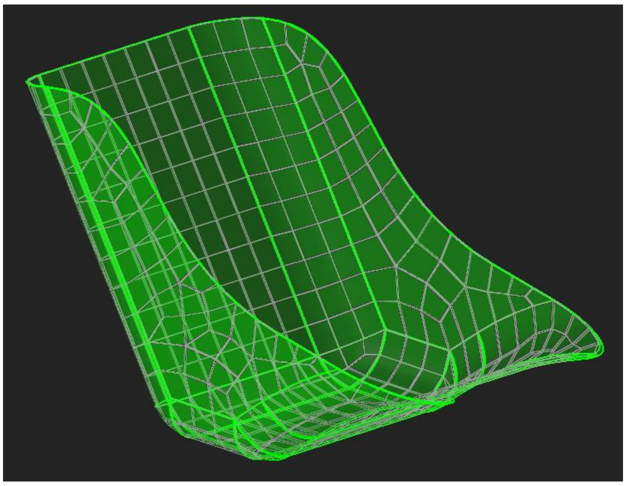

FIGURE 4.18: 3D MESH OF THE SEAT.

It is very important to be verified, after the Mesh creation, that all the elements created are of CHEXA8 typology because, the selection “Quads only” in the mesh options (image **4.17**) does not completely guarantee to obtain as output a mesh of CHEXA elements (figure **4.19**), owing to problems that the software can meet during the mesh generation for a certain Element size. For example, trying to use a mesh size of 10mm the obtained elements are visible in picture **4.20**, both CHEXA and CPENTA.

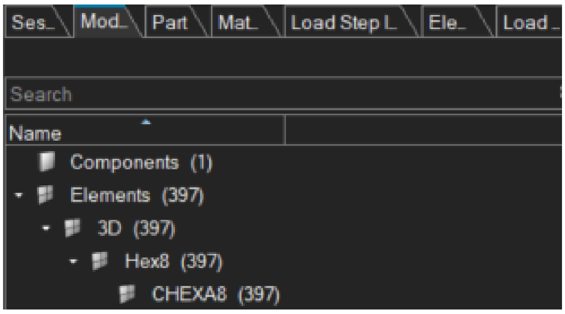

FIGURE 4.19: ONLY CHEXA8 ELEMENT

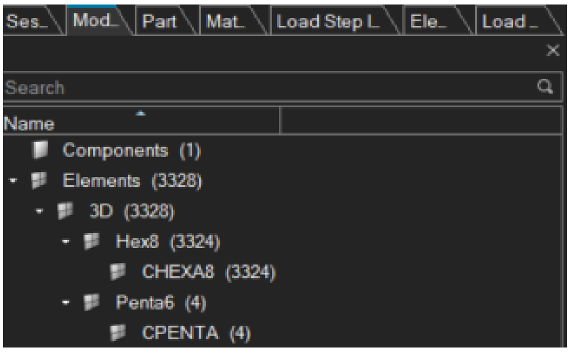

FIGURE 4.20: BOTH CHEXA8 AND CPENTA ELEMENTS

So, since the Hexa solid elements in LUPOS environment define a link between eight nodes, a discretization like the one shown at figure **4.20** cannot be used because only CHEXA elements can be well translated in LUPOS as hexahedral interconnection. For this reason, the 3 elements mesh sizes that match all the requirements defined up to now are:

- 9mm;
- 21mm;
- 30mm.

Then, a Free-Free modal analysis has been performed in Hypermesh for each listed mesh type.

It is very worth to be pointed out that a 2D mesh type is more suitable for the seat: being it a thin-walled component (since the thickness is much lower than other two dimensions, length and width), shell elements are much more indicated if compared with solid elements. Indeed, the main problem of these “Hexa” solid elements is that, along the thickness, it is better to have more than 1 layer of discretization, otherwise the final component will result stiffer (trouble that is not present with 2D elements, where the mesh is generated on the only one midplane). In this case study, as shown in figure **4.16**, along the thickness, no layers of discretization are present, since the "Hexa" solid elements of LUPOS does not foresee the presence of one or more intermediate discretization layers.

For this reason, in order to find which one of the 3D mesh sizes listed before matches the convergency conditions, the results obtained from the eigenvalue analysis with a 3D mesh, must be compared with the normal modes analysis performed on components characterized by a 2D mesh type (so with "Tria" elements) and similar element size (ES). All the simulations for this comparison have been performed on hypermesh.

	FREQUENCIES [Hz]		FREQUENCIES [Hz]		FREQUENCIES [Hz]	
MODE	2D CTRIA – ES=10mm	3D CHEXA - ES=9mm	2D CTRIA - ES=20mm	3D CHEXA - ES=21mm	2D CTRIA - ES=30mm	3D CHEXA - ES=30mm
1	32.3	33	32.7	38.7	33	54
2	63.8	64.8	64.1	71.9	64.4	85.5
3	114.5	116.7	114.9	132.1	115.2	161.6
4	147.1	150.5	148.9	178.1	150.6	226.6

TABLE 4.4: 2D VS 3D MESH TYPE.

A consideration that comes from finite elements theory can be done seeing the table **4.4**: normally, reducing the number of elements (and so, increasing the mesh size), the user is "adding" numerical stiffness.

$$\boldsymbol{f} = \sqrt{\frac{\boldsymbol{k}}{\boldsymbol{m}}} \tag{4.1}$$

From the formula of the frequency (**4.1**), is demonstrated what said before: being constant the mass m, the only remained variable is the stiffness k. This is due to the fact that, theoretically, each component is made by infinite degrees of freedom and, through the discretization, the number of degrees of freedom is reduced to a finite number. Perhaps, the higher is the mesh size, the lower will be the number of degrees of freedom of the system under investigation, which results in a higher numerical stiffness.

Hence, after all the previous discussion, the 3D mesh which matches the convergency requirements, is the one with $ES = 9\ mm$, since the percentual error is about 2% for each modes shape if compared to 2D mesh. So, the selected meshed file .fem, has been exported.

Subsequently, the file extension has been changed from. fem to .bdf for exploiting the code "BDFtoLUPOS.p", a FEM tool which allows to translate the Hypermesh results into LUPOS input files to be loaded inside the seat "Model" struct (seat nodes coordinate and solid Hexa elements).

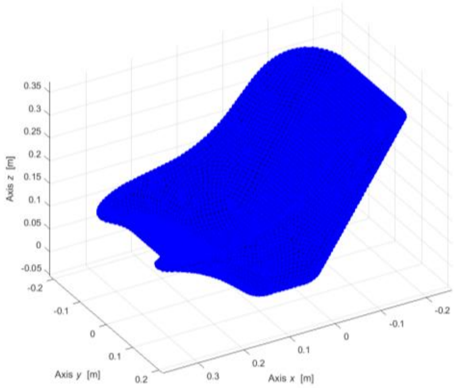

FIGURE 4.21: TRCP OUTPUT OF SEAT NUMERICAL MODEL.

In terms of material, it has been hypothesized the using of E-glass fiber, since it is appropriate for seat production:

- `rho_seat = 2540; %material density [kg/m3]`
- `E_seat = 72.4e9; %Young's modulus  [Pa]`
- `v_seat = 0.20;   %Poisson's ratio`
- `t_seat = 0.002;  %Seat thickness   [m]`

All is now ready to perform the numerical modal analysis with LUPOS, which has given the following results:

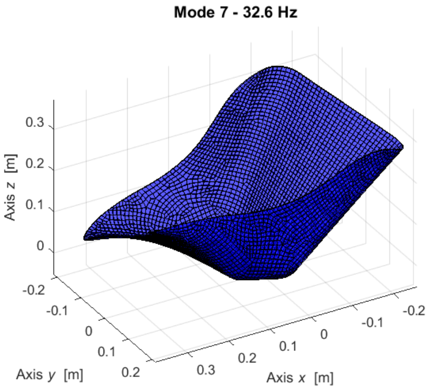

FIGURE 4.22: MODE 7 = 32.6 HZ

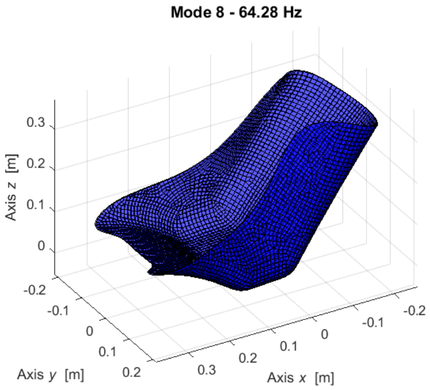

FIGURE 4.23: MODE 8 = 64.28 HZ

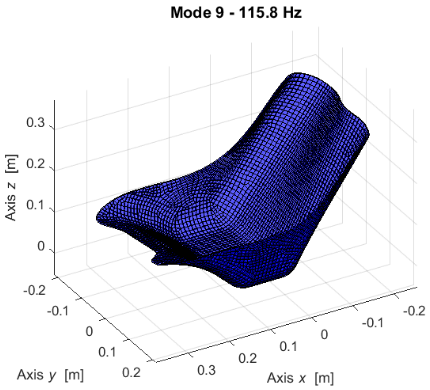

FIGURE 4.24: MODE 9 = 115.8 HZ

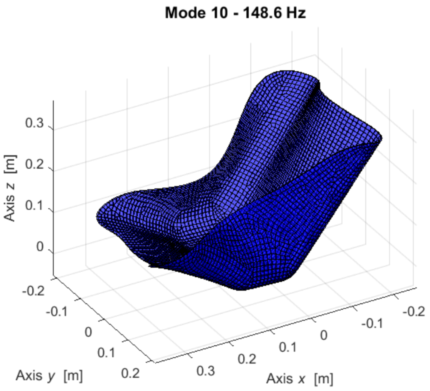

FIGURE 4.25: MODE 10 = 148.6 HZ

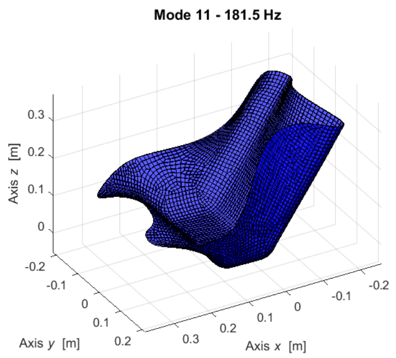

FIGURE 4.26: MODE 11 = 181.5 HZ

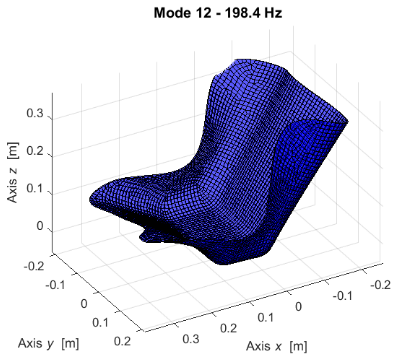

FIGURE 4.27: MODE 12 = 198.4 HZ

Mode - Seat	Frequency [Hz]	Mode Shape
Mode 1	32.6	1st Torsion
Mode 2	64.3	1st Bending
Mode 3	115.8	2nd Bending
Mode 4	148.6	3rd Bending
Mode 5	181.5	4th Bending
Mode 6	198.4	5th Bending

TABLE 4.5: SEAT NUMERICAL NATURAL FREQUENCIES.

4.2.4 Rear axle

The last main component of the kart vehicle regards the rear axle. It has a quite simple geometry, since it is a hollow cylindrical beam with round cross section. The nodes split has been done in same way described for the front anti-roll bar, so putting 22 nodes along the only z-axis: starting from the bottom ($z = 0$), a node each $50mm$ has been introduced over the length of the axle, equal to $1030mm$ ($z = 1030$).The link between the nodes, can be made leveraging the rod elements with circular cross section.

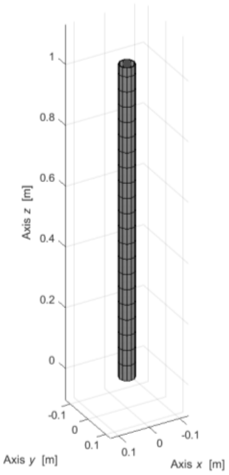

FIGURE 4.28: TRCP OUTPUT OF REAR AXLE NUMERICAL MODEL.

In terms of material, one of the most adequate concerns the AISI 1020, for its high machinability, high strength, high ductility. The material elastic properties and the main geometrical dimensions are:

- `rho_axle = 7870;  %material density  [kg/m3]`
- `E_axle = 205e9;   %Young's modulus   [Pa]`
- `v_axle = 0.29;    %Poisson's ratio`
- `t_axle = 0.002;   %axle thickness    [m]`
- `Dy_axle = 0.05;   %Dimension along y [m]`
- `Dz_axle = 0.05;   %Dimension along z [m]`

LUPOS numerical simulation results, considering as always the first six modes shape with no-null natural frequency, are the following:

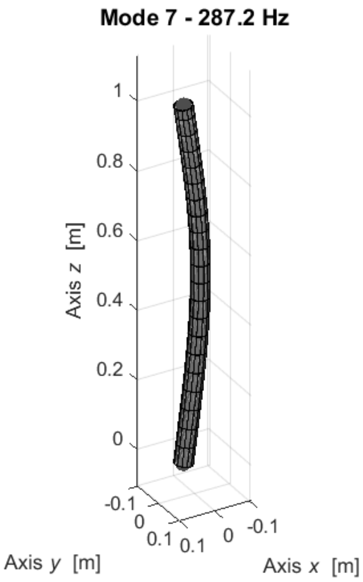

FIGURE 4.29: MODE 7 = 287.2 HZ

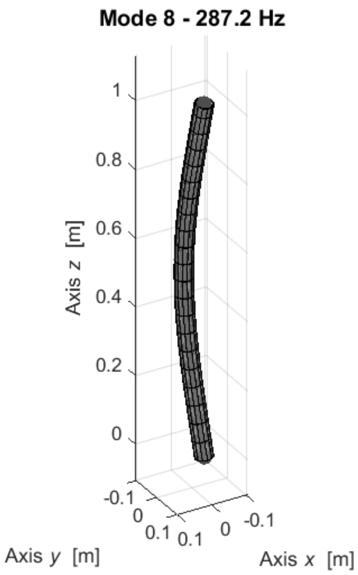

FIGURE 4.30: MODE 8 = 287.2 HZ

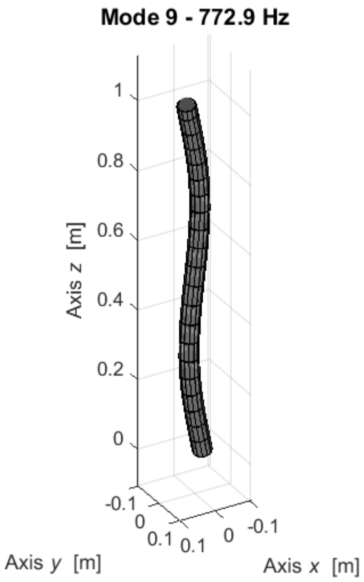

FIGURE 4.31: MODE 9 = 772.9 HZ

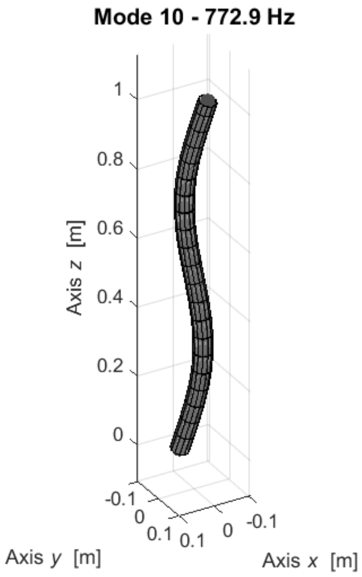

FIGURE 4. 32: MODE 10 = 772.9 HZ

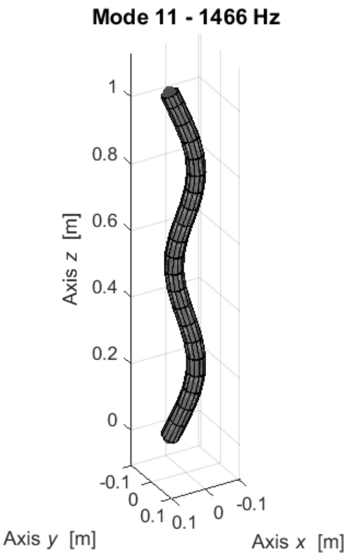

Figure 4.33: mode 7 = 1466 Hz

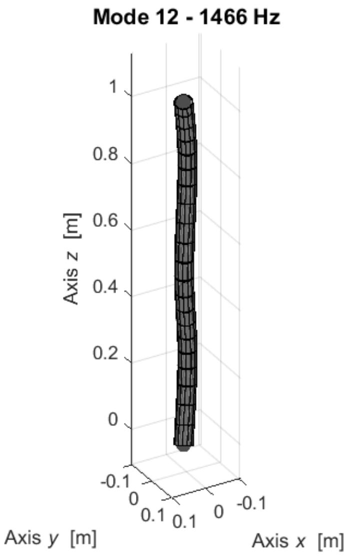

Figure 4.34: mode 12 = 1466 Hz

Mode - Front ARB	Frequency [Hz]	Mode Shape
Mode 1	287.2	1st Bending - 1st plane
Mode 2	287.2	1st Bending - 2nd plane
Mode 3	772.9	2nd Bending - 1st plane
Mode 4	772.9	2nd Bending - 2nd plane
Mode 5	1466	3rd Bending - 1st plane
Mode 6	1466	3rd Bending - 2nd plane

Table 4.6: Rear axle numerical natural frequencies.

As it is displayed into table **4.6**, the natural frequencies are equal in pairs of two, starting from 1st and 2nd, then 3rd and 4th and so on and so forth. It is an expected result since the rear axle is an axisymmetric component. It means that, the 1st bending in two different plane shows same value of natural frequency.

4.3 Secondary components

In this section, the idea is to analyse the modal behaviour of some components which are fundamental as well but less impactful on the dynamic behaviour of the complete kart vehicle. It was previously said that the steering system affect the dynamic response of the chassis, as the rising-up of the rear inner wheel thanks to the caster angle or the tyre contact patch through the camber angle. But the upcoming evaluation is more interesting for investigate the resonance and keep the structure of these components far away from the resonance itself, which results in stability of the go-kart and in good vibrational absorptivity. It means, for example, avoid the quiver of the steering wheel, which can be felt by the driver.

4.3.1 Floor panel

The floor panel has the sustaining function for the tank and for the driver's feet. It is connected through bolts to the body frame in 5 points and has the shape shown in figure **4.21**.

FIGURE 4.35: ISOMETRIC VIEW OF THE FLOOR PANEL MADE BY OTK GROUP.

Since this component creates a connection among the front tubular part of the chassis, it could affect the dynamic deformation of the body frame only if its stiffness is very high. Instead, the main employed materials are:

- Aluminium, with a thickness of 2*mm*;
- Carbon fibre;
- Fiberglass.

So, it is a highly deformable kart part whose effect on the overall tube torsion and load transfer can be considered negligible.

Being the floor panel a thin-walled component as the seat, a 3D CAD model has been created in order to perform the same steps followed the generation of the numerical model and successive numerical simulation of the seat itself.

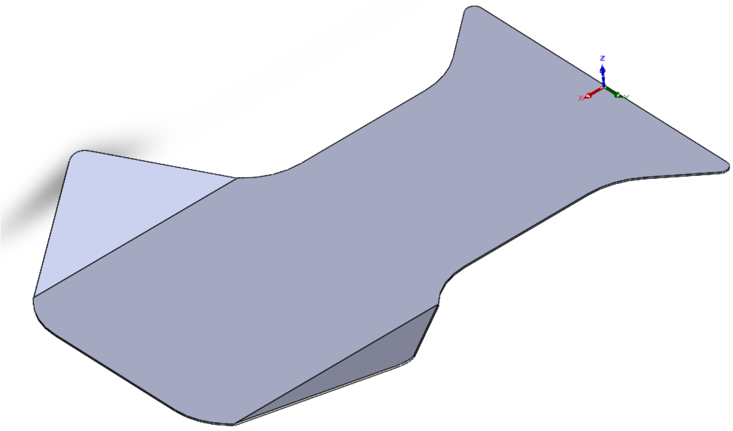

FIGURE 4.36: ISOMETRIC VIEW OF THE FLOOR PANEL 3D CAD MODEL.

Then, as deeply explained in the section **4.2.3**, it has been leveraged the Hypermesh software for creating a 3D mesh. Afterward, the finding of the mesh elements size convergency took place, comparing the Free-Free eigenvalue analysis performed with 3D meshes and with more suitable 2D meshes.

	FREQUENCIES [Hz] - ELEMENT SIZE: 10mm		FREQUENCIES [Hz] - ELEMENT SIZE: 21mm		FREQUENCIES [Hz] - ELEMENT SIZE: 30mm	
MODE	CTRIA	CHEXA	CTRIA	CHEXA	CTRIA	CHEXA
1	22.64	23.44	22.68	24.39	22.72	26.88
2	24.55	25.23	24.57	26.47	24.48	29.86
3	55.54	56.93	55.51	59.2	55.38	62.76
4	60.16	62.21	60.07	67.52	59.85	76.62
5	76.85	79.58	77.08	86.46	77.18	97.18
6	101.97	104.85	102.05	108.37	100.85	117.76
7	113.99	119.54	114.23	133.57	113.75	151.52
8	134.19	139.23	133.94	154.63	133.09	175.96
9	144.77	150.06	144.06	167.64	143.32	195.92
10	155.13	159.47	155.06	172.07	154.63	198.53

TABLE 4.7: 2D VS 3D MESH TYPE.

Evaluating the percentage error, the lowest value is found choosing the 3D mesh with element size of 10*mm,* with an error that ranges from 3.5% to 3.99% if the first 10 modes shape are taken into account. Hence, the selected meshed component file .fem, has been exported with a consequently changing of the file extension from .fem to .bdf, for exploiting the FEM tool "BDFtoLUPOS.p". Once loaded into the "Model" struct the nodes coordinate and the solid Hexa elements subdivision, the LUPOS test rig control panel output is the following:

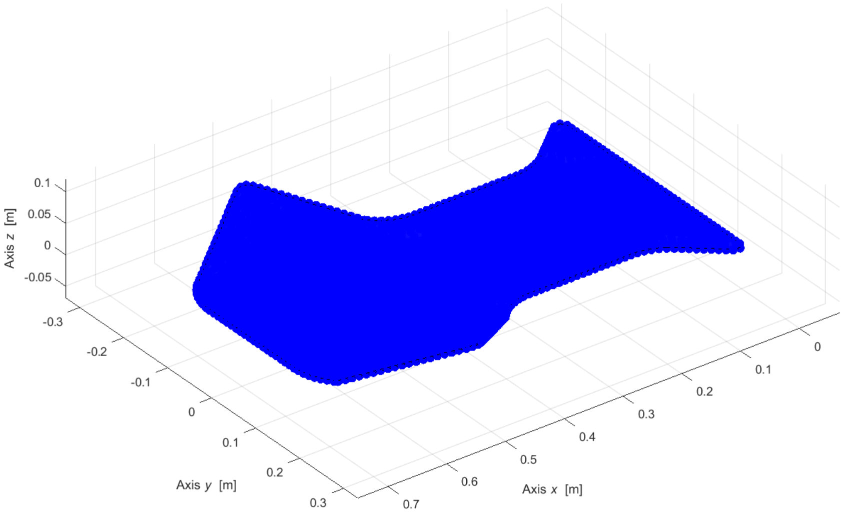

FIGURE 4.37: TRCP OUTPUT OF FLOOR PANEL NUMERICAL MODEL.

The image **4.37**, appears full blue coloured due to the presence of 4934 nodes. The material introduced into the numerical model is the standard employed by OTK group for the floor panel production, Aluminum:

- `rho_seat = 2689.8; %material density      [kg/m3]`
- `E_seat = 68.3e9;    %Young's modulus       [Pa]`
- `v_seat = 0.34;      %Poisson's ratio`
- `t = 0.002;          %floor panel thickness [m]`

The weighing operation has been made for the floor panel as well, for checking before running the simulation, if the numerical model weight fits well the reality: this numerical weight check has been even made for each component numerically analysed up to now.

FIGURE 4.38: FLOOR PANEL WEIGHING OPERATION.

The numerical simulation results given as LUPOS' output are shown in the next pictures.

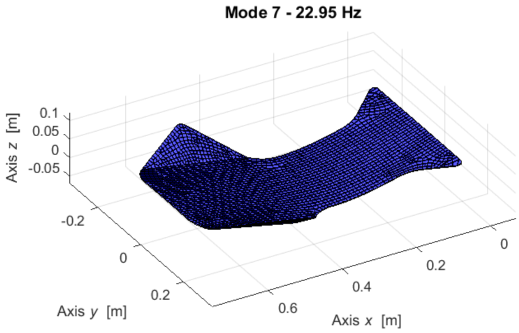

FIGURE 4.39: MODE 7 = 22.95 HZ

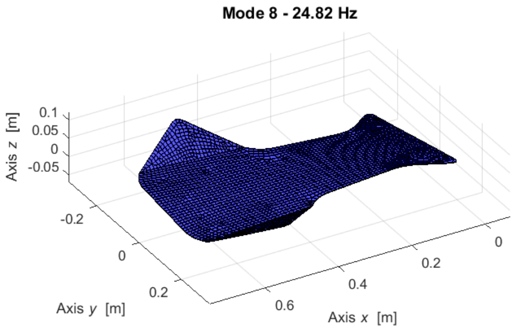

FIGURE 4.40: MODE 8 = 24.82 HZ

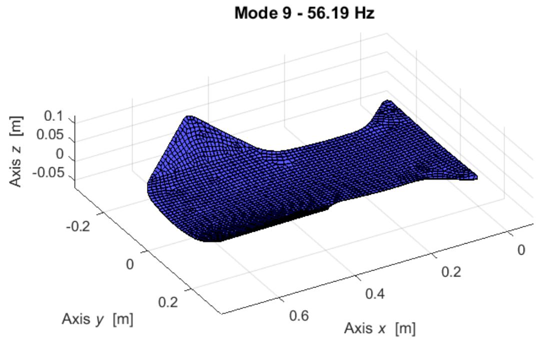

FIGURE 4.41: MODE 9 = 56.19 HZ

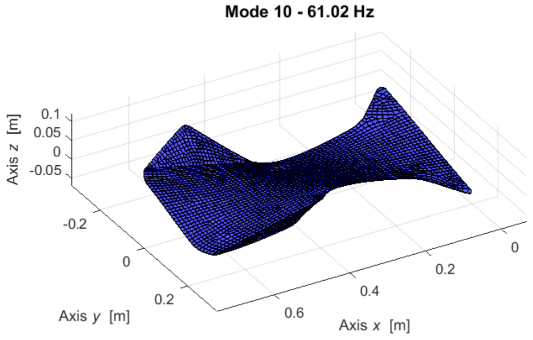

FIGURE 4.42: MODE 10 = 61.02 HZ

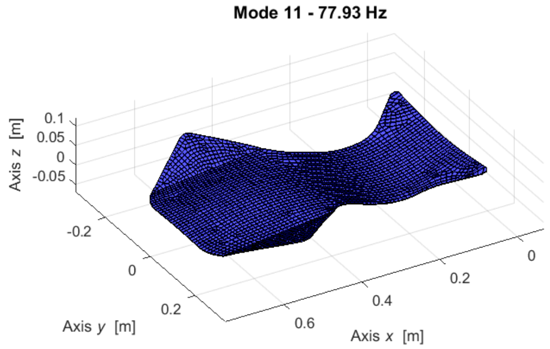

FIGURE 4.43: MODE 7 = 77.93 HZ

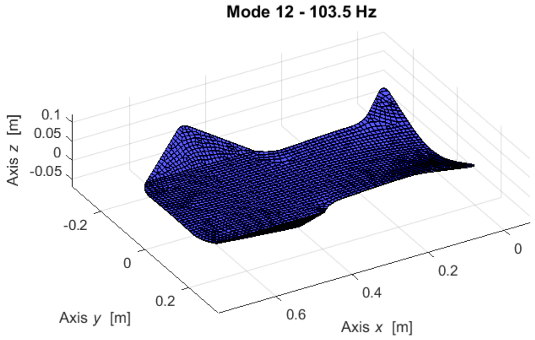

FIGURE 4.44: MODE 12 = 103.5 HZ

Mode - Floor panel	Frequency [Hz]	Mode Shape
Mode 1	22.95	1st Bending
Mode 2	24.82	1st Torsion
Mode 3	56.19	2nd Bending
Mode 4	61.02	2nd Torsion
Mode 5	77.93	3rd Bending
Mode 6	103.5	4th Bending

TABLE 4.8: FLOOR PANEL NUMERICAL NATURAL FREQUENCIES.

4.3.2 Steering column

The steering column is the component which solidly rotate with the steering wheel when the driver gives the rotation angle input. The main difference if compared with a racing car vehicle, stands in the simplicity of the go-kart steering system. Indeed, there is not the presence of pinion-gear system for transmitting the movement to the other components. The go-kart steering system is composed of just 3 elements rigidly connected by means of bolts and joinballs (only where necessary, to reduce frictions):

1. Steering column;
2. Steering tie-rod;
3. Stub-axle.

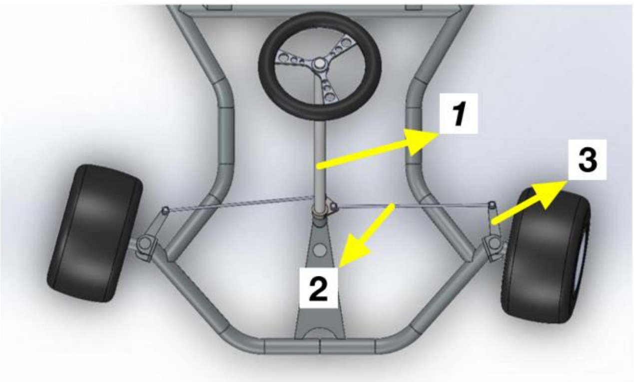

FIGURE 4.45: THREE MAIN ELEMENTS OF A GO-KART STEERING SYSTEM.
STEERING COLUMN (1), STEERING TIE-ROD (2) AND STUB-AXLE (3).

As a matter of fact, the geometry of the steering column is straightforward since is made by a hollow-cylindrical beam with circular cross section. Moreover, it presents 2 brackets in the lower side to host the bolts connection with the tie-rods.

FIGURE 4.46: ISOMETRIC VIEW OF THE STEERING COLUMN MADE BY OTK GROUP.

Even in this case, the nodes division is made through the length of the component, equal to 495mm, positioning 9 points with only z-coordinate different from zero and 1 node in the middle of the brackets to emulate the connection point with tie-rods. For generating the numerical model, as already done for similar components, rod element with rounded cross-sections has been implemented for linking each node.

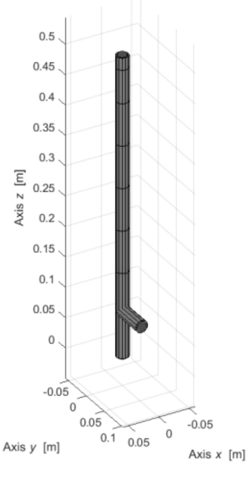

FIGURE 4.47: TRCP OUTPUT OF STEERING COLUMN NUMERICAL MODEL.

The supposed material deployed for the manufacturing of the steering column is the AISI 1018, which is less strength than of both structural steel and body frame material. The employment of such AISI 1018 which has a yield point lower if compared with the one of the chassis, has a particular meaning: in case of crash or contact with other vehicles in the front side of the go-kart, the kinetic energy has to be absorbed mainly from the steering system's components in order to avoid plastic deformations of the tubular frame. The material properties of AISI 1018 and the main geometrical dimensions are:

- `rho_SteerCol = 7850;  %material density          [kg/m3]`
- `E_SteerCol = 200e9;   %Young's modulus           [Pa]`
- `v_SteerCol = 0.29;    %Poisson's ratio`
- `t_SteerCol = 0.002;   %Steering column thickness [m]`
- `Dy_SteerCol = 0.02;   %Dimension along y         [m]`
- `Dz_SteerCol = 0.02;   %Dimension along z         [m]`

The numerical weight check has been performed, having the result of the weighing operation made in laboratory.

FIGURE 4.48: STEERING COLUMN WEIGHING OPERATION.

Numerical simulation results by LUPOS, are shown in the following, listing all the firsts mode shapes with non-zero natural frequencies.

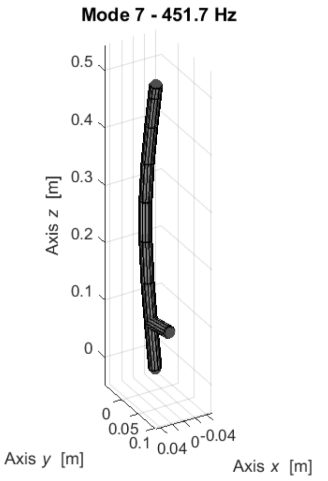

FIGURE 4.49: MODE 7 = 451.7 HZ

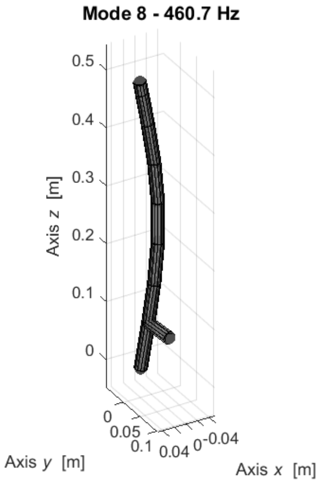

FIGURE 4.50: MODE 8 = 460.7 HZ

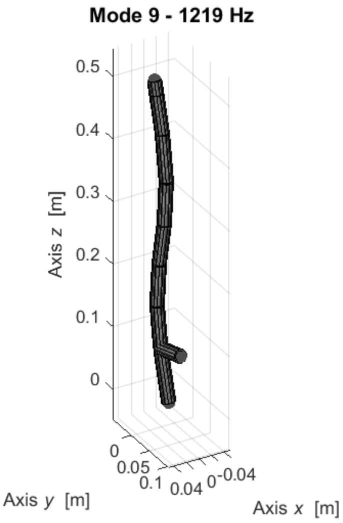

FIGURE 4.51: MODE 9 = 1219 HZ

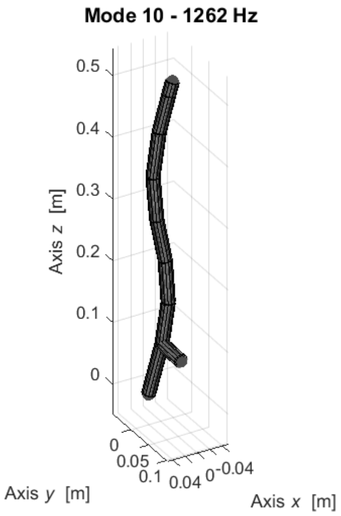

FIGURE 4.52: MODE 10 = 1262 HZ

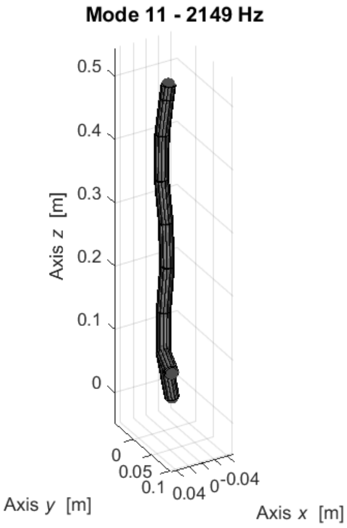

FIGURE 4.53: MODE 11 = 2149 HZ

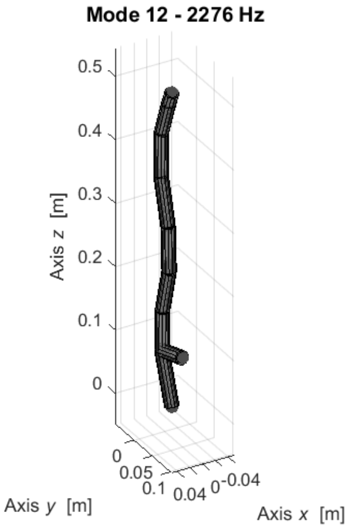

FIGURE 4.54: MODE 12 = 2276 HZ

Mode - Steering column	Frequency [Hz]	Mode Shape
Mode 1	451.7	1st Bending - YZ plane
Mode 2	460.7	1st Bending - XZ plane
Mode 3	1219	2nd Bending - YZ plane
Mode 4	1262	2nd Bending - XZ plane
Mode 5	2276	3rd Bending - XZ plane
Mode 6	2461	3rd Bending - YZ plane

TABLE 4.9: STEERIMG COLUMN NUMERICAL NATURAL FREQUENCIES.

4.3.3 Steering tie-rod

The steering tie-rod is the component whose function is to transfer the movement of the steering column to the stub-axles in order to perform the steering action (element **2** of the image **4.45**). Its geometry is quite essential, since it is a solid cylindrical beam, with hollow parts at the extremities for allowing the presence of the threads where are then screwed the joinballs.

FIGURE 4.55: ISOMETRIC VIEW OF THE STEERING COLUMN MADE BY OTK GROUP (LEFT SIDE) AND JOINBALL (RIGHT SIDE).

Positioning a node each 50mm, the nodes' split division has been carried out, with a total of 7 nodes over the length of the tie-rod (equal to 270mm). For the LUPOS model, the nodes have been distributed on the z-axis and, for emulating the accelerometer mass that will be added during the experimental modal analysis phase, a lumped mass of 10g has been introduced into the numerical model.

FIGURE 4.56: STEERING TIE-ROD WEIGHING OPERATION.

The presence of the concentrated mass into the numerical model is a direct consequence of the very low weight of the tie-rod (only 77.8g). So, it cannot be considered negligible a mass of 10g if corresponds to 13% of the overall weight of the component.

The elements used in the numerical environment to connect the nodes are again rod, with circular cross section.

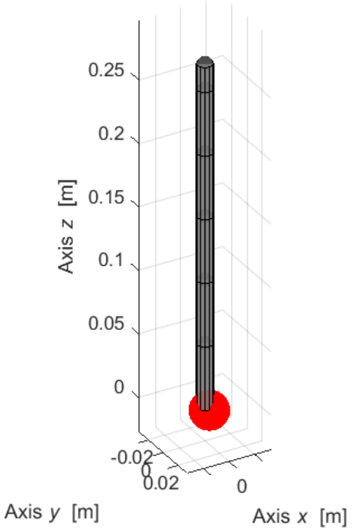

FIGURE 4.57: TRCP OUTPUT OF STEERING TIE-ROD NUMERICAL MODEL WITH LUMPED MASS IN THE OUTER DIAMETER AT COORDINATE $x = 0, y = 0.006\,m, z = 0$.

Regarding the material, it is used anodized aluminium. The main material properties and geometrical dimensions are reported here:

- `rho_TieRod = 2689.8;  %material density           [kg/m3]`
- `E_TieRod = 68.3e9;    %Young's modulus            [Pa]`
- `v_TieRod = 0.34;      %Poisson's ratio`
- `t_TieRod = -1;        %Tie-rod solid section`
- `Dy_TieRod = 0.012;    %Dimension along y          [m]`
- `Dz_TieRod = 0.012;    %Dimension along z          [m]`

The LUPOS numerical simulation results are listed below:

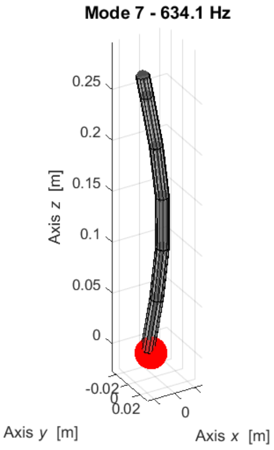

FIGURE 4.58: MODE 7 = 634.1 HZ

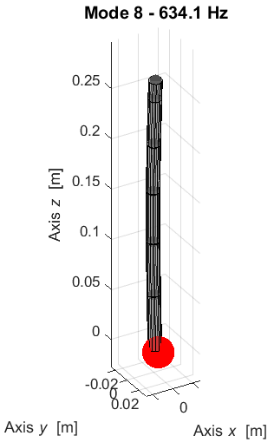

FIGURE 4.59: MODE 8 = 634.1 HZ

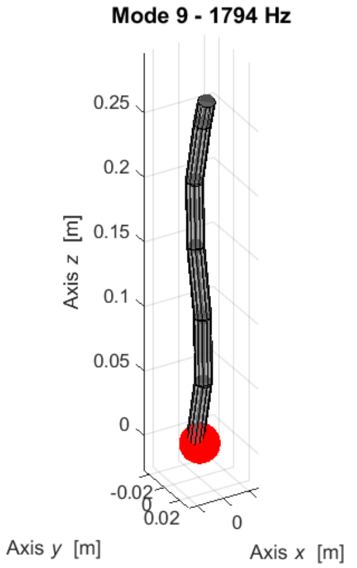

FIGURE 4.60: MODE 9 = 1794 HZ

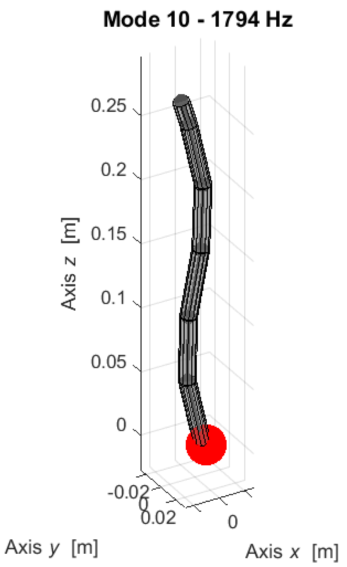

FIGURE 4.61: MODE 10 = 1794 HZ

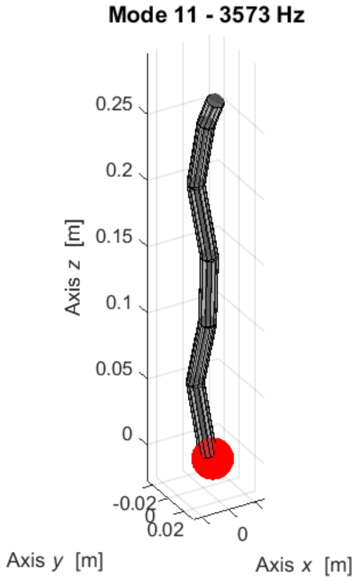

FIGURE 4.62: MODE 11 = 3573 HZ

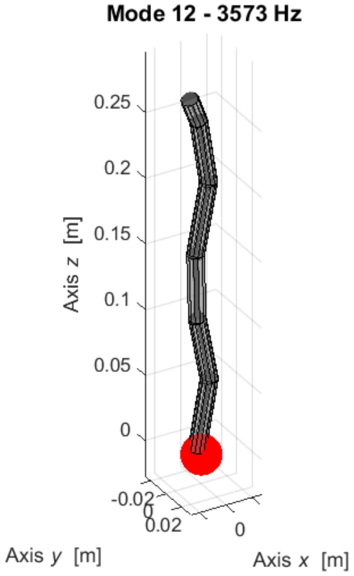

FIGURE 4.63: MODE 12 = 3573 HZ

Mode - Steering Tie-Rod	Frequency [Hz]	Mode Shape
Mode 1	634.1	1st Bending - YZ plane
Mode 2	634.1	1st Bending - XZ plane
Mode 3	1794	2nd Bending - XZ plane
Mode 4	1794	2nd Bending - YZ plane
Mode 5	3573	3rd Bending - YZ plane
Mode 6	3573	3rd Bending - XZ plane

TABLE 4.10: STEERING TIE-ROD NUMERICAL NATURAL FREQUENCIES.

4.3.4 Stub-axle

The third and last component of the steering system, is the stub-axle. It is put in movement by the tie-rod and, rotating around the stub-axle's screw, the front wheel consequently changes its direction.

FIGURE 4.64: ISOMETRIC VIEW OF THE STUB-AXLE MADE BY OTK GROUP.

In terms of geometry, it can be considered as made by 4 different components welded together: 4 rods with solid rounded cross section having different diameters and a beam with squared cross section. After the nodes division, which has given 13 main points, the TRCP output is the following:

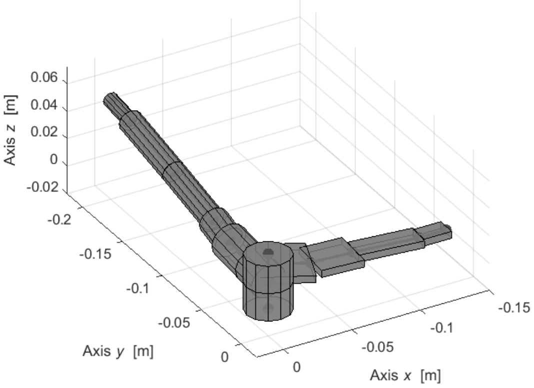

FIGURE 4.65: TRCP OUTPUT OF STUB AXLE NUMERICAL MODEL.

The weight is evaluated for the usual numerical-real weight comparison:

FIGURE 4.66: STUB-AXLE WEIGHING OPERATION.

The deployed material is a steel with more strength if compared with the one used for the steering column. For this reason, it has been hypothesized the using a particular kind of structural steel (different from the one of front ARB):

- `rho_SubAxle = 7850;  %material density          [kg/m3]`
- `E_SubAxle = 210e9;   %Young's modulus           [Pa]`
- `v_SubAxle = 0.3;     %Poisson's ratio`

Numerical modal analysis results:

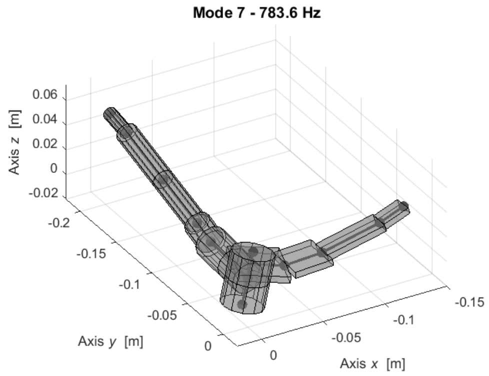

Figure 4.67: Mode 7 = 783.6 Hz

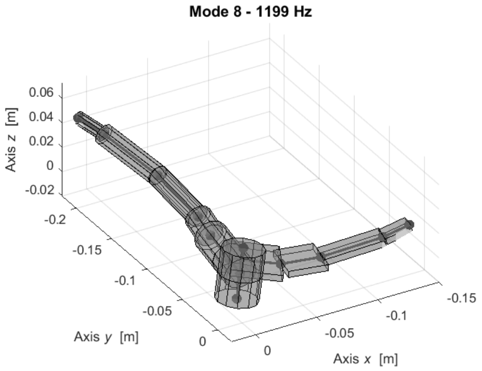

Figure 4.68: Mode 8 = 1199 Hz

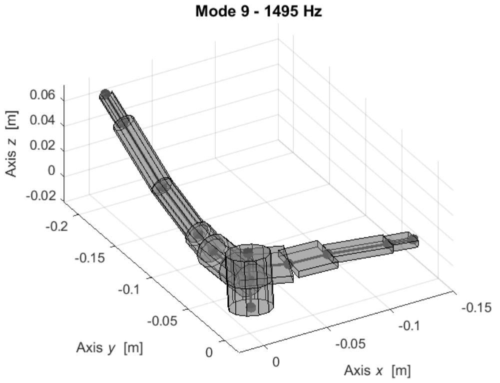

Figure 4.69: Mode 9 = 1495 Hz

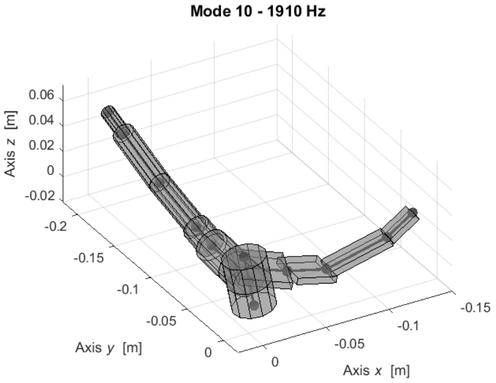

Figure 4.70: Mode 10 = 1910 Hz

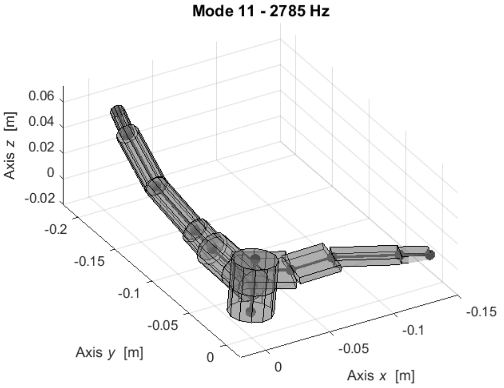

Figure 4.71: Mode 7 = 2785 Hz

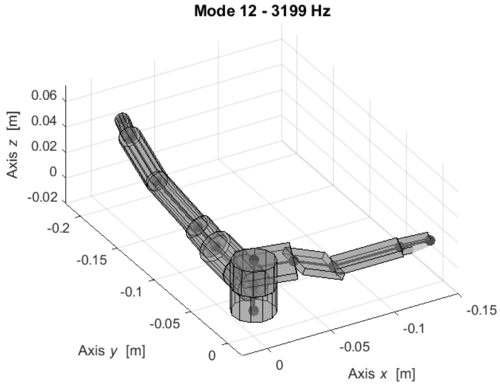

Figure 4.72: Mode 12 = 3199 Hz

Mode - Stub-axle	Frequency [Hz]	Mode Shape
Mode 1	783.6	1st Bending - XZ plane
Mode 2	1199	1st Bending - XY plane
Mode 3	1495	1st Bending - YZ plane
Mode 4	1910	2nd Bending - XZ plane
Mode 5	2785	2nd Bending - XY plane
Mode 6	3199	2nd Bending - YZ plane

TABLE 4. 11: STUB-AXLE NUMERICAL NATURAL FREQUENCIES.

4.3.5 Front lower bumper

The last component to be analysed for assessing modal behaviour and right material properties, is the Front lower bumper, which has even safety function. Side (left and right) bumper and front upper bumper are made with the same material and have similar shape of the one we are going to investigate, for this reason it is sufficient to just make the analysis on the front upper bumper for understanding how can behave the other safety components.

FIGURE 4.73: FRONT BUMPER SYSTEM (**1**: UPPER BUMPER, **2**: LOWER BUMPER) ON THE LEFT, ISOMETRIC VIEW OF THE FRONT LOWER BUMPER ON THE RIGHT.

It has been divided into 10 nodes, linked by means of hollow rod element with circular cross-section.

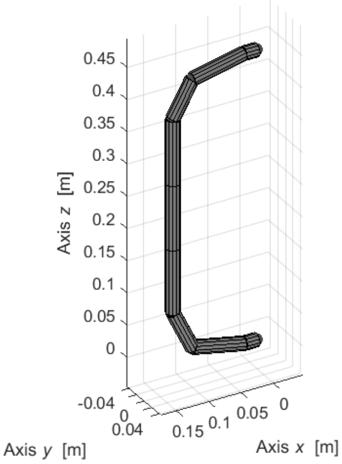

FIGURE 4.74 TRCP OUTPUT OF FRONT LOWER BUMPER NUMERICAL MODEL.

Weighing operation result:

FIGURE 4.75: FRONT LOWER BUMPER WEIGHING OPERATION.

The supposed material employed is the AISI 1018, the same of the steering column. Material properties and main dimensions are reported below:

- `rho_FrontLow_bump = 7850;   %material density         [kg/m3]`
- `E_FrontLow_bump = 200e9;    %Young's modulus          [Pa]`
- `v_FrontLow_bump = 0.29;     %Poisson's ratio`
- `t_FrontLow_bump = 0.0015;   %thickness`
- `Dy_FrontLow_bump = 0.02;    %Dimension along y        [m]`
- `Dz_FrontLow_bump = 0.02;    %Dimension along z        [m]`

Numerical modal analysis results:

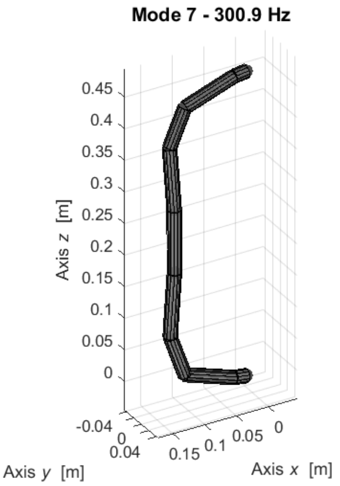

FIGURE 4.76: MODE 7 = 300.9 HZ

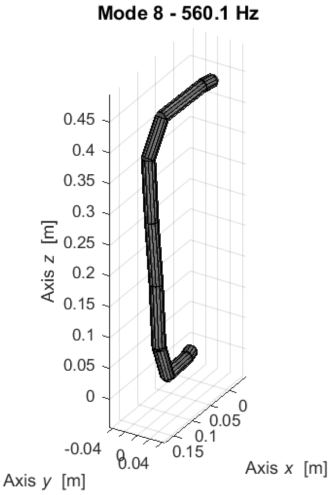

FIGURE 4.77: MODE 8 = 560.1 HZ

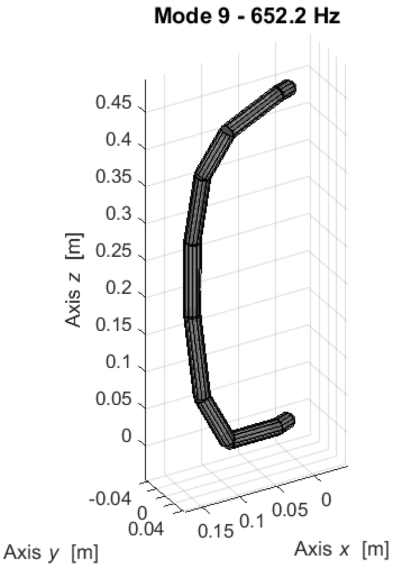

FIGURE 4.78: MODE 9 = 652.2 HZ

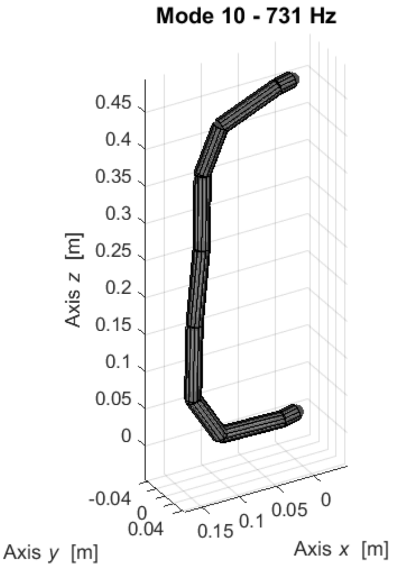

FIGURE 4.79: MODE 10 = 731 HZ

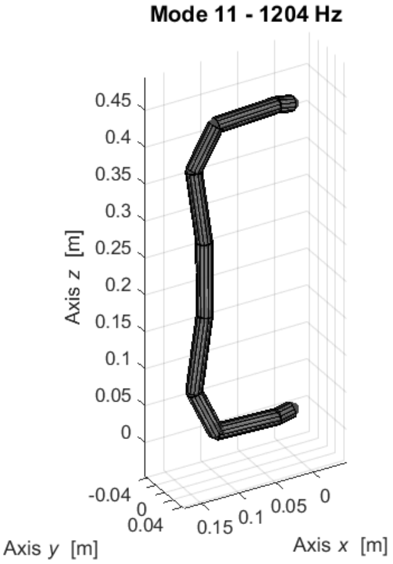

FIGURE 4.80: MODE 11 = 1204 HZ

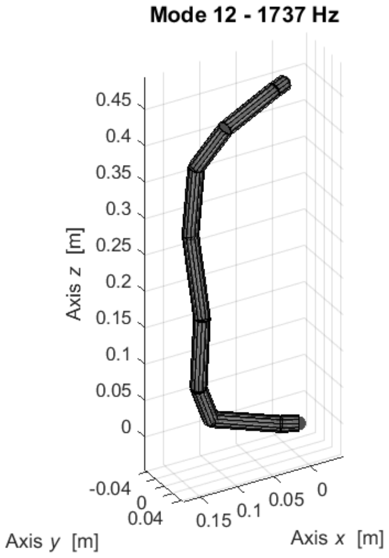

FIGURE 4.81: MODE 12 = 1737 HZ

Mode - Front lower bumper	Frequency [Hz]	Mode Shape
Mode 1	300.9	1st Bending
Mode 2	560.1	2nd Bending
Mode 3	652.2	3rd Bending
Mode 4	731	4th Bending
Mode 5	1204	5th Bending
Mode 6	1737	6th Bending

TABLE 4.12: FRONT LOWER BUMPER NUMERICAL NATURAL FREQUENCIES.

Chapter 5

5 EMA: Experimental Modal Analysis

The SINT Technology website, defines the Experimental Modal Analysis as an effective instrument for describing, understanding and modelling the dynamic behaviour of a structure. In this work, it has been carried out on all the components described in the previous chapter both to determine the real natural frequencies and mode shapes and to verify accuracy and calibrate the correspondent finite element model (FE). Experimental Modal Analysis (EMA) tests has been made in a controlled laboratory environment.

5.1 LMS SCADAS: hardware overview and experimental setup

The hardware that has been used for performing the experimental tests is LMS SCADAS, developed and produced by SIEMENS. LMS SCADAS systems offer test engineers versatile and scalable high-precision measurement tools that can be used to conduct productive measurements during all development stages of a product. This device is seamlessly integrated with dedicated and tailored software packages for accelerated measurement setup and correctly formatted results and analysis, such as LMS Test.Lab software on personal computers (PCs).

In this thesis work, vibration measurements are performed through impact test, with the aim of measuring the Frequency Response Function (FRF) on a test object using LMS Test.Lab Impact Testing. The FRF plays a key role in modal analysis, since provides insight about the dynamic behaviour of the system in terms of frequency and helps to identify vibration modes and their frequencies. Indeed, A Frequency Response Function is a frequency-based function used to identify resonant frequencies, damping and mode shapes of a physical structure. It is sometimes referred to a "transfer function" between the input and output, so expresses the frequency domain relationship between an input (x) and output (y) of a linear, time-invariant system.

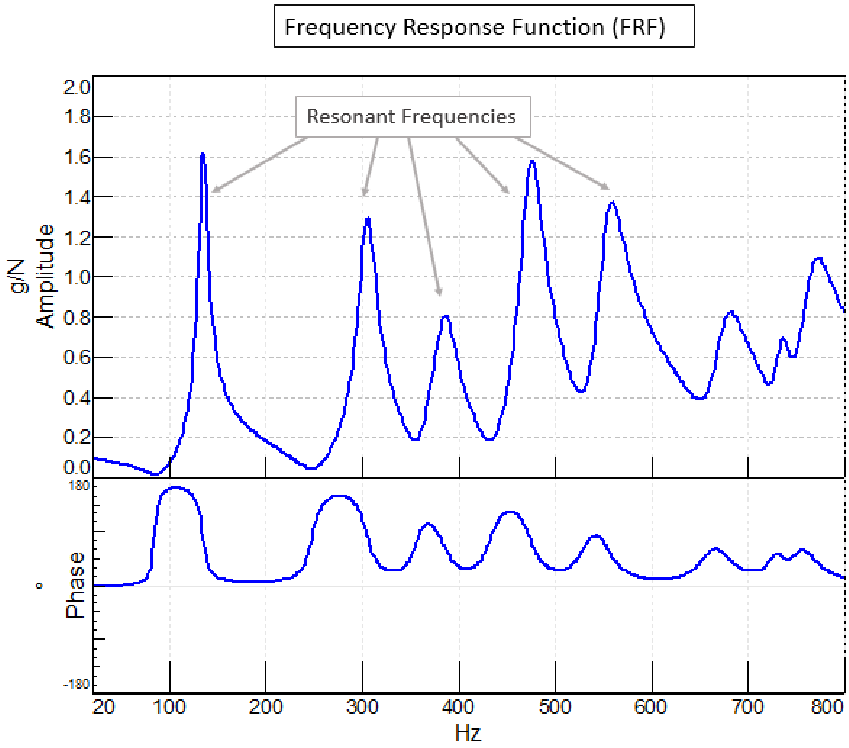

FIGURE 5.1: BODE PLOT OF AMPLITUDE AND PHASE OF A FRF FUNCTION.

Observing figure **5.1**, what can be said is that:

- Amplitude has peaks corresponding to natural frequencies/resonances of test object;
- Phase has shift at resonant frequency.

So, summing up all the information given up to now, the following can be learnt about a structure from the FRF:

- Resonances. Peaks indicate the presence of the natural frequencies of the structure under test;
- Damping. Damping is proportional to the width of the peaks. The wider the peak, the heavier the damping;
- Mode Shape. The amplitude and phase of multiple FRFs acquired to a common reference on a structure are used to determine the mode shape.

The equipment that has been used in laboratory for making possible the acquisition is listed below:

1. Simcenter SCADAS Mobile and SCADAS Recorder (formerly called LMS SCADAS);
2. Computer with Simcenter TestLab Impact Testing;
3. Impact instrumented hummer;

4. One or more accelerometers (depending on the test object) each with their own sensitivity;
5. Cables for input/output;
6. Ethernet cable for allowing connection between LMS SCADAS and PC;
7. Test object.

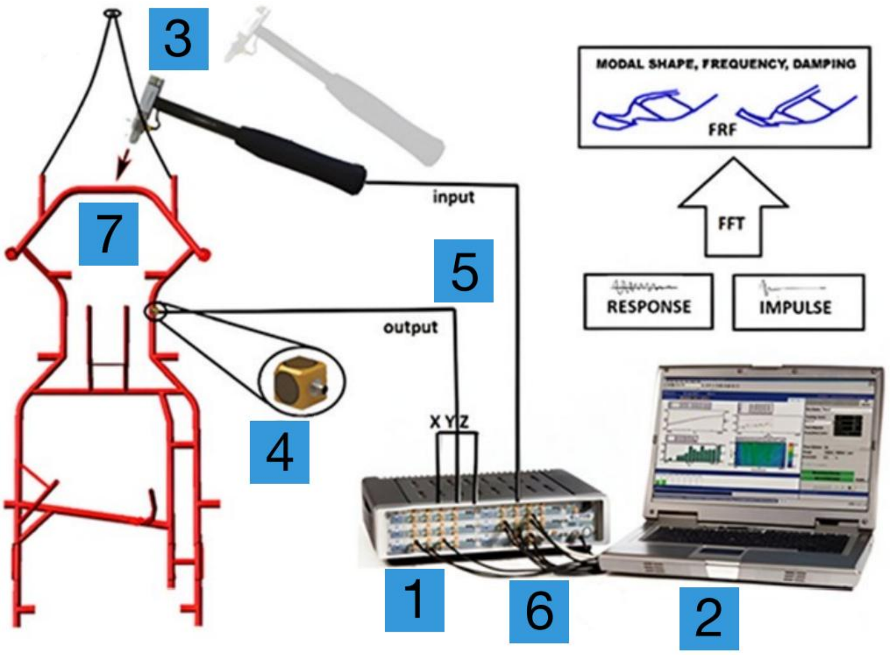

FIGURE 5.2: EXPERIMENTAL MODAL ANALYSIS SETUP.

Practically, when the instrumented hammer hits the test object, the input forces are sensed by the impedance head on the hammer and transmitted to the data acquisition system. Through the accelerometer(s), the response to the impulse on the examined frame structure has been measured. The experimental setup assumes free-free boundary conditions, enabling a “floating” state for the test object, thereby excluding external influences. This condition has been readily achieved in computer numerical modelling and replicated in physical modal tests using elastic rubber bands for hanging the test object, facilitating the identification of the first six rigid-body modes due to their low frequency.

5.2 EMA workflow: setup, measurement and postprocessing

The experimental modal analysis process is characterized by a certain workflow that is equivalent for any kind of component that must be investigated. For this reason, in this section will be deeply explained all the steps that are performed in laboratory when a test object needs to be experimentally evaluated. Obviously, some precautions must be taken into account into the operative phases as function of the object to be examined. Then, in the next sections regarding each kart vehicle components, only the results and peculiar passages performed will be shown.

In terms of making as clear as possible the description, the following flow chart has the aim of reporting the key steps to consider when the validation through experimental modal analysis needs to be carried out.

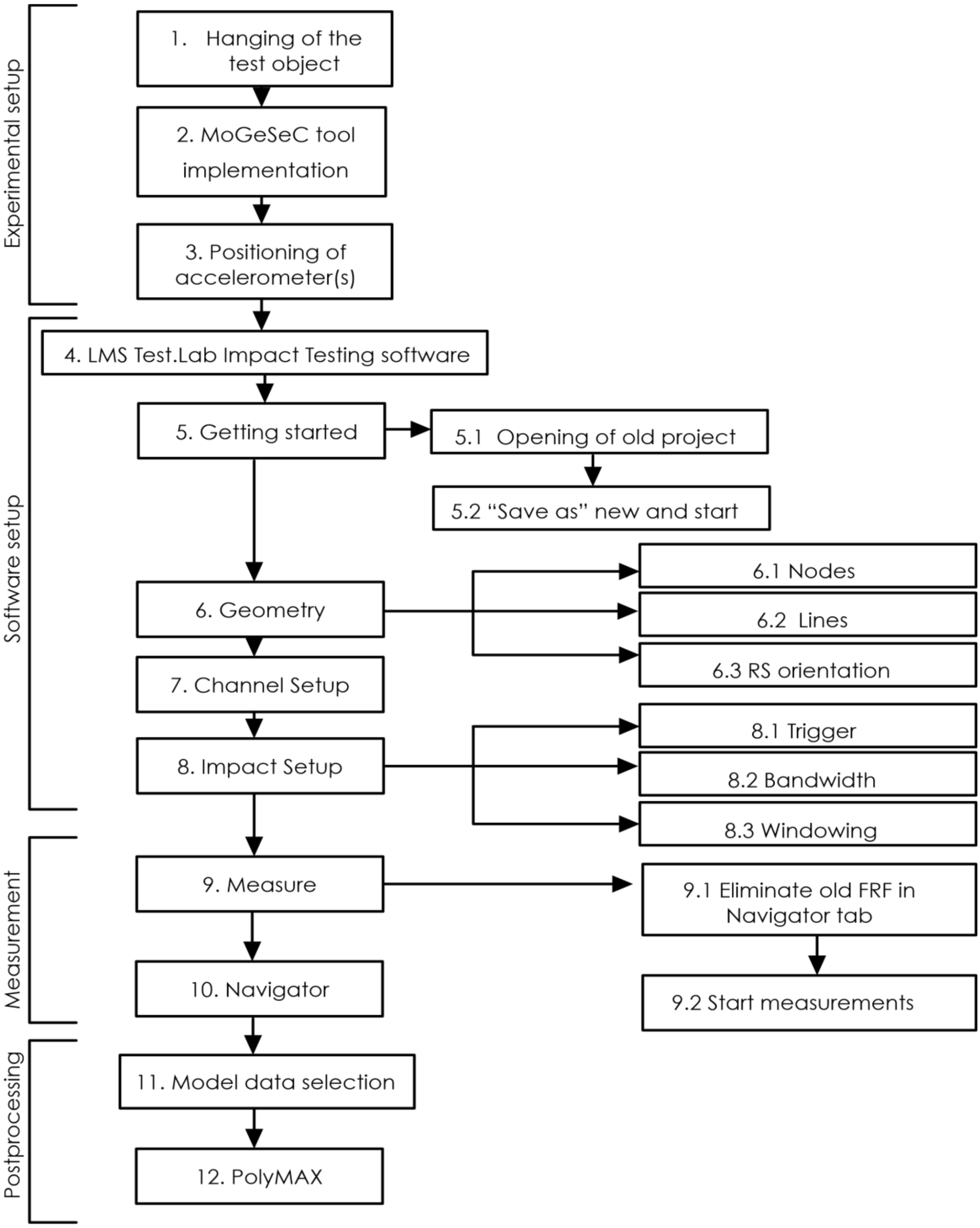

FIGURE 5.3: EMA FLOW CHART.

Experimental setup phase:

1. **Hanging of the test object.** Before starting the test, the item has to be positioned somewhere in order of making it ready for being hammered. Hence, an hydraulic crane has been employed for hanging the component under investigation with elastic rubber bands, since the experimental setup assumes free-free boundary conditions, enabling a "floating" state for the test object.

FIGURE 5.4: EXAMPLE OF TEST OBJECT (REAR AXLE IN THIS IMAGE) HANGED BY HYDRAULIC CRANE THROUGH ELASTIC RUBBER BANDS.

2. **MoGeSeC tool implementation**. In order to understand where the accelerometer(s) has to be positioned on the component to be tested, the MoGeSeC tool has been exploited. Indeed, a good data acquisition is based on the correct positioning of sensors on the structure. Modal and Geometrical Selection Criterion (MoGeSeC) is a FEM efficient tool, based on both geometry and modal properties of the system, obtained by a numerical modal analysis, for choosing the best representative nodes. The concept behind this technique is that the modal behaviour of a model can be represented by a list of nodes, whose eigenvectors resume the modal properties of the whole system. The progressive optimal location is based on both modal independence information and geometrical location to distribute accelerometers on the whole structure.
   Starting from a completed numerical simulation of the structure, it is needed to save the .geo file (from the "Model" struct) which contains all the node ID and coordinates and the simulation results from the

"Simul" struct (NodesPhi.dat, Phi.dat, W2.dat). These 4 files are given as input to MoGeSeC (graphical interface in image **5.5**) and, in the setting side, must be specified the type of accelerometers at disposal (triaxial, in our case) and the number of them (it depend on the complexity of the component).

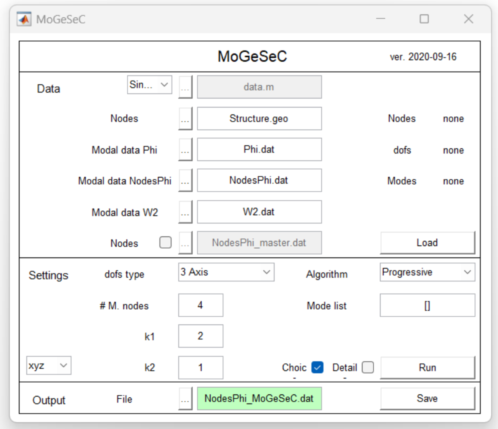

MoGeSeC ver. 2020-09-16

Data: Sin... data.m
Nodes: Structure.geo
Modal data Phi: Phi.dat
Modal data NodesPhi: NodesPhi.dat
Modal data W2: W2.dat
Nodes ☐ NodesPhi_master.dat
Nodes: none
dofs: none
Modes: none

Settings
dofs type: 3 Axis
M. nodes: 4
k1: 2
k2: 1
xyz
Algorithm: Progressive
Mode list: []
Choic ☑
Detail ☐

Output
File: NodesPhi_MoGeSeC.dat

FIGURE 5.5: MOGESEC GRAPHICAL INTERFACE.

An example of the MoGeSeC application is shown in the following image, where it is displayed the obtained result when applied for the seat selecting 3 accelerometers.

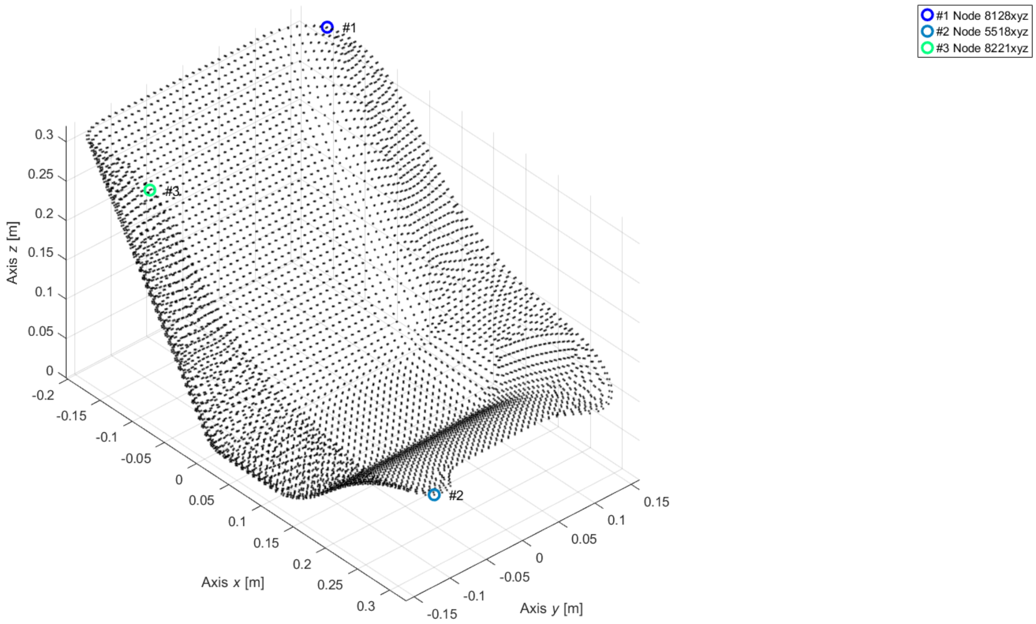

FIGURE 5.6: MOGESEC OUTPUT FOR SEAT.

3. **Positioning of accelerometer(s):** Once clear where to locate the accelerometers, the installation phase took place. In the picture below is reported the Greyhond after the installation of the accelerometers following the instruction given by MoGeSeC tool.

FIGURE 5.7: ACCELEROMETERS POSITIONED ON THE GREYHOUND SEAT.

Software setup phase:

4. **LMS Test.Lab Impact Testing software.** As previously defined, it is the software used in combination with LMS SCADAS for evaluating the FRF on a test object.
5. **Getting started.** Once connected the PC to the LMS SCADAS thorough ethernet cable, the icon Impact Testing in the Test.Lab Sructures Acquisition folder can be clicked.
   Then, it has been decided for each component, to start from an old project (5.1) which is opened and saved as a new one (5.2), with the name of the test object under investigation.
6. **Geometry.** Firstly, in the "Geometry" tab, the lines referred to the old project needs to be deleted. Then, leveraging the excel file generated for each kart vehicle component, the node ID and coordinates have been introduced into the sub-worksheet "Nodes" (6.1).
   Secondly, these nodes have been connected by means of lines (6.2) or surfaces (only in the case of seat and floor panel), for reproducing the structure of the component itself and so, giving to the software insights about the shape of the item.
   Finally, it is worth to be pointed out that Test.Lab introduces a local reference frame on each node, oriented as the global one. Hence, depending on the shape of the test object, those local reference frame have to be re-oriented (6.3) in such a way to "follow" the geometry of the component to be examined, since the software allows to rotate each reference frame about plane XY, XZ and YZ (a graphical demonstration will be given for each component in the next sections). It is very important because, the local reference frame of each node, indicates the 3 correct directions to be hammered in the measurement phase (8).

7. **Channel Setup.** The channel setup worksheet allows to define which channel of the LMS SCADAS must be activated: it depends on the number of the accelerometers positioned on the component to be tested. Being the inertial sensors at our disposal triaxial, 3 channels are associated per each transducer, one channel per each direction (x,y,x).
   Moreover, once specified the node ID where the sensor is located, depending on how the accelerometer is oriented after the installation on a certain node, the local inertial sensor direction must be re-oriented with respect to the direction of the local reference frame of the node.
   The last operation is to check if the accelerometer's sensitivity that appears on a certain channel, effectively corresponds to the real transducer sensitivity (which can be found on the calibration sheet).
8. **Impact setup.** Some parameters are defined into this section:
   - Trigger level (8.1), that will make the measurement start automatically when the impact hammer strikes the object.
   - Bandwidth (8.2), which is the input spectrum of the impact hammer. To get a good Frequency Response Function (FRF) measurement, the impact hammer force should be uniform, or the same level, across the desired frequency range.
   - In the "Windowing" sub-worksheet (8.3), Using a sample acquired measurement, a suitable window will be determined to assure that the measurement is not affected by leakage. Otherwise, it is possible to set by hand 2 of the 3 parameters present: Bandwidth, Spectral line and Acquisition time. Indeed, being the $Spectral\ lines = Acquisition\ time * Bandwidth$, defined 2 of them, the third will consequently change.

Measurement phase:

9. **Measure.** With setup finished, the actual FRF measurement can be performed in the 'Measure' worksheet. Before doing this, the old FRF must be deleted into the "Navigator" tab (9.1).

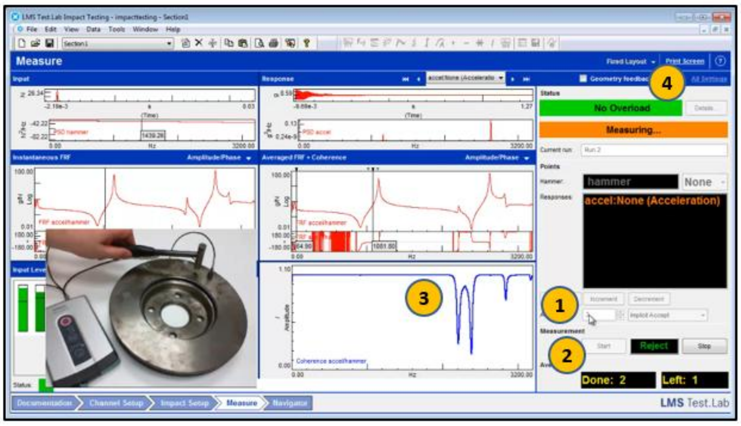

FIGURE 5.8: "MEASURE" WORKSHEET.

Here, has to be defined the node to be hammered and the direction of the hummer hit. Then for performing the measurement, the 4 steps indicated into the figure **5.7** need to be made:

1. Set the number of averages desired;
2. Press the 'Start' button and hit the test object (9.2);
3. Monitor the FRF and coherence after each hit. Measurement must manually be accepted by user. If an undesirable measurement occurs, the component is hit again.

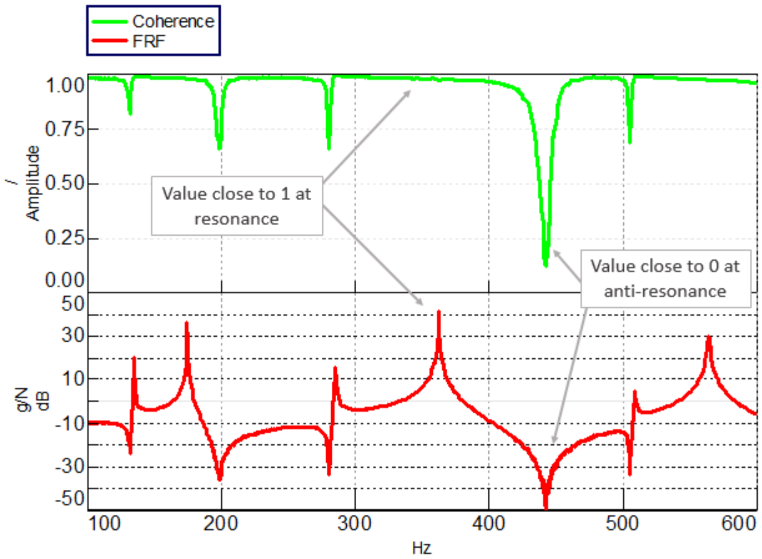

FIGURE 5.9: COHERENCE (TOP DISPLAY) SHOULD BE CLOSE TO 1, WITH THE ONLY EXCEPTIONS OCCURRING AT ANTI-RESONANCES IN THE FRF (BOTTOM DISPLAY)

4. Optional. Under 'All settings', it can be turned on double hit and overload detection/rejection if desired.

10. **Navigator**. Where all the FRF are present, so it is possible to manage them, eliminating and making again some measurements if errors are made.

Postprocessing:

11. **Model Data Selection.** In this worksheet, it can be found:
    - $References = (n° \ of \ nodes) * (n° \ of \ hammered \ direction)$
    - $Responses = (n° \ of \ transducers) * (n° \ of \ transducer \ direction)$

    Since the References are always higher than the Responses, for avoiding the malfunctioning of the identification system, the "Switch" button is pressed, which create the reciprocate of the FRF.
12. **PolyMAX:** Firstly, into the "Stabilization" sub-worksheet, has to be decided the frequency range where the searching for the mode shapes must take place. Then, the Model size must be chosen.

    After having pressed 'play', the identification can be manually carried out, selecting only the stable poles in terms of mode, frequency and damping.

Finaly, in the “Shapes” sub-worksheet, it can be specified if is required a real or a complex modal analysis and, once finished the calculation, the selected mode shapes can be seen.

In the next sections, the attention will switch more on the experimental modal analysis results, showing per each component just what follows:

- MoGeSeC’s output;
- Hanged test object with accelerometers installed;
- Test.Lab model nodes local reference system “re-oriented” (when re-orientation is required) or “orientation” (when the standard orientation has not been modified);
- EMA’s results.

5.3 Main components

The experimental modal analysis of the 4 main components, is going to be displayed.

5.3.1 Chassis

- MoGeSeC’s output:

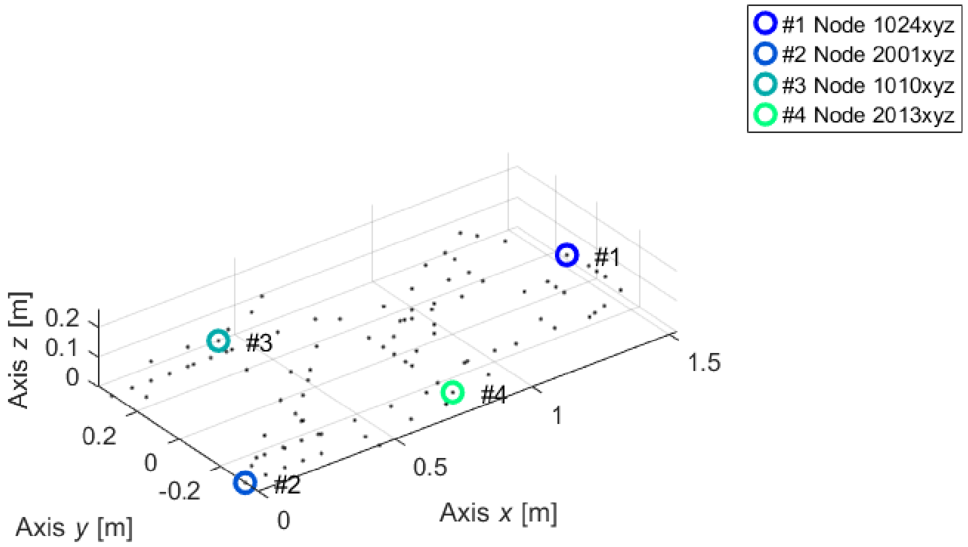

Figure 5.10: Chassis MoGeSeC’s output.

The accelerometers have been positioned in the following nodes:

1. 1024;
2. 2001;
3. 1010;
4. 2011.

Even though the suggestion given by MoGeSeC regards the positioning on the node 2013, it has been chosen to put in a different position (but very close to the recommended one) for technical issues during installation.

Figure 5.11: Accelerometer 1

Figure 5.12: Accelerometer 2

Figure 5.13: Accelerometer 3

Figure 5.14: Accelerometer 4

- Hanged chassis with accelerometers installed:

Figure 5.15: Hanged chassis with accelerometers installed on nodes 1024, 2001, 1010, 2011.

- Test.Lab model nodes local reference system re-oriented: Chassis. In terms of re-orienting each node in such a way that the local reference frame could “follow” the shape of the chassis, the rotation angle(s) about XY, XZ or YZ plane has been taken from the 3D CAD model of the tested object and introduced into the sub-worksheet “Nodes” of the Test-Lab software, besides the coordinates x,y,z.

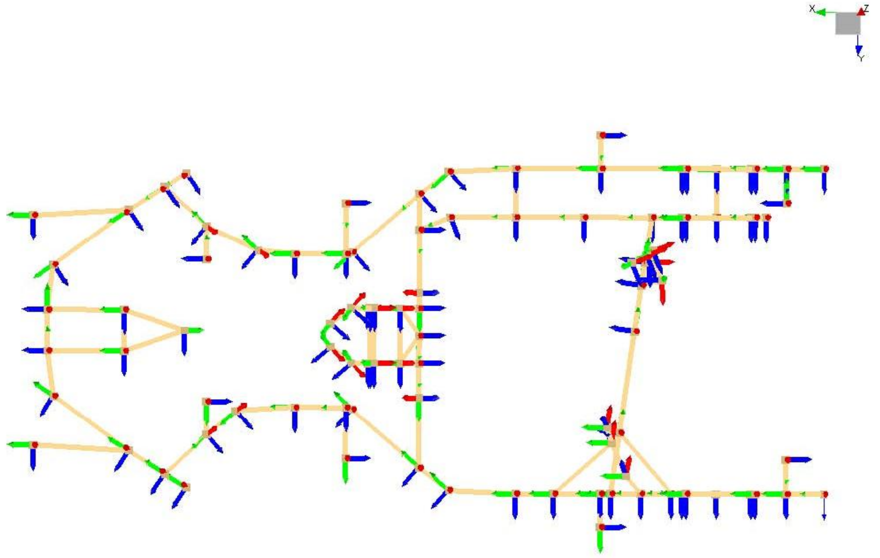

FIGURE 5.16: NODES LOCAL REFERENCE SYSTEM RE-ORIENTED: CHASSIS.

Each node has been connected to the other by means of “lines”.

- Chassis EMA’s results:

Mode - Chassis	Frequency [Hz]	Mode Shape
Mode 1	42.6	1st Bending
Mode 2	43.5	1st Torsion
Mode 3	64.85	2nd Bending
Mode 4	83.93	2nd Torsion
Mode 5	88.49	3rd Torsion
Mode 6	102.4	3rd Bending

TABLE 5.1: CHASSIS EMA’S RESULTS.

5.3.2 Front ARB

- MoGeSeC’s output: For a simple component like the Front ARB and Rear axle, it is not necessary to exploit the FEM tool MoGeSeC. Indeed, in order to understand where to install the accelerometers, it is sufficient to analyse the mode shapes of a numerical simulation previously performed for spotting the fixed nodes: these can be considered as a potential transducer assemble points.

  At the end of the pre-described investigation, the accelerometers have been positioned in the following nodes:

1. 2;
2. 6;
3. 8.

- Hanged Front ARB with accelerometers installed:

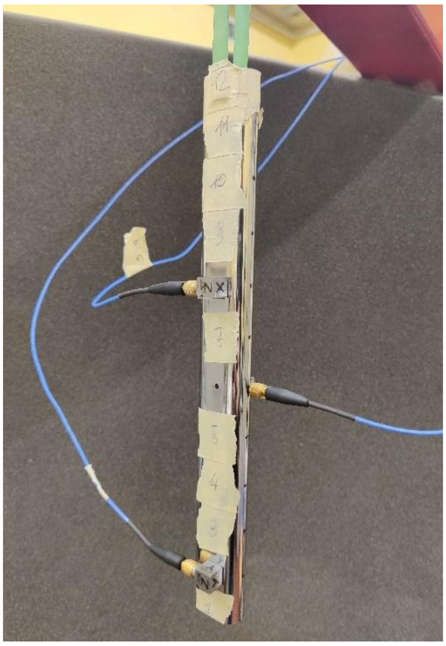

FIGURE 5.17: HANGED FRONT ARB WITH ACCELEROMETERS INSTALLED ON NODES 2, 6, 8.

- Test.Lab model nodes local reference system orientation: Front ARB.

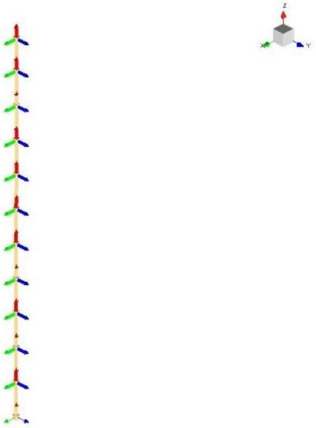

FIGURE 5.18: NODES LOCAL REFERENCE SYSTEM ORIENTATION: FRONT ARB.

- Front ARB EMA's results:

Mode - Front ARB	Frequency [Hz]	Mode Shape
Mode 1	1260	1st Bending - XZ plane
Mode 2	2084	1st Bending - YZ plane
Mode 3	3365	2nd Bending - XZ plane

TABLE 5.2: FRONT ARB EMA'S RESULTS.

5.3.3 Seat: Standard and Greyhound

- MoGeSeC's output: for both seats, the MoGeSeC's output is only one since the only CAD model present is the one referred to the standard seat. There is a difference in the size of the two components, since the Greyhound one has the same shape but with scaled dimensions over the x and y axis for getting a bigger seat (it is just for fitting well the requirements of some drivers with larger body).
  It has been used a different size seat because Greyhound factory had available, at that time, the bigger seat to be sent to us.

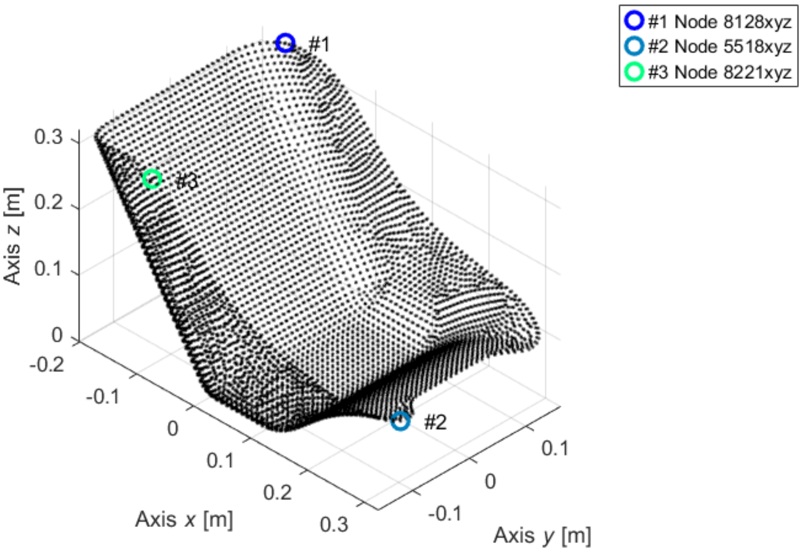

FIGURE 5.19: SEAT MOGESEC'S OUTPUT.

As shown in the previous illustration (**5.19**), the FEM tool MoGeSeC has been applied to the numerical model made by 8426 nodes (connected through hexahedral elements). For performing the Experimental Modal Analysis, it has been necessary to reduce as much as possible the nodes number. Thereby, starting from the 3D CAD model, 58 nodes has been selected and the x,y,z coordinates have been saved into an excel file.

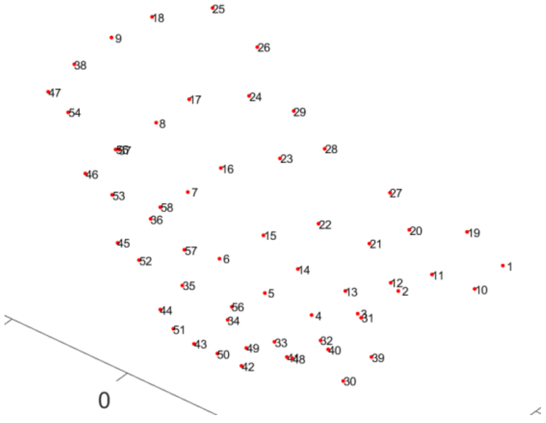

FIGURE 5.20: RESULT OF THE SEAT NODES SPLIT (TOTAL OF 58) REPORTED ON MATLAB.

Since the shape of the two seats is completely equal, the x and y coordinates of the standard seat have been scaled of a factor 0.04 for reproducing the correct dimensions of the Greyhound seat.

As it is possible to see from picture **5.19**, MoGeSeC's output suggests positioning the transducers on the nodes: 8128, 5518, 8221. So, after having carried out a detailed comparison between the experimental nodes split division (58 points) and the numerical one (8426 nodes), it has been assumed that the accelerometers could be positioned on nodes:

1. 25;
2. 30;
3. 55.

- Standard seat with accelerometers installed and experimental nodes split division:

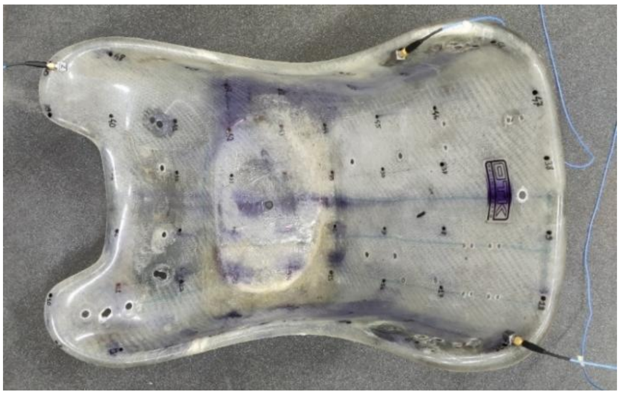

FIGURE 5.21: STANDARD SEAT WITH ACCELEROMETERS INSTALLED ON NODES 25, 30, 55.

- Hanged Greyhound seat with accelerometers installed and experimental nodes split division:

FIGURE 5.22: HANGED GREYHOUND WITH ACCELEROMETERS INSTALLED.

- Test.Lab model nodes local reference system re-oriented: Seat. Whether for the other components the 3D CAD model has given the insights for rotating the reference system, in this case (and for the floor panel as well), a dedicated MatLab script has been generated with the aim of assessing the normal vector to each node and the correspondent made rotation about x-axis and y-axis (the last one about y-axis must be set as negative value into the software due to the way in which Test.Lab makes the rotation of each local node reference system with respect to the global reference system).

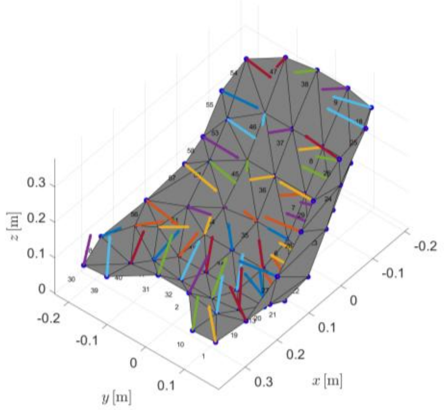

FIGURE 5.23: MATLAB SCRIPT NORMALS' EVALUATION OUTPUT.

Once defined all the rotation into the software, seat into the Test-Lab enviroment appears as below:

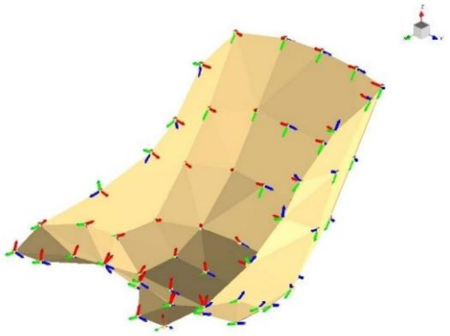

FIGURE 5.24: NODES LOCAL REFERENCE SYSTEM RE-ORIENTED: SEAT.

Nodes connection, in seat and floor panel case, has been made through "surfaces".

- Seat standard EMA's results:

Mode - Seat std	Frequency [Hz]	Mode Shape
Mode 1	30.69	1st Torsion
Mode 2	99.7	1st Bending
Mode 3	137.3	2nd Bending
Mode 4	150.7	3rd Bending
Mode 5	193	2nd Torsion
Mode 6	214	4th Bending

TABLE 5.3: SEAT STANDARD EMA'S RESULTS.

- Seat Greyhound EMA's results:

Mode - Greyhound	Frequency [Hz]	Mode Shape
Mode 1	19.73	1st Torsion
Mode 2	57.87	1st Bending
Mode 3	86.52	2nd Bending
Mode 4	94.09	2nd torsion
Mode 5	112.4	3rd Bending

TABLE 5.4: SEAT GREYHOUND EMA'S RESULTS.

5.3.4 Rear axle

- MoGeSeC's output: as previously announced in the section **5.3.2**, observing and analysing the numerical simulations result of the rear axle, it is possible to define the fixed nodes, which can potentially host the transducers. The selected nodes are:
    1. 1;
    2. 7;
    3. 15.

- Hanged Rear axle with accelerometers installed:

FIGURE 5.25: HANGED FRONT ARB WITH ACCELEROMETERS INSTALLED ON NODES 1, 7, 15.

- Test.Lab model nodes local reference system orientation: Rear axle.

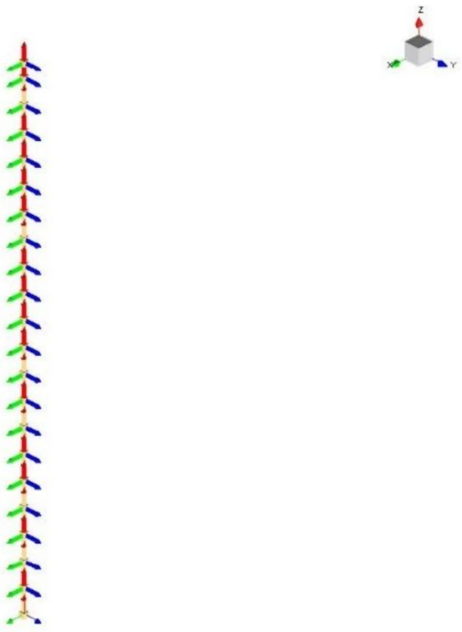

FIGURE 5.26: NODES LOCAL REFERENCE SYSTEM ORIENTATION: REAR AXLE.

- Rear axle EMA's results:

Mode - Rear axle	Frequency [Hz]	Mode Shape
Mode 1	285.7	1st Bending - 1st plane
Mode 2	286.2	1st Bending - 2nd plane
Mode 3	760.7	2nd Bending - 1st plane
Mode 4	768.1	2nd Bending - 2nd plane
Mode 5	1439	3rd Bending - 1st plane
Mode 6	1452	3rd Bending - 2nd plane

TABLE 5.5: REAR AXLE EMA'S RESULTS.

5.4 Secondary components

In this section the 5 secondary components already described into the chapter **4**, will be experimentally analysed.

5.4.1 Floor panel

- MoGeSeC's output: the floor panel is a thin-walled component which has been numerically modelled in the same way of the seat. For this reason, the FEM tool MoGeSeC has been applied to a numerical model composed by 4934 nodes, linked together with "Hexa" elements.

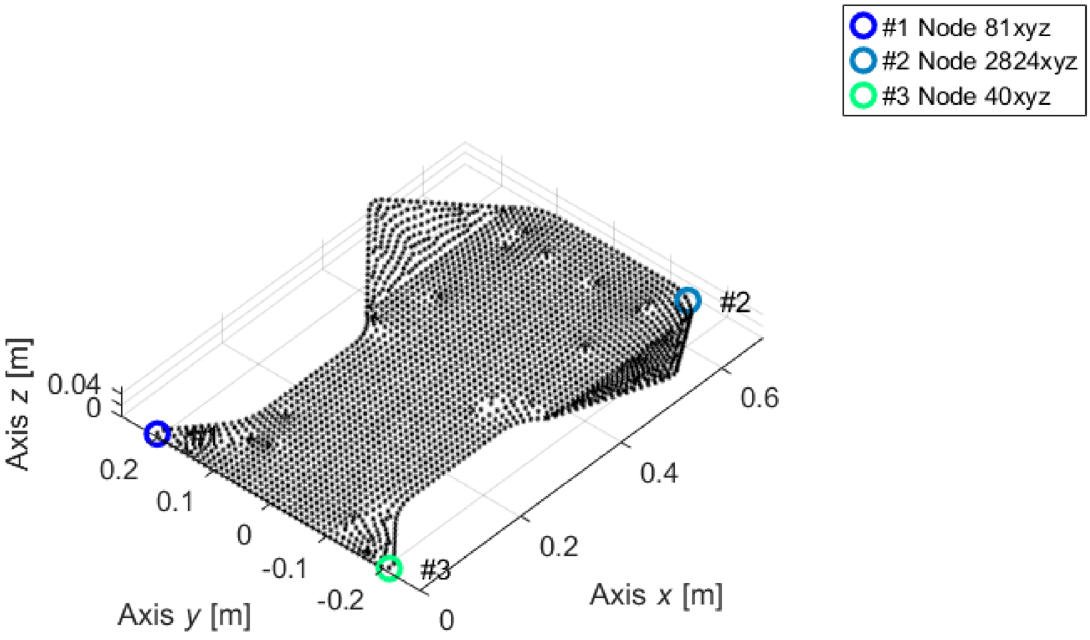

FIGURE 5.27: FLOOR PANEL MOGESEC'S OUTPUT.

Starting from the 3D CAD model, only 24 nodes have been selected as important to be hammered and the correspondent x,y,z coordinates have been saved into a new excel file.

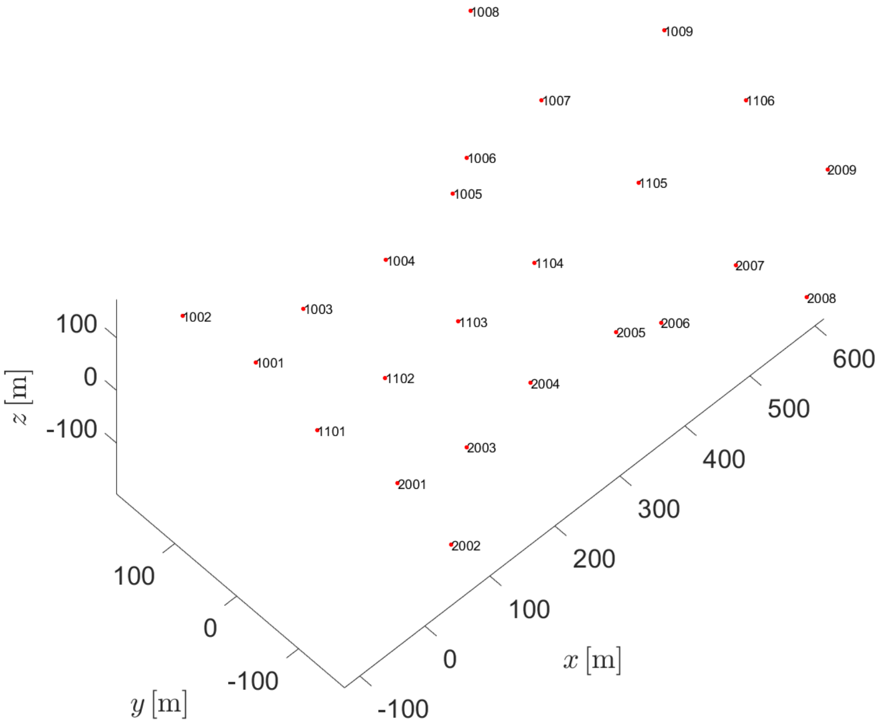

FIGURE 5.28: RESULT OF THE FLOOR PANEL NODES SPLIT (TOTAL OF 24) REPORTED ON MATLAB.

Comparing the two previous illustrations (**5.27** and **5.28**), it is quite easy to understand that the experimental nodes much closer to the suggested ones by MoGeSeC (81, 2824 and 40) are the following:

1. 1002;
2. 2009;
3. 2002.

- Floor panel with accelerometers installed and experimental nodes split division:

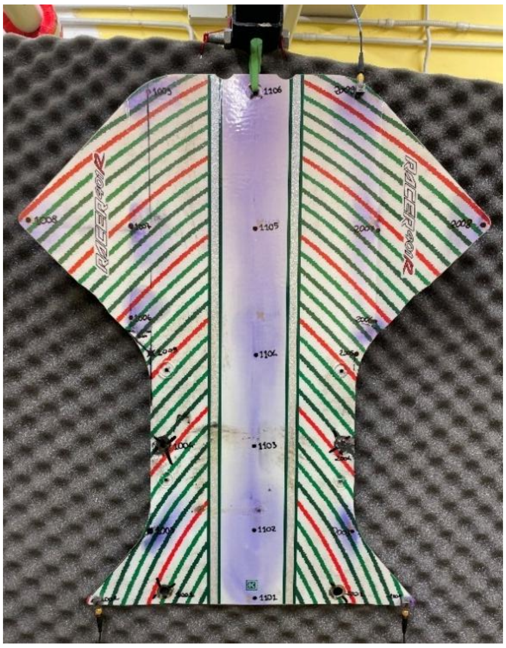

FIGURE 5.29: FLOOR PANEL WITH ACCELEROMETERS INSTALLED ON NODES 1002, 2009, 2002.

- Test.Lab model nodes local reference system re-oriented: Floor panel.

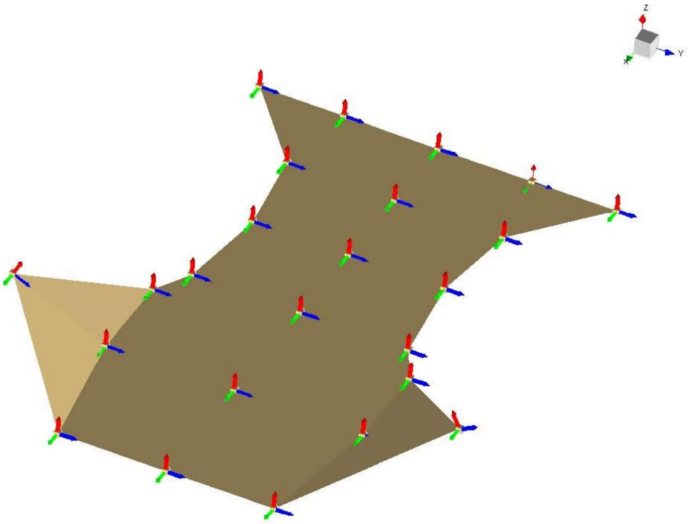

FIGURE 5.30: NODES LOCAL REFERENCE SYSTEM RE-ORIENTED: FLOOR PANEL.

- Floor panel EMA's results:

Mode - Floor panel	Frequency [Hz]	Mode Shape
Mode 1	15.51	1st Torsion
Mode 2	16.8	1st Bending
Mode 3	44.44	2nd Torsion
Mode 4	48.81	2nd Bendig
Mode 5	73.96	3rd Torsion
Mode 6	90.2	3rd Bending

TABLE 5.6: FLOOR PANEL EMA'S RESULTS.

5.4.2 Steering column

- MoGeSeC's output:

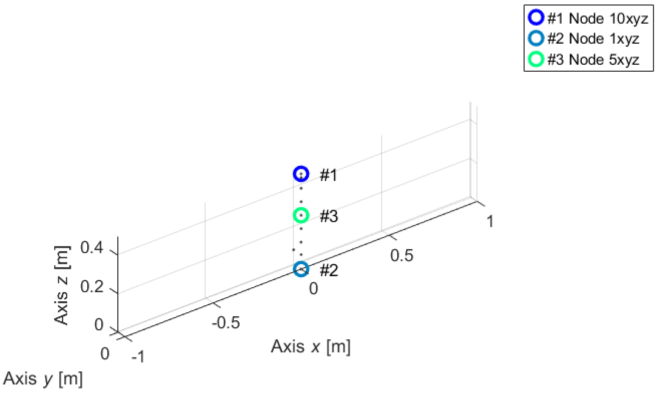

FIGURE 5.31: STEERING COLUMN MOGESEC'S OUTPUT.

So, the potentially transducers location could be the following: 10, 1, 5.

- Hanged steering column with accelerometers installed:

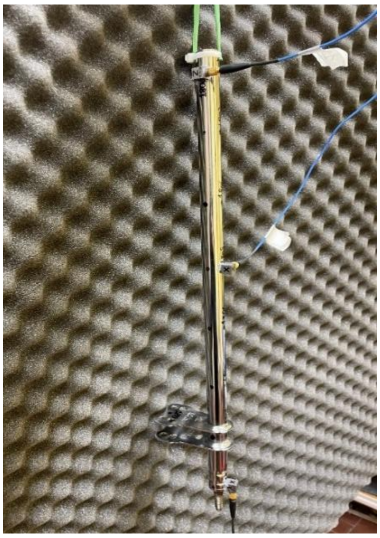

FIGURE 5.32: STEERING COLUMN WITH ACCELEROMETERS INSTALLED ON NODES 10, 1, 5.

- Test.Lab model nodes local reference system orientation: Steering column.

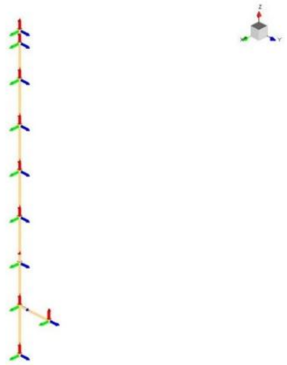

FIGURE 5.33: NODES LOCAL REFERENCE SYSTEM ORIENTATION: REAR AXLE.

- Steering column EMA's results:

Mode - Steering column	Frequency [Hz]	Mode Shape
Mode 1	376.9	1st Bending - YZ plane
Mode 2	394.7	1st Bending - XZ plane
Mode 3	1082	2nd Bending - YZ plane
Mode 4	1096	2nd Bending - XZ plane
Mode 5	1994	3rd Bending - XZ plane

TABLE 5.7: STEERING COLUMN EMA'S RESULTS.

5.4.3 Steering Tie-Rod

- MoGeSeC's output:

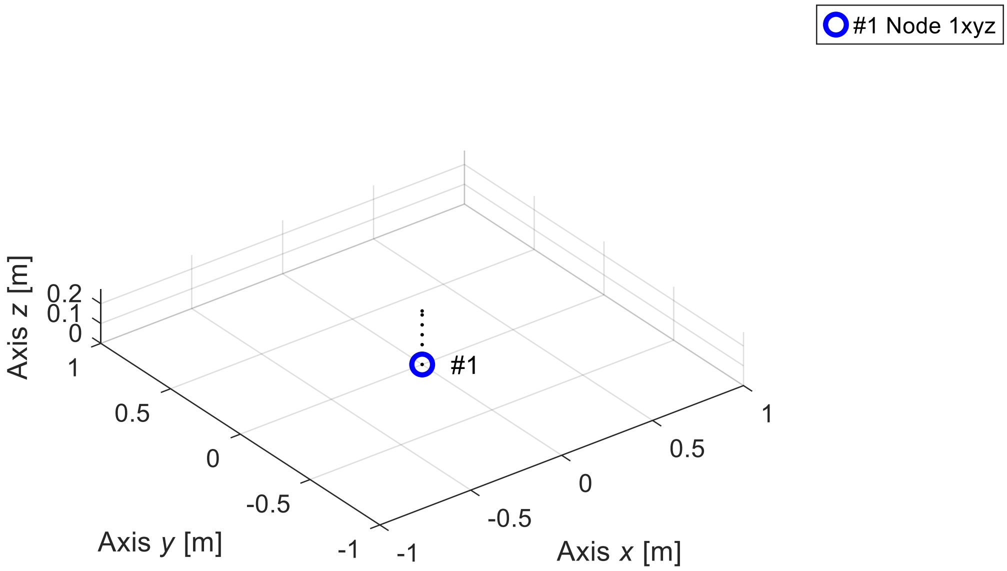

FIGURE 5.34: STEERING TIE-ROD MOGESEC'S OUTPUT.

The choice of using just one accelerometer (to be positioned into the node 1) is related to the weight of this component is very low, 77.8g. So, since each transducer weight is 10g (which corresponds to 13% of the overall weight of the component), adding more than one inertial sensor would impact too much the natural response of the tie-rod.

- Hanged steering column with accelerometers installed:

FIGURE 5.35: STEERING TIE-ROD WITH ACCELEROMETERS INSTALLED ON NODE 1.

- Test.Lab model nodes local reference system orientation: Steering tie-rod.

FIGURE 5.36: NODES LOCAL REFERENCE SYSTEM ORIENTATION: STEERING TIE-ROD.

- Steering column EMA's results:

Modes - tierod	Frequency [Hz]	Mode Shape

Mode 1	652.9	1st Bending - YZ plane
Mode 2	752.7	1st Bending - XZ plane
Mode 3	1949	2nd Bending - YZ plane
Mode 4	2290	2nd Bending - XZ plane
Mode 5	3250	3rd Bending - YZ plane
Mode 6	3909	3rd Bending - XZ plane

TABLE 5.8: STEERING TIE-ROD EMA'S RESULTS.

The fact that the experimental natural frequencies are not equal in pair as obtained into the numerical simulation, is due to the missing of "symmetry" property regarding the position of the CoG due to the presence of lumped mass of the accelerometer, which affect the modal behaviour.

5.4.4 Stub-axle

- MoGeSeC's output:

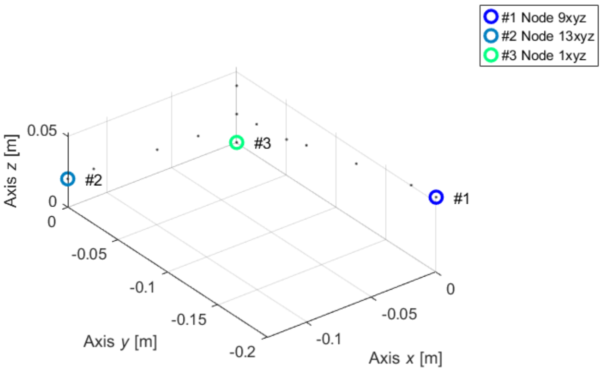

FIGURE 5.37: STUB-AXLE MOGESEC'S OUTPUT.

Hence, the accelerometers can be located on nodes: 9, 13, 1.

- Hanged steering column with accelerometers installed:

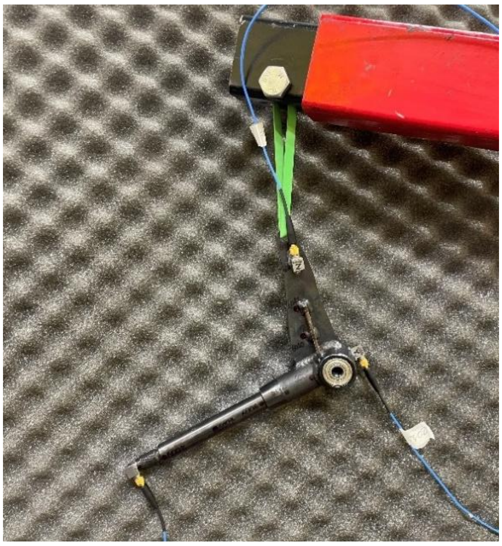

FIGURE 5.38: STUB-AXLE WITH ACCELEROMETERS INSTALLED ON NODES 9, 13, 1.

- Test.Lab model nodes local reference system re-oriented: Stub-axle.

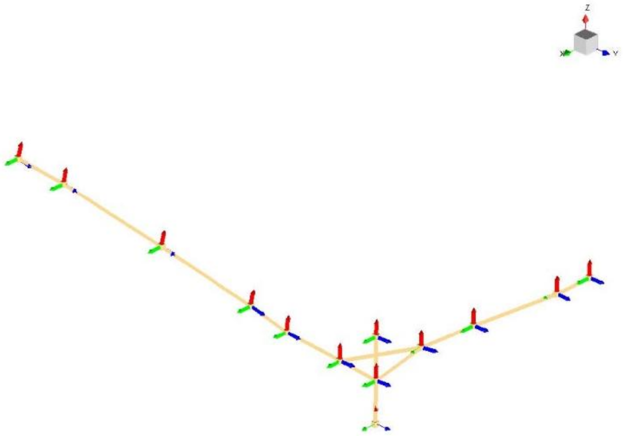

FIGURE 5.39: NODES LOCAL REFERENCE SYSTEM RE-ORIENTED: STUB-AXLE.

- Stub-axle EMA's results:

Mode - Stub-axle	Frequency [Hz]	Mode Shape
Mode 1	724.6	1st Bending - XZ plane
Mode 2	1073	1st Bending - XY plane
Mode 3	1482	1st Bending - YZ plane
Mode 4	2338	2nd Bending - XY plane
Mode 5	2726	2nd Bending - XZ plane
Mode 6	3417	2nd Bending - YZ plane

TABLE 5. 9: STUB-AXLE EMA'S RESULTS.

5.4.5 Front lower bumper

- MoGeSeC's output:

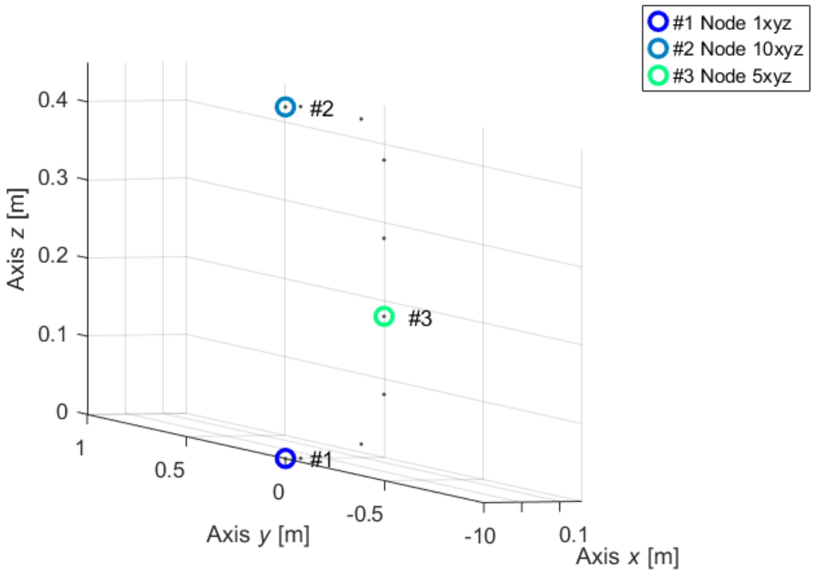

FIGURE 5.40: FRONT LOWER BUMPER MOGESEC'S OUTPUT.

The accelerometers have been positioned in the following nodes: 1, 10, 5.

- Hanged Front lower bumper with accelerometers installed:

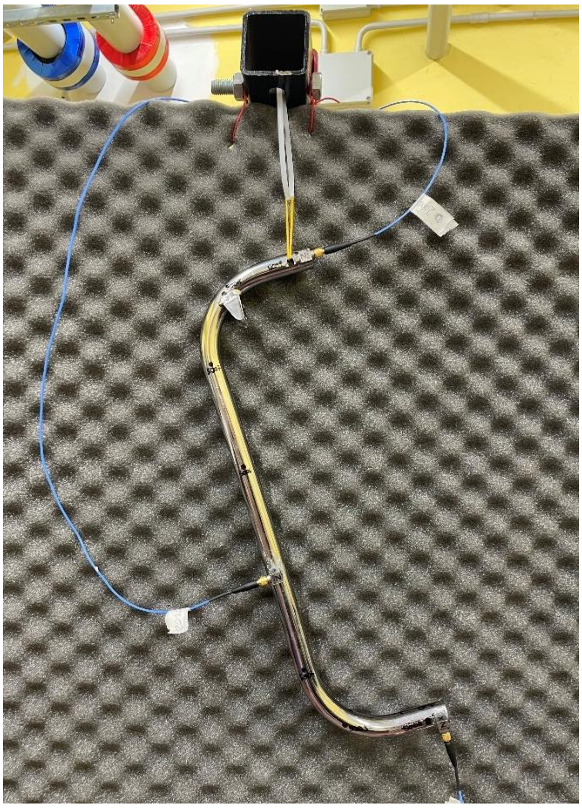

FIGURE 5.41: STUB-AXLE WITH ACCELEROMETERS INSTALLED ON NODES 1, 10, 5.

- Test.Lab model nodes local reference system re-oriented: Front lower bumper.

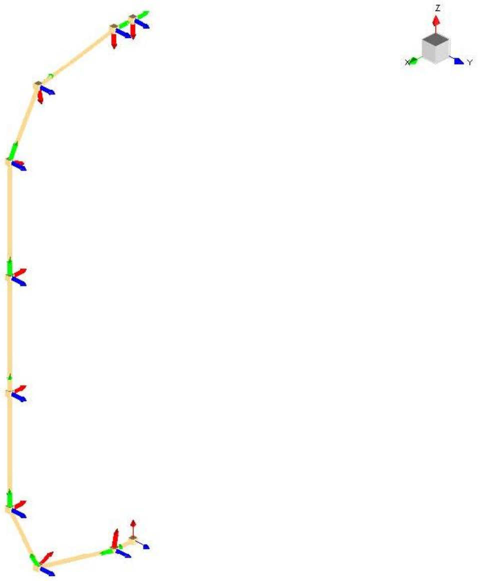

FIGURE 5.42: NODES LOCAL REFERENCE SYSTEM RE-ORIENTED: FRONT LOWER BUMPER.

- Front lower bumper EMA’s results:

Mode -Front lower bumper	Frequency [Hz]	Mode Shape
Mode 1	289.7	1st Bending
Mode 2	545.3	2nd Bending
Mode 3	588.6	3rd Bending
Mode 4	687.4	4th Bending
Mode 5	1014	5th Bending
Mode 6	1566	6th Bending

TABLE 5.10: FRONT LOWER BUMPER EMA’S RESULTS.

Chapter 6

6 Components model updating and MacDistW.m

In this chapter, it will be shown the model updating of each numerical model deeply described into chapter 4, through the results obtained into the chapter **5**, and even the output of the MatLab function "MacDistW.m", which defines the correspondence between the numerical and experimental modal parameters.

What the model updating is and how the "MacDistW.m" function determines that correlation, has been already defined in the thesis section **1.2** of the chapter **1.**

So, per each of the main and secondary components, the comparison of natural frequencies between the EMA and FEA updated results will be reported in a table. It will follow the list of the updated material properties.ì and the output of the MatLab function "MacDistW.m".

- Chassis:

Chassis	Frequency [Hz]		
Mode	EMA	FEA updated	Error [%]
Mode 1	42.6	42.6	0.00
Mode 2	43.5	45.92	5.27
Mode 3	64.85	64.07	1.20
Mode 4	83.93	83.97	0.05
Mode 5	88.49	88.43	0.07
Mode 6	102.4	104.5	2.01

TABLE 6.1: COMPARISON CHASSIS' NATURAL FREQUENCIES BETWEEN EMA AND FEA UPDATED RESULTS.

For getting this value, as material property only the Young's modulus has been changed and it has been calibrated the stiffness k (imposed equal to $k = 67000\ \frac{N}{m}$) of the elastic elements introduced between the tubular frame and the supports component of seat and steering system, with the aim of simulating as better as possible the welding.

Updated material properties (only E changed):

- `rho_4130 = 7850;   %material density`
- `E_4130 = 210.1e9;  %material Young’s modulus [Pa] UPDATED`
- `v_4130 = 0.30;     %material Poisson ratio`

To have a quantitative comparison between the eigenvectors numerically and experimentally obtained, the Modal Assurance Criterion has been evaluated. As previously introduced into the section **1.2**, MAC calculation is a used in Modal Analysis to indicate the similarity of two mode shapes. This tool compares two series of n eigenvectors and returns a $n\ x\ n$ matrix contained values from 0 to 100, as percentage of the correlation between the eigenvectors. The calculation is performed in Matlab through the function “MacDistW.m”, as a tool of LUPOS.

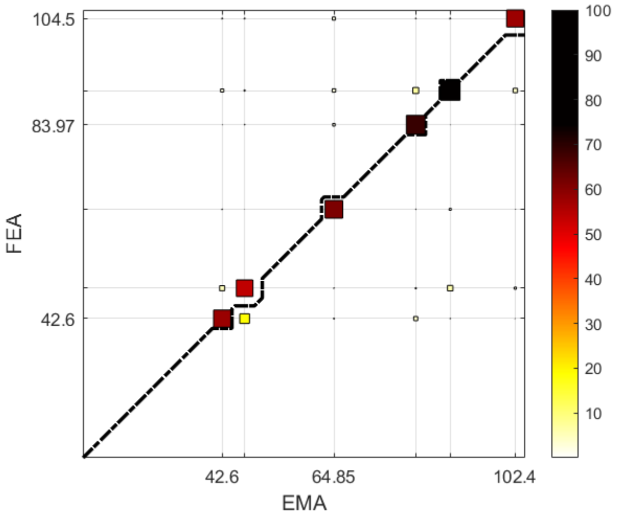

FIGURE 6.1: MACDISTW.M OUTPUT OF CHASSIS.

Figure **6.1** shows a representation of the MAC evaluated for the numerical and experimental models of the chassis. When the coloured square appears on the diagonal, it means that each numerical mode shape corresponds to the experimental one. The black line is the iso-frequency line. For what regards the colour, it could be said that:

- if the mode shapes are identical, which means that all points move the same, the MAC will have a value of one or 100%. So, the square is coloured in black.
- If the mode shapes are very different, the MAC value will be close to zero. The correspondent square’s colours are white/yellow.

Then, as shown from the colour bar of figure **6.1**, all the other colours (orange, red, dark grey) tells about an intermediate MAC value from 0 to 100.

- Front ARB:

Front ARB	Frequency [Hz]		
Mode	EMA	FEA updated	Error [%]
Mode 1	1260	1260	0.00
Mode 2	2084	2149	3.02
Mode 3	3365	3381	0.47

Table 6.2: Comparison Front ARB’s natural frequencies between EMA and FEA updated results.

Changed material properties: only Young’s modulus (E).
Updated material properties:

- `rho_ARB = 7850;   %material density  [kg/m3]`
- `E_ARB = 209.5e9;  %Young's modulus   [Pa] UPDATED`
- `v_ARB = 0.30;     %Poisson’s ratio`

MacDistW.m output:

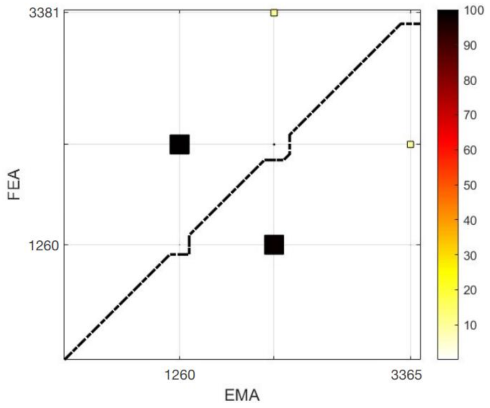

Figure 6.2: MacDistW.m output of Front ARB.

Since in the illustration **6.2** the squares are not on the diagonal, it means that the 1st numerical result (FEA) corresponds to the 2nd experimental result (EMA) and the 2nd numerical mode shape corresponds to the 1st experimental mode shape, both with 100% of correlation.

- Standard seat:

Standard seat	Frequency [Hz]		
Mode	EMA	FEA Updated	Error [%]
Mode 1	30.69	30.68	0.03
Mode 2	99.7	60.49	39.32
Mode 3	137.3	108.9	20.68
Mode 4	150.7	139.9	0.07
Mode 5	193	170.8	0.12

TABLE 6.3: COMPARISON STANDARD SEAT'S NATURAL FREQUENCIES BETWEEN EMA AND FEA UPDATED RESULTS.

Changed material properties: Young's modulus (E) and material density (ρ), for making equal the numerical weight with the real one.

Updated material properties:

- `rho_ARB = 2131.8;   %material density  [kg/m3] UPDATED`
- `E_ARB = 53.85e9;    %Young's modulus   [Pa] UPDATED`
- `v_ARB = 0.20;       %Poisson's ratio`

MacDistW.m output:

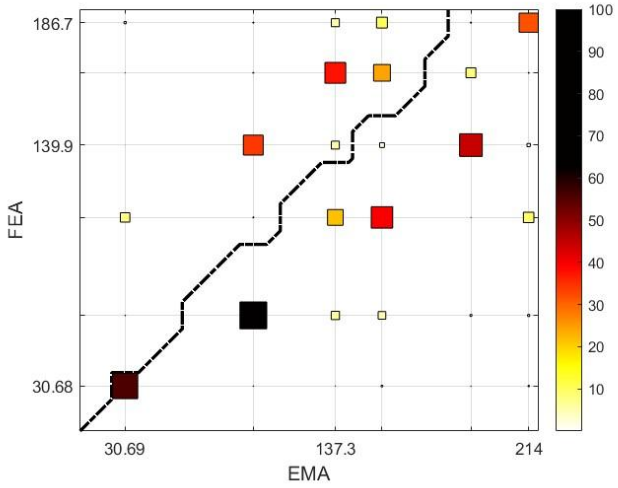

FIGURE 6.3: MACDISTW.M OUTPUT OF STANDARD SEAT.

In this case, from the third mode the correlation index lowers its value with even a mode shapes conformity that does not appear on the diagonal. This result was expected because, the 3D CAD model used for producing the numerical model simulated with LUPOS, is a bit different in terms of shape with the real seat and so, the modal shift of each node does not find the right correlation.

- Greyhound seat:

Greyhound Seat	Frequency [Hz]		
Modes	EMA	FEA Updated	Error [%]
Mode 1	19.73	19.73	0.00
Mode 2	57.87	38.90	32.78
Mode 3	86.52	70.06	19.02
Mode 4	94.09	89.95	4.40
Mode 5	112.4	109.90	2.22

TABLE 6.4: COMPARISON GREYHOUND SEAT'S NATURAL FREQUENCIES BETWEEN EMA AND FEA UPDATED RESULTS.

Even for the Greyhound seat, it has been changed the Young’s modulus (**E**) and the material density (**ρ**), for making equal the numerical weight with the real one.
Updated material properties:

```
▪   rho_ARB = 1928.9;   %material density  [kg/m3] UPDATED
▪   E_ARB = 20.14e9;    %Young's modulus   [Pa] UPDATED
▪   v_ARB = 0.20;      %Poisson’s ratio
```

MacDistW.m output:

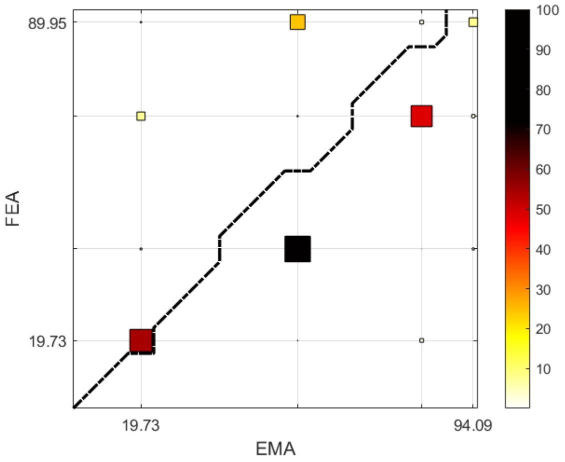

FIGURE 6.4: MACDISTW.M OUTPUT OF GREYHOUND SEAT.

- Rear axle:

Rear axle	Frequency [Hz]		
Mode	EMA	FEA -Updated	Error [%]
Mode 1	285.7	285.9	0.07
Mode 2	286.2	285.9	0.11
Mode 3	760.7	769.5	1.14
Mode 4	768.1	769.5	0.18
Mode 5	1439	1460	1.44
Mode 6	1452	1460	0.55

TABLE 6.5: COMPARISON REAR AXLE’S NATURAL FREQUENCIES BETWEEN EMA AND FEA UPDATED RESULTS.

Changed material properties: only Young’s modulus (E).
Updated material properties:

```
▪   rho_ARB = 7870;   %material density  [kg/m3]
▪   E_ARB = 203.2e9;  %Young's modulus   [Pa] UPDATED
▪   v_ARB = 0.29;     %Poisson’s ratio
```

MacDistW.m output:

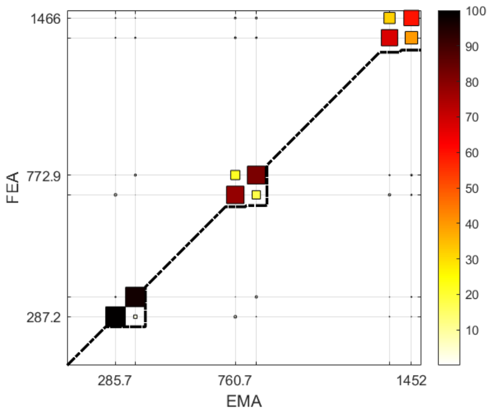

FIGURE 6.5: MACDISTW.M OUTPUT REAR AXLE.

- Floor panel:

Floor panel	Frequency [Hz]		
Modes	EMA	FEA Updated	Error [%]
Mode 1	15.51	15.51	0.00
Mode 2	16.8	16.78	0.12
Mode 3	44.44	41.24	7.20
Mode 4	48.81	52.67	7.33
Mode 5	73.96	78.73	6.04
Mode 6	90.2	92.6	2.59

TABLE 6.6: COMPARISON FLOOR PANEL'S NATURAL FREQUENCIES BETWEEN EMA AND FEA UPDATED RESULTS.

Changed material properties: only Young's modulus (E).
Updated material properties:

- `rho_ARB = 2689;    %material density  [kg/m3]`
- `E_ARB = 31.2e9;    %Young's modulus   [Pa] UPDATED`
- `v_ARB = 0.34;      %Poisson’s ratio`

MacDistW.m output:

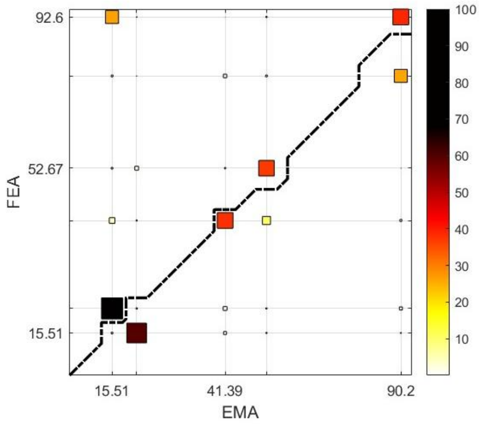

FIGURE 6.6: MACDISTW.M OUTPUT OF FLOOR PANEL.

- Steering column:

Steering column	Frequency [Hz]		
Mode	EMA	FEA Updated	Error [%]
Mode 1	376.9	376.9	0.00
Mode 2	394.7	384.4	2.61
Mode 3	1082	1018	5.92
Mode 4	1096	1053	3.92
Mode 5	1994	1793	10.08

TABLE 6.7: COMPARISON STEERING COLUMN'S NATURAL FREQUENCIES BETWEEN EMA AND FEA UPDATED RESULTS.

Changed material properties: only Young's modulus (E).
Updated material properties:

- `rho_ARB = 7850;      %material density  [kg/m3]`
- `E_ARB = 139.25e9;    %Young's modulus   [Pa] UPDATED`
- `v_ARB = 0.29;        %Poisson’s ratio`

MacDistW.m output:

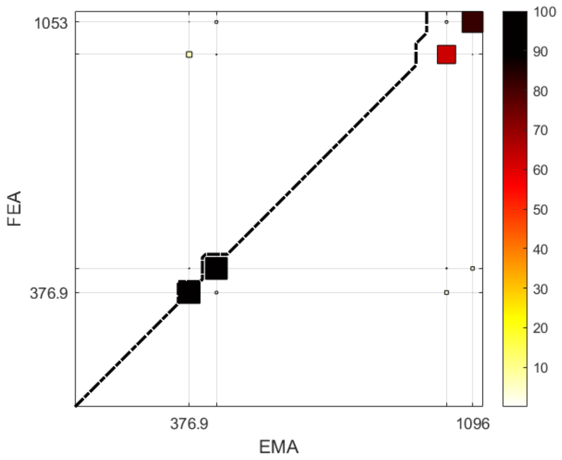

FIGURE 6. 7: MACDISTW.M OUTPUT OF STEERING COLUMN.

- Steering tie-rod:

Steering Tie-Rod	Frequency [Hz]		
Mode	EMA	FEA Updated	Error [%]
Mode 1	652.9	652.9	0.00
Mode 2	752.7	652.9	13.26
Mode 3	1949	1847	5.23
Mode 4	2290	1847	19.34
Mode 5	3250	3678	11.63
Mode 6	3909	3878	0.79

TABLE 6.8: COMPARISON STEERING TIE-ROD'S NATURAL FREQUENCIES BETWEEN EMA AND FEA UPDATED RESULTS.

Changed material properties: only Young's modulus (E).
Updated material properties:

```
rho_ARB = 2689.8;     %material density  [kg/m3]
E_ARB = 72.41e9;      %Young's modulus   [Pa] UPDATED
v_ARB = 0.34;         %Poisson's ratio
```

MacDistW.m output:

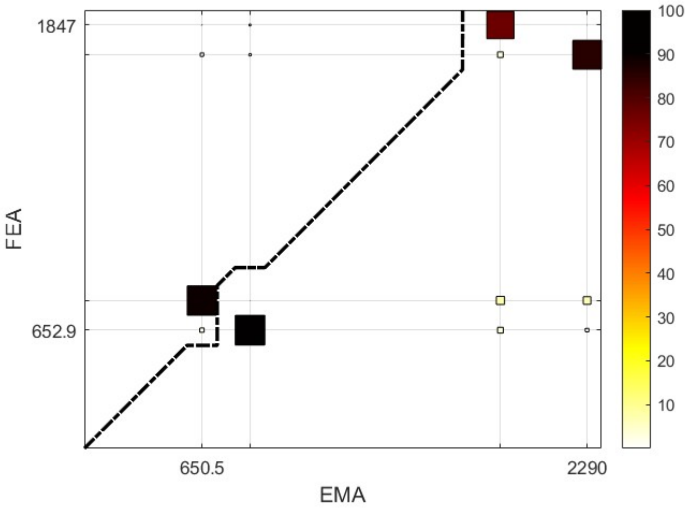

FIGURE 6.8: MACDISTW.M OUTPUT OF STEERING TIE-ROD.

- Stub-axle:

Stub-axle	Frequency [Hz]		
Mode	EMA	FEA Updated	Error [%]
Mode 1	724.6	724.6	0.00
Mode 2	1109	1072	3.34
Mode 3	1482	1382	6.75
Mode 4	2529	2576	1.82
Mode 5	2726	2958	7.84

TABLE 6.9: COMPARISON STUB-AXLE'S NATURAL FREQUENCIES BETWEEN EMA AND FEA UPDATED RESULTS.

Changed material properties: only Young's modulus (E).
Updated material properties:

```
rho_ARB = 7850;       %material density  [kg/m3]
E_ARB = 179.55e9;     %Young's modulus   [Pa] UPDATED
v_ARB = 0.3;          %Poisson's ratio
```

MacDistW.m output:

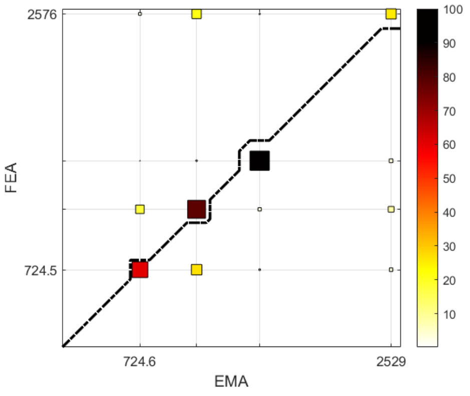

FIGURE 6.9: MACDISTW.M OUTPUT OF STUB-AXLE.

- Front lower bumper:

Front lower bumper	Frequency [Hz]		
Mode	EMA	FEA Updated	Error [%]
Mode 1	289.7	289.7	0.00
Mode 2	545.3	539.3	1.10
Mode 3	588.6	627.9	6.26
Mode 4	687.4	703.8	2.33
Mode 5	1014	1159	12.51
Mode 6	1566	1672	6.34

TABLE 6.10: COMPARISON STUB-AXLE'S NATURAL FREQUENCIES BETWEEN EMA AND FEA UPDATED RESULTS.

Changed material properties: Only Young's modulus (E).
Updated material properties:

- `rho_ARB = 7850;       %material density  [kg/m3]`
- `E_ARB = 185.4e9;      %Young's modulus   [Pa] UPDATED`
- `v_ARB = 0.29;         %Poisson’s ratio`

MacDistW.m output:

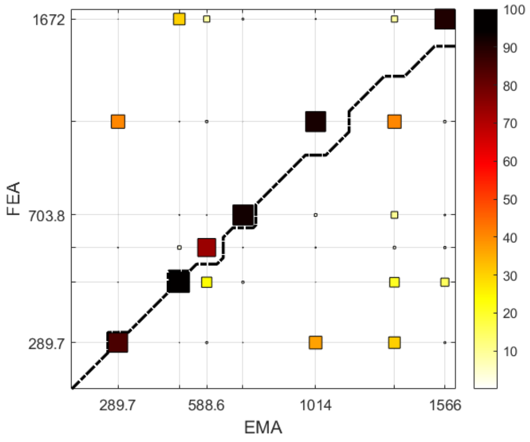

FIGURE 6.10: MACDISTW.M OUTPUT OF FRONT LOWER BUMPER.

Chapter 7

7 Final Assembly

Up to now, it has been done the evaluation of the numerical and experimental modal behaviour of each component of the complete kart vehicle. The aim of this chapter is to study the final assembly of a go-kart.

For first, each part has been "numerically assembled" in order of getting the numerical model of the complete vehicle (chapter **7.1**) and then simulated, for understanding which kind of natural frequencies and mode shapes have to be expected. Secondly, the previously analysed components have been connected through specifics bolts and screws into the laboratory, obtaining a go-kart vehicle almost ready to be used on track. Then, the experimental modal analysis has been carried out on the final assembly (chapter **7.2**). Finally, a comparison between the numerical and experimental modal analysis will be shown (chapter **7.3**).

FIGURE 7.1: GO-KART VEHICLE ASSEMBLED INTO THE LABORATORY.

7.1 FEA

The generation of the numerical model has been started with the numerical model of the naked chassis reported into the chapter **4.2.1**. Afterwards, for introducing the other main and secondary components, it could not be leveraged the nodes coordinates saved into the chapter **4**, for the singular numerical model. For this reason, the vehicle has been firstly assembled into the laboratory (figure **7.1**). Once finished this assembling process, new nodes coordinates of each component have been taken from the vehicle, saved and introduced, step by step, into the numerical model of the naked chassis for obtaining the numerical final assembly. As it is possible to see from the illustration **7.1,** there are some plastic components (called “Bodywork”) which have not been analysed neither numerically nor experimentally.

Figure 7.2: OTK bodywork.

This because it is not worth to make a modal analysis on components like the bodyworks, since they are made as said, in plastic. But, in terms of introducing such parts into the numerical model for sake of completeness, they have been found on “GrabCAD” website and the SolidWorks part have been downloaded. Only the side bumpers have been considered as lumped masses.

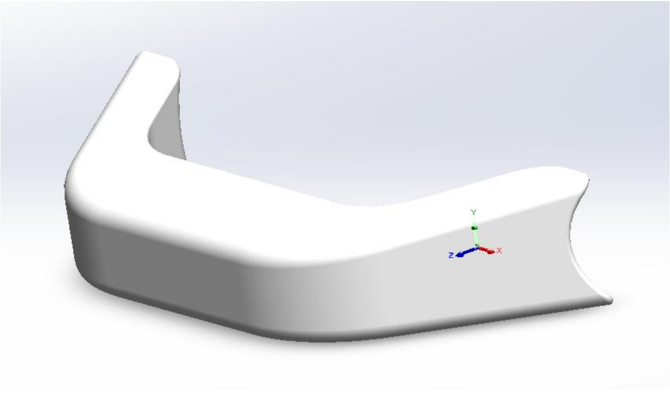

Figure 7.3: Front fairing from grabCAD.

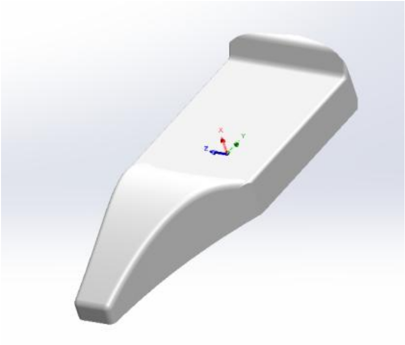

FIGURE 7.4: FRONT SPOILER FROM GRABCAD.

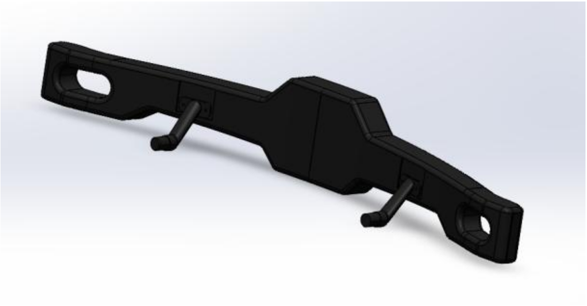

FIGURE 7.5: REAR BUMPER FROM GRABCAD.

These SolidWorks parts have been treated as other two thin-walled components: seat and floor panel. Indeed, being the bodywork's parts shell elements of thickness equal to 3mm, the only way to introduce them into the LUPOS numerical model is using the "Hexa" elements. For this reason, the same item deeply explained more times into the previous chapters (as in the **4.2.3** about the Seat numerical model) has been followed: loading of the SolidWorks part into Hypermesh, 3D mesh generation (element size of 10mm has been chosen since it is was demonstrated to be the best discretization), export of the meshed file, file extension modification (.fem to .bdf), FEM tool "BDFtoLUPOS.p" employment and, finally, loading of the nodes coordinates and of the hexahedral elements into the Matlab script requested by LUPOS for simulating the numerical model.

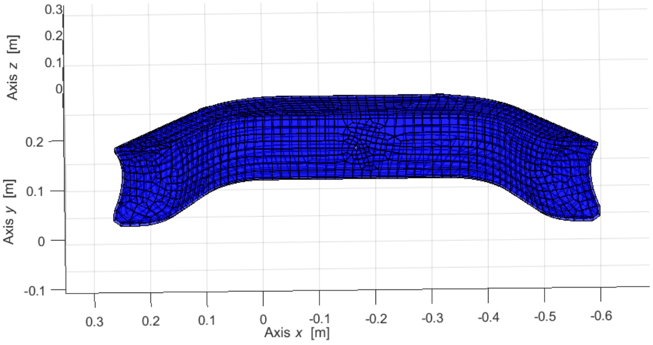

FIGURE 7.6: LUPOS NUMERICAL MODEL OF FRONT FAIRING.

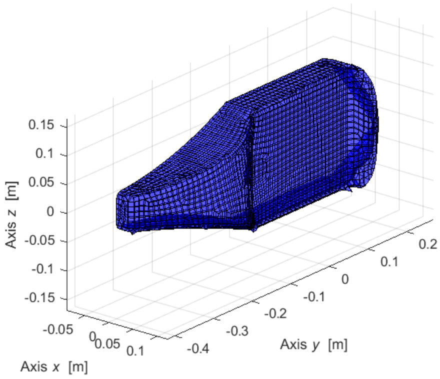

FIGURE 7.7: LUPOS NUMERICAL MODEL OF FRONT SPOILER.

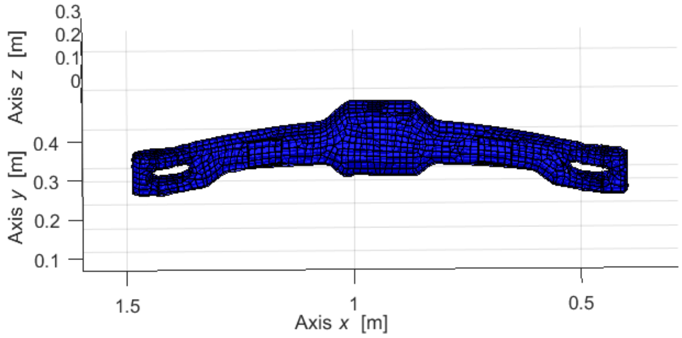

FIGURE 7.8: LUPOS NUMERICAL MODEL OF REAR BUMPER.

At the end of the numerical assembling process, where each component has been introduced with its own updated material properties into the chapter **6**, the final numerical go-kart vehicle that has been obtained is shown below:

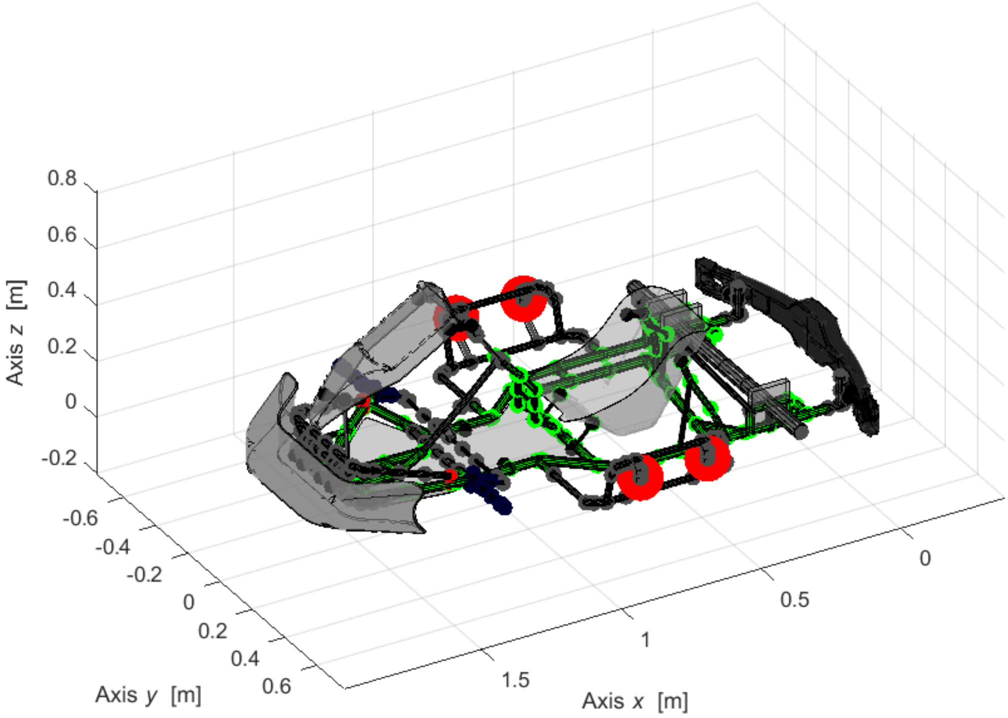

FIGURE 7.9: LUPOS NUMERICAL MODEL OF FINAL ASSEMBLY.

Hence, LUPOS numerical simulation results are:

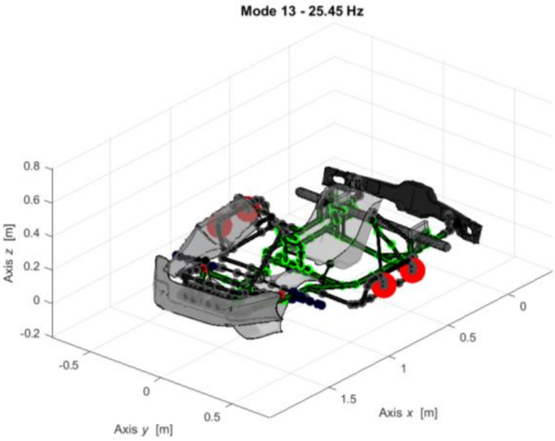

FIGURE 7.10: 1ST BENDING

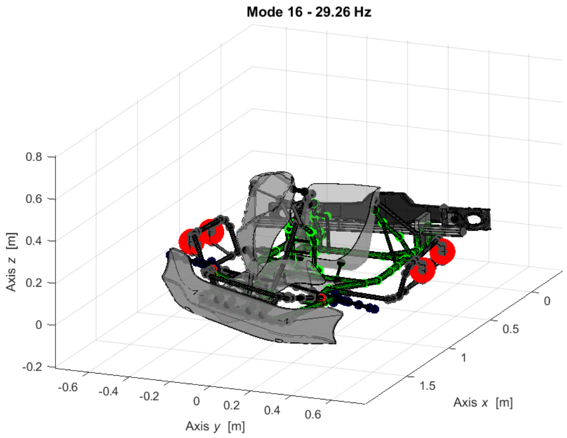

FIGURE 7.11: 1ST TORSION

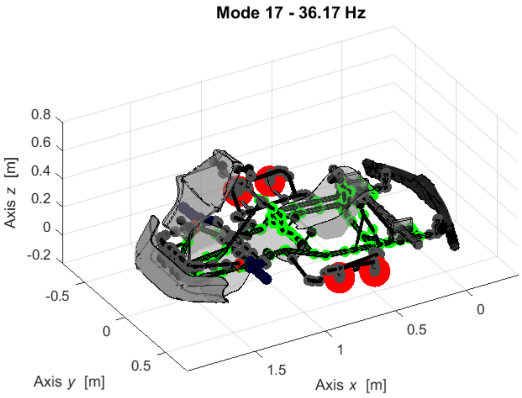

FIGURE 7.12: 2ND BENDING

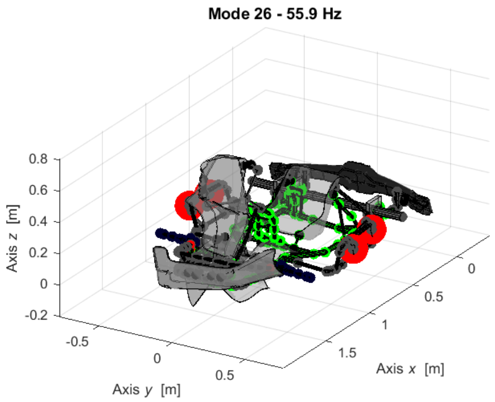

FIGURE 7.13: 2ND TORSION

Modes - Assembly	Frequency [Hz]	Mode Shape
Mode 1	25.45	1st Bending
Mode 2	29.26	1st Torsion
Mode 3	36.17	2nd Bending
Mode 4	55.90	2nd Torsion

TABLE 7.1: LUPOS NUMERICAL MODAL ANALYSIS RESULTS, ASSEMBLY.

7.2 EMA

With the aim of performing the experimental modal analysis on the final assembly, it has been necessary to produce new nodes split on each component of the vehicle, for avoiding to have too much nodes to be hammered during the experimental test.

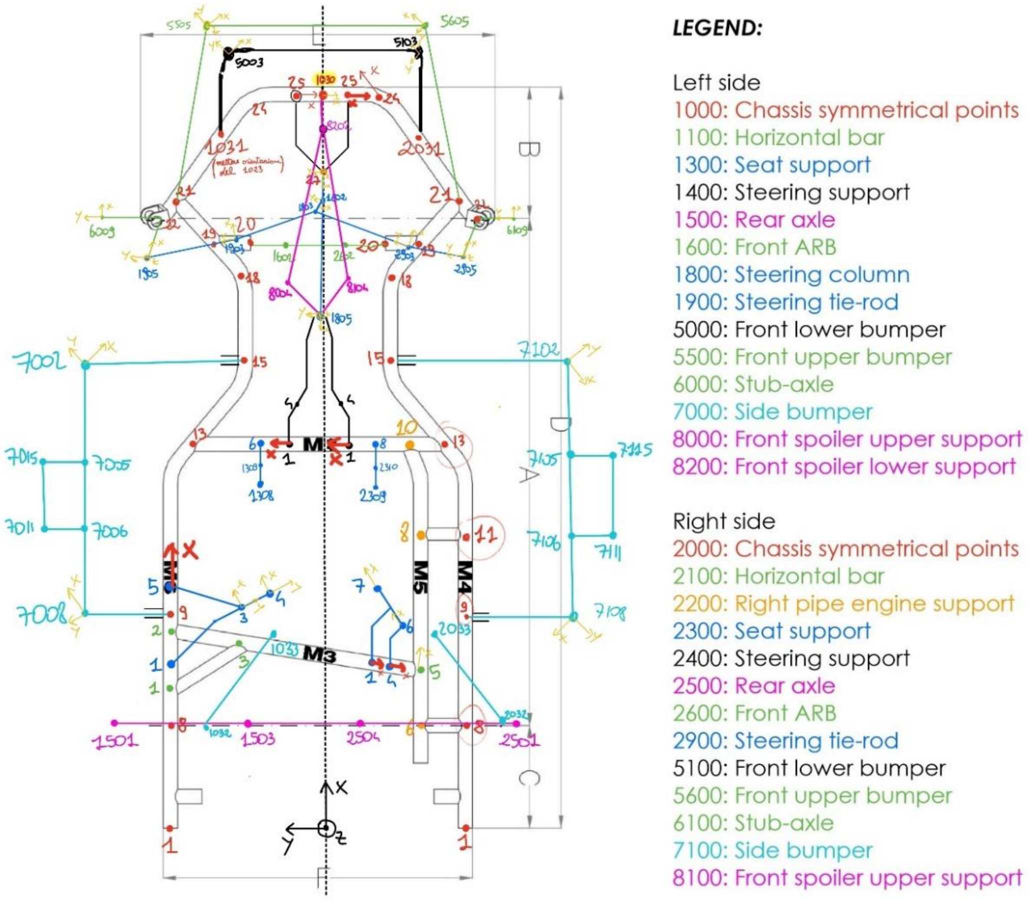

FIGURE 7.14: FINAL ASSEMBLY NODES DIVISION.

Then, it has been followed the same steps defined into chapter 5:

- MoGeSeC output. Only the tubular frame nodes have been considered when given the input files to MoGeSeC, in order of locating the accelerometers just on the chassis frame.

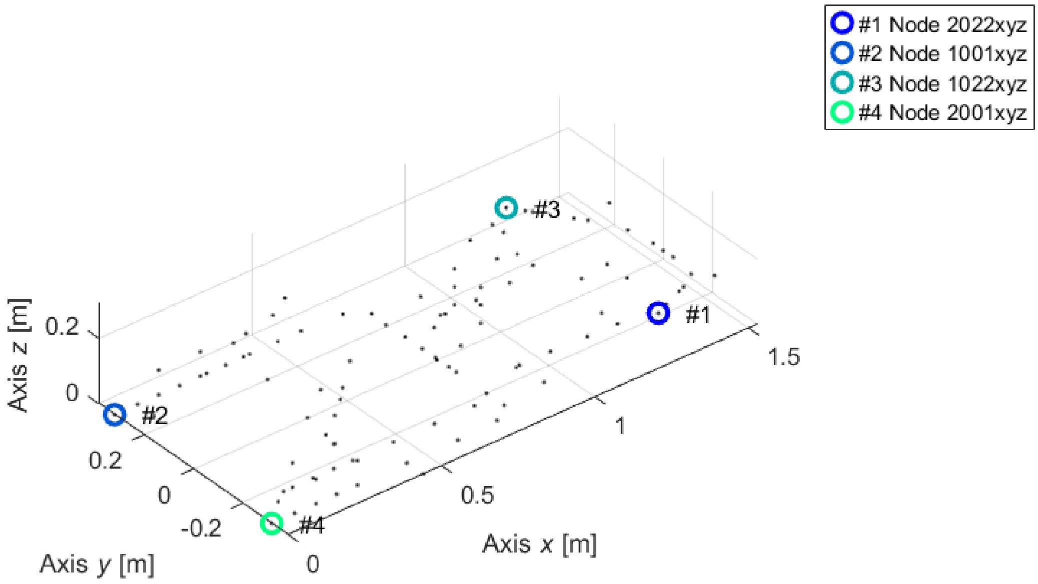

FIGURE 7.15: FINAL ASSEMBLY MOGESEC'S OUTPUT.

The transducers have been positioned in the following nodes:

1. 2021 (not 2022 since it is a point where there is a bolt connection between the fixation sustaining the stub axle and the stub-axle itself);
2. 1001;
3. 1021 (not 1022 for the same reason explained at point 1);
4. 2001.

- Hanged Final assembly with accelerometers:

FIGURE 7.16: HANGED FINAL ASSEMBLY WITH ACCELEROMETERS INSTALLED ON NODES 2021, 1001, 1021, 2001.

- Test.Lab model nodes local reference system re-oriented: Final assembly.

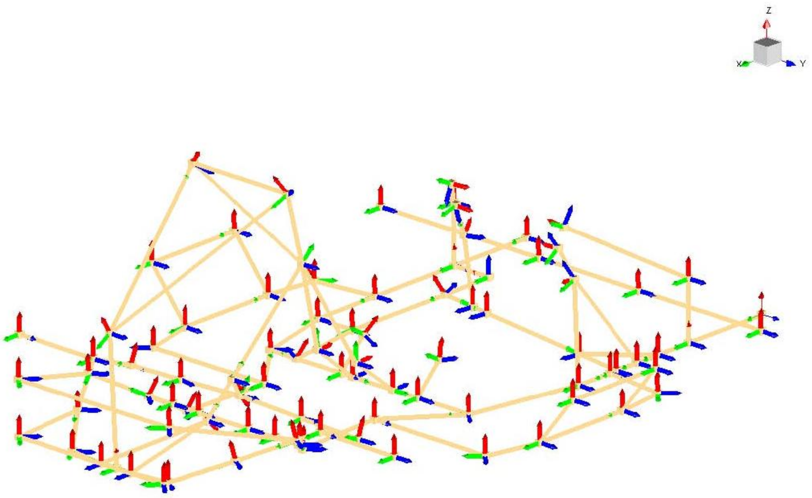

FIGURE 7.17: NODES LOCAL REFERENCE SYSTEM RE-ORIENTED: FINAL ASSEMBLY.

- Final Assembly EMA's results:

Mode - Assembly	Frequency [Hz]	Mode Shape
Mode 1	18.97	1st Torsion
Mode 2	19.99	1st Bending
Mode 3	26.89	2nd Bending
Mode 4	59.62	2nd Torsion

TABLE 7.2: FINAL ASSEMBLY EMA'S RESULTS.

7.3 FEA vs EMA and MacDistW.m

- FEA vs EMA:

Assembly	Frequency [Hz]		
Mode	EMA	FEA	Error [%]
Mode 1	18.97	25.45	25.46
Mode 2	19.99	29.26	31.68
Mode 3	26.89	36.17	25.65
Mode 4	59.62	55.90	6.24

TABLE 7.3: FINAL ASSEMBLY FEA AND EMA COMPARISON.

- MacDistW.m output:

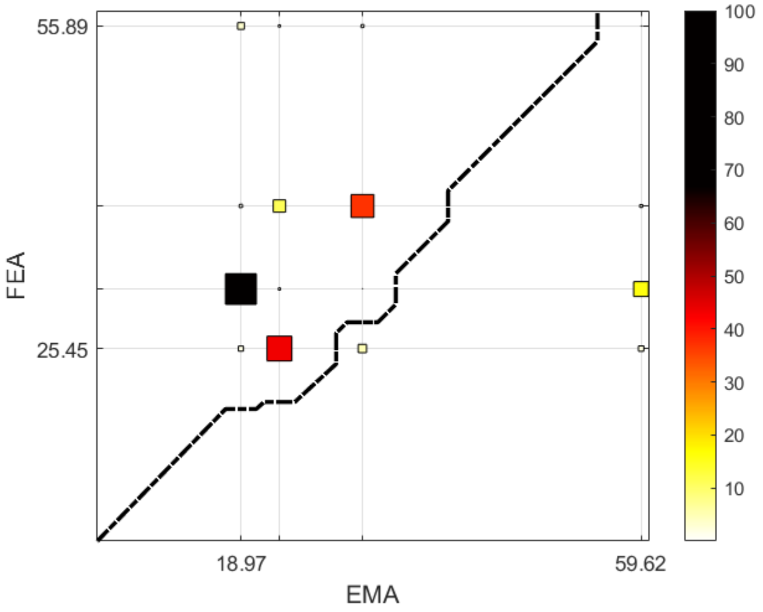

FIGURE 7.18: MACDISTW.M OUTPUT OF FINAL ASSEMBLY.

It can be concluded saying that, even if there is an error of 25%-30% between the numerical and experimental results, it can be considered acceptable due to some software's limitations had during the development of the numerical model which forced us in introducing some simplifications. Indeed, the screws and bolts connections present into the real vehicle, could not be modelled in LUPOS. So, rigid connections are present into the numerical vehicle assembly, which leads to get a numerical system is much more rigid than the real one: this can widely explain why the frequencies regarding the first three mode shapes are higher in the numerical simulation.

Chapter 8

8 Conclusions

The aim of the thesis project was to prepare the basis for all the future developments studies about the go-kart vehicle performance. All the introductory parts where it has been explained how these vehicles work, would like to enthuse the reader about how wide this awesome world is and why a kind of improvement process could make the difference in terms of dynamic performance. Moreover, the model validation of each component of the complete vehicle, has given to us the possibility of understanding how it behaves and to spot the right material property. Indeed, as seen into the chapter **4**, the material used for the analysed test object was supposed to be something close to the real one. Then, after the Experimental modal analysis, the model updating process has paved the way for calibrating the properties of each component. Thanks to this, it has been found that different levels of stiffnesses are present in the whole kart vehicle if all the parts are taken into account, demonstrating the variety of materials and of the studying that is present on these vehicles for improving the performances.

The future work must regard the real karting manoeuvres simulation of the vehicle validated into this thesis, integrating the obtained results into a multy-body system. Indeed, the multi-body numerical analysis of a go-kart is focused on the evaluation of the vehicle dynamics performance sensibility with respect to the stiffness of its main structural components. For this reason, the structural behaviour of these elements has been in deep analysed in this work.

Bibliography

[1–19]

[1] K. Horváth, A. Zelei, Development of a multibody model for go-karts considering frame flexibility, Pollack Periodica (2024).

[2] M. Muzzupappa, G. Matrangolo, G. Vena, Methods for the Evaluation of the Go-Kart Vehicle Dynamic Performance by the Integration of CAD/CAE Techniques, in: XVIII International Congress on Graphic Engineering. INGEGRAF, 2006.

[3] T.O. Sadiq, L. Mohd Daud, J. Idris, Investigation of microstructure and mechanical properties of A335 P11 main steam pipe in Stesen Janaelektrik Jambatan Connaught Power Plant, Malaysia, Transactions of the Indian Institute of Metals 71 (2018) 2527–2540.

[4] A. Schweighardt, B. Vehovszky, D. Feszty, Modal Analysis of the Tubular Space Frame of a Formula Student Race Car, Manufacturing Technology, Engineering Science and Research Journal 20 (2020).

[5] K. Horváth, A. Zelei, Development of a multibody model for go-karts considering frame flexibility, Pollack Periodica (2024).

[6] P. Luque, D.A. Mántaras, A. Pello, Racing car chassis optimization using the finite element method, multi-body dynamic simulation and data acquisition, Proc Inst Mech Eng P J Sport Eng Technol 227 (2013) 3–11.

[7] R. Koike, T. Shiiba, M.F. Bin Ashari, Vehicle simulations of a racing kart with flexible multibody dynamic analysis, in: Dynamic Systems and Control Conference, American Society of Mechanical Engineers, 2012: pp. 59–64.

[8] A. Padhi, A. Joshi, N. Hitesh, C. Rakesh, A. Padhi, A. Joshi, N. Hitesh, C. Rakesh, Increase factor of safety of go-kart chassis during front impact analysis, International Journal for Innovative Research in Science & Technology 3 (2016) 385–390.

[9] K. Nagendra, G.V.R. Reddy, P. Vijay, K.A. Yadav, G.N. Reddy, DESIGN AND ANALYSIS OF A GO-KART CHASSIS BYCOMPARING DIFFERENT MATERIALS, (2022).

[10] J. Mikler Anaya, Construction of a computational model of a go-kart for dynamic analysis: multibody model construction and theoretical analysis, (2018).

[11] G.A. Mesquita, E.D.M. Santanna, C.T.M. Anflor, COB-2023-1399 IMPROVING CHASSI KART STRUCTURE CONSIDERING FATIGUE, MODAL AND STATIC ANALYSES THROUGH FINITE ELEMENT ANALYSIS, (n.d.).

[12] V. Pattanshetti, Design and analysis of go kart chassis, International Journal of Mechanical and Industrial Technology 4 (2016) 150–164.

[13] R.S. Kiran, S.S. Chandu, Design and Analysis of Go-Kart Chassis using Distinctive Materials, International Journal for Research in Applied Science & Engineering Technology (IJRASET) 8 (n.d.).

[14] S. Krishnamoorthi, L. Prabhu, M.D. Shadan, H. Raj, N. Akram, Design and analysis of electric Go-Kart, Mater Today Proc 45 (2021) 5997–6005.

[15] G. Mirone, Multi-body elastic simulation of a go-kart: Correlation between frame stiffness and dynamic performance, International Journal of Automotive Technology 11 (2010) 461–469.

[16] R. Lot, N. Dal Bianco, Lap time optimisation of a racing go-kart, Vehicle System Dynamics 54 (2016) 210–230.

[17] N.A.Z. Abdullah, M.S.M. Sani, N.A. Husain, M.M. Rahman, I. Zaman, Dynamics properties of a Go-kart chassis structure and its prediction improvement using model updating approach, International Journal of Automotive and Mechanical Engineering 14 (2017) 3887–3897.

[18] D. Sampayo, P. Luque Rodríguez, D. Álvarez Mántaras, E. Rodríguez Ordóñez, Go-kart chassis design using finite element analysis and multibody dynamic simulation, International Journal of Simulation Modelling (2021).

[19] K. Hajare, Y. Shet, A. Khot, A review paper on design and analysis of a go-kart chassis, International Journal of Engineering Technology, Management and Applied Sciences 4 (2016) 212–214.